5-2018

Nonlinear Optical Phenomena in Emerging Low-dimensional Materials

Yongchang Dong
Clemson University, yongchang.dong@gmail.com

NONLINEAR OPTICAL PHENOMENA IN EMERGING LOW-DIMENSIONAL MATERIALS

A Dissertation
Presented to
the Graduate School of
Clemson University

In Partial Fulfillment
of the Requirements for the Degree
Doctor of Philosophy
Physics

---

by
Yongchang Dong
May 2018

Accepted by:
Apparao M. Rao, Committee Chair
Ramakrishna Podila, Co-Chair
Mark Leising
Ya-Ping Sun

ABSTRACT

As digital information technologies continue to evolve at much faster rates than the growth of Si-based processors, the encroachment of light-based technologies into computing seems inevitable. With the advent of lasers, photonic crystals, and optical diodes, photonic computing has made significant strides in information technology over the past 30 years. This continuing integration of light into all-optical computing, optoelectronic components, and emerging optogenetic technologies demands the ability to control and manipulate light in a predictable fashion, or by design. Of particular interest, is the passive control and manipulation of light in all-optical switches, photonic diodes, and optical limiting which can be achieved by leveraging intrinsic non-linear optical properties of low dimensional materials.

The reverse saturable absorption in fullerenes has been widely used to realize excellent passive optical limiters for the visible region up to 650 nm. However, there is still a need for passive optical switches and limiters with a low limiting threshold (<0.5 J/cm^2) and higher damage limits. The electronic structure of fullerenes can be modified either through doping or by the encapsulation of endohedral clusters to achieve exotic quantum states of matter such as superconductivity. Building on this ability, we discuss in Chapter 2 that the encapsulation of Sc_3N, Lu_3N or Y_3N in C_{80} alters the HOMO-LUMO gap and leads to passive optical switches with a significantly low limiting threshold (0.3 J/cm^2) and a wider operation window (average pulse energy >0.3 mJ in the ns regime).

In addition to extraordinary and strongly anisotropic electronic properties, two dimensional (2D) materials such as graphene and boron nitride, exhibit strong light-matter

interactions despite their atomic thickness. The nonlinear light-matter interactions in 2D materials are well suited for several applications in photonics and optoelectronics, such as ultrafast optical switching and optical diodes. Unlike most 2D materials that display nonlinear saturable absorption or increased light transmission at higher fluences, hexagonal boron nitride nanoplatelets (BNNPs) exhibit enhanced opaqueness with increasing light fluence. A two-photon absorption (2PA) process was previously proposed to explain the intrinsic non-linear absorption in BNNPs at 1064 nm or 1.16 eV (Kumbhakar *et al.*, Advanced Optical Materials, vol. 3, pp. 828, 2015); which is counter-intuitive because a 2PA process at 1.16 eV cannot excite electrons across the wide band gap of BNNPs (~5.75 eV). Here, through a systematic study of the non-linear properties of BNNPs we uncover a notoriously rare non-linear phenomenon, *viz.*, five-photon absorption (5PA) at 1064 nm for low laser input fluences (below 0.6 J/cm^2) that irreversibly transforms to a 2PA for higher laser input fluences (above 0.6 J/cm^2). Our detailed experimental and theoretical findings delineated in Chapter 3 provide compelling evidence that the high laser fluence generates defects in BNNPs (*e.g.*, oxygen/carbon doping), which support a 2PA process by inducing new electronic states within the wide band gap of BNNPs.

MXenes comprise a new class of two-dimensional (2D) transition metal carbides, nitrides, and carbonitrides that exhibit unique light-matter interactions. Recently, 2D Ti_3CNT_x (T_x represents functional groups such as –OH and –F) was found to exhibit nonlinear saturable absorption (SA) or increased transmittance at higher light fluences that is useful for mode locking in fiber-based femtosecond lasers. However, the fundamental origin and thickness-dependence of SA behavior in MXenes remains to be understood. We

fabricated 2D $Ti_3C_2T_x$ thin films of different thicknesses using an interfacial film formation technique to systematically study their nonlinear optical properties. Using the open aperture Z-scan method, we find that the SA behavior in $Ti_3C_2T_x$ MXene arises from plasmon-induced increase in the ground state absorption at photon energies above the threshold for free carrier oscillations. The saturation fluence and modulation depth of $Ti_3C_2T_x$ MXene was observed to be dependent on the film thickness. Unlike other 2D materials, $Ti_3C_2T_x$ was found to show higher threshold for light-induced damage with up to 50% increase in nonlinear transmittance. Lastly, building on the SA behavior of $Ti_3C_2T_x$ MXenes, we demonstrate in Chapter 4 a $Ti_3C_2T_x$ MXene-based photonic diode that breaks time-reversal symmetry to achieve non-reciprocal transmission of nanosecond laser pulses. Finally, in Chapter 5, we discuss the equilibrium and non-equilibrium free carrier dynamics in a 16 nm thick $Ti_3C_2T_x$ film. High (~2 x 10^{21} cm^{-3}) intrinsic charge carrier density and relatively high (~34 cm^2/Vs) mobility of carriers within individual nanoplates (that comprise the $Ti_3C_2T_x$ film) result in an exceptionally large (~ 46 000 cm^{-1}) absorption in the THz range, implying the potential use of $Ti_3C_2T_x$ for THz detection. We also demonstrate that $Ti_3C_2T_x$ conductivity and THz transmission can be manipulated by photoexcitation, as absorption of near-infrared 800 nm pulses is found to cause transient suppression of the conductivity that recovers over hundreds of picoseconds. The possibility of controlling THz transmission and conductivity via photoexcitation makes 2D MXenes suggests a promising material for application in THz modulation devices and variable electromagnetic shielding.

DEDICATION

*To those who shed **light** on my research and my life*

ACKNOWLEDGMENTS

My deepest gratitude and appreciation goes to my research advisers Dr. Apparao M. Rao and Dr. Ramakrishna Podila, for showing me the path in the scientific world. Their passion for science, work ethics, and immense knowledge will keep encouraging me to achieve higher goals in my career.

I also would like to thank my Ph.D. committee members – Dr. Mark Leising and Dr. Ya-Ping Sun, for their expertise and suggestions on my research projects.

My projects wouldn't have been possible without our prime collaborators Dr. Yury Gogotsi and Dr. Vadym N. Mochalin, who provided valuable samples and academic guidance. Many thanks to their team members Dr. Sergii Chertopalov, Dr. Babak Anasori and Kathleen Maleski for help on projects related to their samples.

My work was made enjoyable because of my beloved colleagues: Dr. Sriparna Bhattacharya, Herbert Behlow, Dr. Mehmet Karakaya, Dr. Jingyi Zhu, Dr. Deepika Saini, Sai Sunil Mallineni, Achyut Raghavendra, Wren Gregory, Anthony Childress, Fengjiao Liu, Longyu Hu, Jun Yi, Prakash Parajuli, Bipin Sharma, Shailendra Chiluwal and Lakshman Ventrapragada.

Special thanks to my parents Lizhong Dong and Hongqin Zhang for years of support. Thanks to Xi Yang for her kind support. Thanks to Dr. D. E. (Steve) Stevenson for inspiring weekly conversations. Thanks to Bill and Mary McGinn and their daughter Catherine who consider me as a part of their family, and *all* friends in Clemson.

TABLE OF CONTENTS

Page

Table of Contents (Continued)

Page

LIST OF TABLES

LIST OF FIGURES

List of Figures (Continued)

Figure Page

List of Figures (Continued)

Figure Page

List of Figures (Continued)

Figure Page

List of Figures (Continued)

Figure Page

CHAPTER ONE

INTRODUCTION TO NONLINEAR OPTICS

Light-matter interactions are ubiquitous in nature. Many commonly observed phenomena such as light scattering, reflection, refraction, and fluorescence result from light-matter interactions. From a classical standpoint, light-matter interactions can be viewed as a result of an oscillating electromagnetic field interacting with charged particles in matter. When an electromagnetic wave interacts with a material, the charges in medium are displaced from their equilibrium positions, so that positive nuclei move slightly (due to heavier mass) in the direction of the field, while the negatively charged electrons move in the opposite direction. Thus, dipole moments are created because of the displacement between positive and negative charges, and the dipole moment per unit volume describes the induced polarization (***P***) of the medium. At low light intensities, the dielectric polarization (***P***) of materials responds linearly to the electric field (***E***) of the light. However, at higher light intensities, the relationship between ***P*** and ***E*** becomes nonlinear. At high light intensities, when one or more electromagnetic waves propagate in a material, the atoms and molecules oscillate not only at the frequencies of the electric field applied, but also at different combinations of those frequencies as a result of the nonlinear response of the medium. Nonlinear optics (NLO) is the study of material phenomenon in which intense light induces a nonlinear response (e.g., nonlinear relationship between ***P*** and ***E***) in the medium, and in return, the medium modifies the optical fields in a nonlinear way. In fact, all media are

nonlinear to a certain degree. Several fundamental properties of materials such as non-linear absorption, refraction, second harmonic generation, as explained later in this chapter, can be probed using NLO spectroscopy [1], [2]. In general, nonlinear behavior of any media can be unveiled only with the help of highly intense light beams generated by lasers [1], [2]. The demonstration of second-harmonic generation by Franken *et al.* (1961) [3], shortly after the invention of laser is often considered as the birth of NLO spectroscopy.

In recent years, the discovery of low dimensional materials such as fullerenes (zero dimensional)[4], [5], carbon nanotubes (one dimensional)[6], [7], graphene (two dimensional)[8], [9] and other emerging nanostructures have been found to show interesting nonlinear optical phenomena[1], [10]. Knowledge of electronic transitions is critical in order to interpret the linear and nonlinear optical properties of nanomaterials. Very often, the energy levels in nanostructures are investigated by "linear" spectroscopic techniques such as optical absorption, photoluminescence, photoacoustic- and x-ray photoelectron spectroscopy[10]–[13]. However, nonlinear interaction of light plays important role in probing the higher electronic levels in low dimensional materials[12], [14]. Nanomaterials exhibit quantum confinement effects that alter their electronic energy levels, electronic density of states, phonon anharmonicity and bottlenecks[14]–[18], which lead to interesting changes in nonlinear properties with many promising applications such as ultrafast optical switching, optical limiting, passive mode locking, frequency up-conversion lasing, optical data storage, and multi-photon based laser microscopy. Interestingly, nanomaterials exhibit distinct intensity dependent nonlinear responses for laser excitation that depend on parameters such as the laser wavelength, pulse duration,

and repetition rate[19]–[21]. The physical basis of observed nonlinear optical responses in nanostructures is briefly elucidated in the following sections along with an outline for various experimental techniques used for probing their photophysical properties.

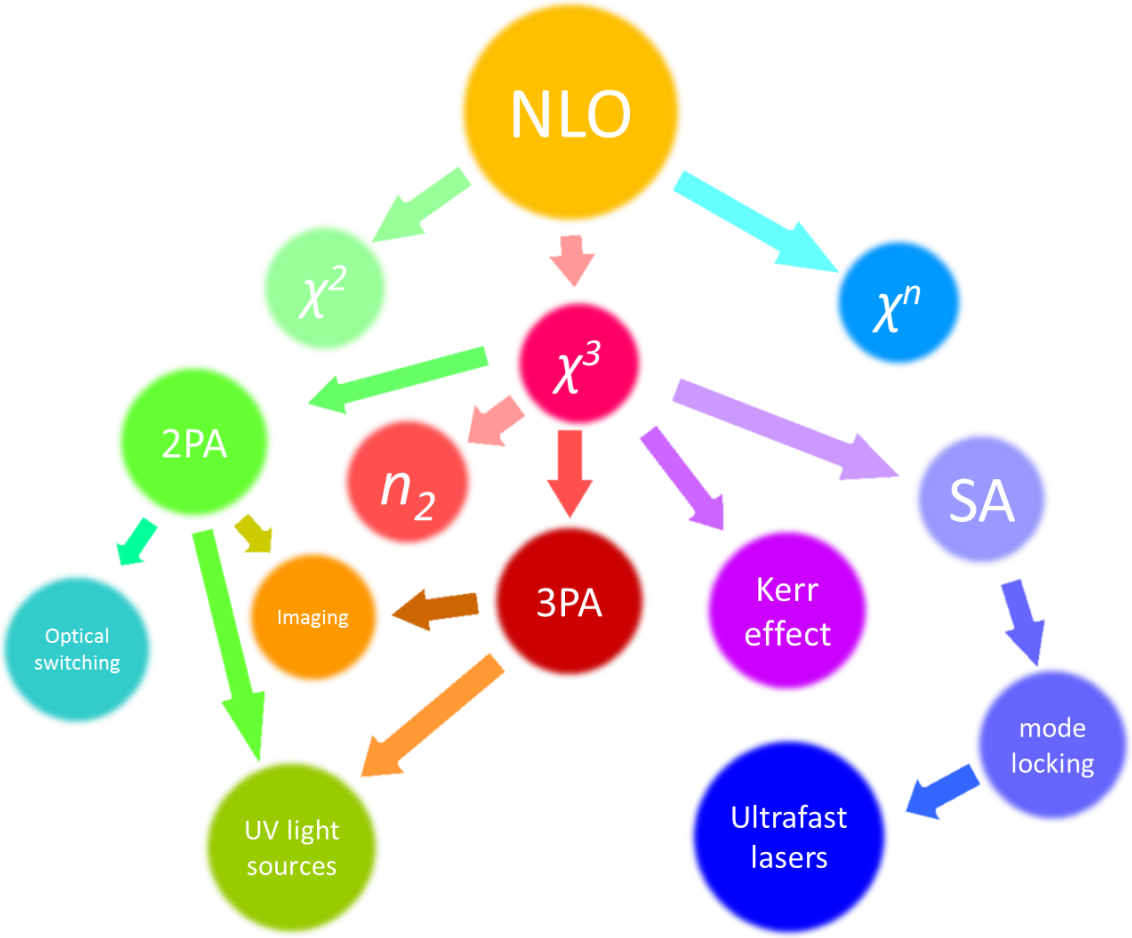

Figure 1.1. The illustration of various nonlinear optical (NLO) phenomenon and their applications. SA = saturable absorption, 2PA = two photon absorption, 3PA = three photon absorption. χ^2 and χ^3 are associated with light-induced nonlinear effects. n_2 is the nonlinear refractive index.

Table 1.1. Various nonlinear optical (NLO) phenomena and their applications.

NLO		
χ^2	χ^3	χ^n
Second harmonic generation (SHG)	Third harmonic generation (THG)	...
Optical refraction	Optical Kerr effect	
Parametric mixing	Non-degenerate four-wave mixing	
Pockel's effects	Stimulated Raman scattering (SRS)	
	Stimulated Brillouin Scattering (SBS)	
	Degenerate four-wave mixing	
	Two photon absorption (2PA)	
	DC induced harmonic generation	

1.1 Nonlinear Optical Processes

When the applied electric field is sufficiently small (e.g., < 10^8 V/m), the electric polarization, $\boldsymbol{P}$ is approximately linearly proportional with the applied electric field $\boldsymbol{E}$

$$\boldsymbol{P} = \chi \cdot \boldsymbol{E}, \tag{1.1}$$

where χ is the electric susceptibility tensor. This is the case of linear optics.

However, when the applied electric field is greater than 10^8 V/m, the induced polarization has a nonlinear dependence on the electric field and can be expressed as a power series with respect to the electric field as:

$$\boldsymbol{P} = \chi^1 \cdot \boldsymbol{E} + \chi^2 \cdot \boldsymbol{EE} + \chi^3 \cdot \boldsymbol{EEE} \tag{1.2}$$

$$\boldsymbol{P} = \boldsymbol{P^1} + \boldsymbol{P^2} + \boldsymbol{P^3}. \tag{1.3}$$

The first term χ^1 is responsible for linear absorption and refraction, while the remaining terms are associated with light-induced nonlinear effects.

In nonlinear optics, the product of two or more oscillating fields generates oscillations at different combinations of the incident frequencies. In order to account for this and to have a complete description of the process, the following notation is used:

$$\boldsymbol{P}(\boldsymbol{\omega}) = \chi^1(-\omega;\omega)\cdot\boldsymbol{E}(\omega) + \chi^2(-\omega_3;\omega_1\omega_2)\cdot\boldsymbol{E}(\omega_1)\boldsymbol{E}(\omega_2) + \chi^3(-\omega_4;\omega_1\omega_2\omega_3)\boldsymbol{E}(\omega_1)\boldsymbol{E}(\omega_2)\boldsymbol{E}(\omega_3)+.. \quad (1.4)$$

This notation also reflects the conservation of energy for each nonlinear process:

$$\omega_3 = \omega_1 + \omega_2 = \omega \text{ for } \chi^2, \quad (1.5)$$

$$\omega_4 = \omega_1 + \omega_2 + \omega_3 = \omega \text{ for } \chi^3. \quad (1.6)$$

In order to find the wave equation for a beam that propagates through a nonlinear optical medium, one starts with the Maxwell's equations (1.7-1.10):

$$\boldsymbol{\nabla}\cdot\boldsymbol{D} = \rho \quad (1.7)$$

$$\nabla\times\boldsymbol{E} = -\frac{\partial\boldsymbol{B}}{\partial t} \quad (1.8)$$

$$\boldsymbol{\nabla}\cdot\boldsymbol{B} = 0 \quad (1.9)$$

$$\nabla\times\boldsymbol{H} = \boldsymbol{J} + \frac{\partial\boldsymbol{D}}{\partial t}. \quad (1.10)$$

Assuming nonmagnetic materials with no free charges or currents, *i.e.* $\rho = 0$ and $\boldsymbol{J} = 0$, we get:

$$\boldsymbol{D} = \boldsymbol{P} + \varepsilon\boldsymbol{E}. \quad (1.11)$$

Using the above conditions and Maxwell's equations, we can determine the wave equation as:

$$\nabla \times \nabla \times \boldsymbol{E} = -\left(\frac{\partial}{\partial t}\right)\nabla \times \boldsymbol{B} = -\left(\frac{\partial}{\partial t}\right)\nabla \times \boldsymbol{H} = -(\partial/\partial t)\,[\boldsymbol{E} + (\partial/\partial t)\boldsymbol{E} + (\partial/\partial t)\boldsymbol{P^{NL}}]\,, \tag{1.12}$$

where $\boldsymbol{P^{NL}}$ is the nonlinear part of $\boldsymbol{P}$. Using the general vector notation $\nabla \times \nabla \times \boldsymbol{E} = \nabla(\nabla \cdot \boldsymbol{E}) - \nabla^2 \boldsymbol{E}$, we have for charge free medium:

$$\nabla^2 \boldsymbol{E} = \mu\sigma \left(\frac{\partial}{\partial t}\right)\boldsymbol{E} + \mu\varepsilon\left(\frac{\partial^2}{\partial t^2}\right)\boldsymbol{E} + \mu\left(\frac{\partial^2}{\partial t^2}\right)\boldsymbol{P^{NL}}. \tag{1.13}$$

Therefore, the ***nonlinear wave equation*** becomes:

$$\nabla^2 \boldsymbol{E} - \mu\sigma \left(\frac{\partial}{\partial t}\right)\boldsymbol{E} - \mu\varepsilon\left(\frac{\partial^2}{\partial t^2}\right)\boldsymbol{E} = \mu\left(\frac{\partial^2}{\partial t^2}\right)\boldsymbol{P^{NL}} \tag{1.14}$$

$$\nabla^2 \boldsymbol{E} + \frac{1}{c^2}\left(\frac{\partial^2}{\partial t^2}\right)\boldsymbol{E} = \frac{-1}{c^2\varepsilon}\left(\frac{\partial^2}{\partial t^2}\right)\boldsymbol{P^{NL}}. \tag{1.15}$$

The equation is inhomogeneous, and the nonlinear response of the medium represents the source term, which is included as the right-hand term. This means that $\boldsymbol{P}$ drives the electric field $\boldsymbol{E}$. This is responsible for many nonlinear optical phenomena like second harmonic and higher harmonic generation, sum and difference frequency generation, etc.

Second order effects are primarily parametric in nature (interactions between light waves and matter do not involve transfer of energy to, or from, the medium). They are in general called three wave-mixing and include:

- Second harmonic generation (SHG) $\left[\chi^{(2)}(2\omega;\omega,\omega)\right]$
- Optical refraction $\left[\chi^{(2)}(0;\omega,-\omega)\right]$
- Parametric mixing $\left[\chi^{(2)}(\omega_1 \pm \omega_2;\omega_1 \pm \omega_2)\right]$

- Pockel's effects $\left[\chi^{(2)}(\omega;\omega,0)\right]$

These phenomena occur through electric dipole interactions. Because of symmetry restrictions, the even order electric dipole susceptibilities are zero in materials with optical inversion symmetry. As a result, the second order nonlinear interactions are observed most commonly only in certain classes of crystals which lack center of inversion. However, some second order processes (due to electric quadrupole interactions) have been observed in gases and in solids that have center of inversion. The second order frequency conversion process is primarily used to produce coherent radiation in wavelength regions where radiation from direct laser sources is not available, or to obtain radiation in a given wavelength range with properties, such as tunability, that are not available with existing direct laser sources[22]. Radiation ranging from 185 nm (ultraviolet) to 2 μm (microwave) has been generated with different crystals and lasers.

The third order effects involving $\chi^{(3)}$ do take place in all materials irrespective of their possessing inversion symmetry. Third order parametric processes are also used for frequency conversion. They have been used to generate radiation ranging from 35 nm, almost in the soft x-ray range to 25 μm in the infrared. Third order processes can be observed with electric dipole interactions in materials with any symmetry, such as gases, liquids, and some solids. Since, these materials have the lowest order non-zero nonlinearities allowed by electric dipole interactions. Some important third order effects are:

- Third harmonic generation (THG) $\left[\chi^{(3)}(3\omega;\omega,\omega,\omega)\right]$

- Optical Kerr effect $[\mathrm{Re}\,\chi^{(3)}(\omega;\omega,0,0)]$
- Non-degenerate four-wave mixing $[\chi^{(3)}(\omega_1+\omega_2\pm\omega_3;\omega_1,\omega_2,\pm\omega_3)]$
- Stimulated Raman scattering (SRS) $[\chi^{(3)}(\omega\pm\Omega;\omega,-\omega,\omega\pm\Omega)]$
- Stimulated Brillouin Scattering (SBS) $\left[\chi^{(3)}\left(\omega\pm\Omega;\omega,-\omega,\omega\pm\Omega\right)\right]$
- Degenerate four-wave mixing $[\mathrm{Re}\,\chi^{(3)}(\omega;\omega,-\omega,\omega)]$
- Two photon absorption (2PA) $[\mathrm{Im}\,\chi^{(3)}(\omega;\omega,-\omega,\omega)]$
- DC induced harmonic generation $[\mathrm{Re}\,\chi^{(3)}(2\omega;\omega,\omega,0)]$

SBS[23], SRS[24], [25] and degenerate four wave-mixing processes are widely used third order techniques for generating phase conjugate beams. The magnitude and the response of these higher order effects can be compared only by evaluating their corresponding nonlinear coefficients χ^2, χ^3, etc. The χ^2 term is present only in non-centrosymmetric materials possessing inversion symmetry[26]. Therefore, materials that are isotropic and homogeneous (such as liquids & gases) have the lowest nonlinear response as the third order nonlinear processes. Thus this third order effect is widely investigated.

From the above discussion, one can invariably understand that the determination of the magnitude and response of third-order nonlinear susceptibility are vital parameters in characterizing and quantifying the applicability of any material as a nonlinear optical device. In general, the nonlinear index of refraction is defined as a variation of the index of refraction of the material caused by the intensity of light waves propagating through the medium. The third order nonlinear susceptibility is related to the nonlinear index of

refraction, similar to the relationship of the linear susceptibility to the linear index of refraction.

The intensity dependent nonlinear refractive index for an isotropic centrosymmetric material with a third order nonlinearity is given as,

$$n = n_0 + n_2 I\,, \tag{1.16}$$

where n_2 is the contribution to change in the refractive index due to χ^3 as we have $I \propto E^2$. This nonlinear contribution to the refractive index causes the phenomena of self-action. It is called self-action since the nonlinear polarization caused by the incident beam affects the propagation of the beam through the medium. In the case of a Gaussian beam where the beam is more intense at the center than at the edges, and if the material has a positive nonlinear refractive index, then the medium acts as a positive lens focusing the beam. If the material has a negative nonlinear refractive index, then the material acts as a negative lens. As in the case of the refractive index the nonlinear absorption coefficient is given as

$$\alpha = \alpha_0 + \beta I\,, \tag{1.17}$$

where α_0 is the linear coefficient of absorption and β is the nonlinear coefficient of absorption. Such nonlinear processes occur in a nonlinear material only when the optical field incident on the material is quite strong, i.e., at high intensities.

The third order susceptibility can be considered as combination of real and imaginary parts as

$$\chi^3 = \chi_R^3 + \chi_I^3. \tag{1.18}$$

The real part χ_R^3, accounts for all the effects that are transient and consume no energy such as molecular orientation, electrostriction, *etc*. The imaginary part χ_I^3, accounts for

processes that involve losses such as the one due to bleaching, nonlinear absorption, etc. The most important χ^3 processes for optical limiting are nonlinear absorption and the electronic Kerr effect, which are respectively associated with the imaginary part of χ^3 and the real part of χ^3.

A Feynman diagram is useful for picturizing corresponding physical processes when photons are absorbed or emitted,[27] which can be used to evaluate a nonlinear process to various orders of perturbation. It also allows one to write down a mathematical expression associated with that particular process. Thus it is a convenient tool for evaluating complicated higher order nonlinear optical responses.

The elements of a Feynman diagram include:

• a wavy line representing a photon

• a vertex representing absorption (or emission) of a photon

• a diagonal line representing a specific state

• a vertical line representing many possible states which do not necessarily conserve energy through a vertex

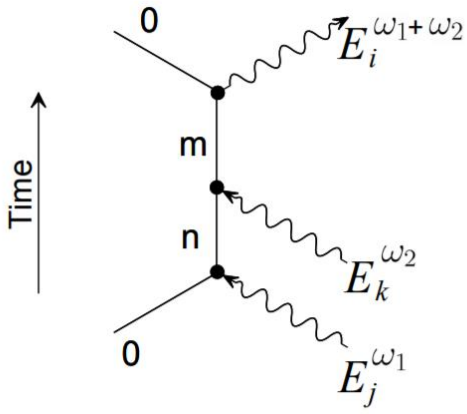

Fig. 1.2. Feynman diagram of sum frequency generation. This can represent two photon absorption if $\omega_1 = \omega_2$.

1.2 Nonlinear Absorption

Nonlinear absorption refers to the nonlinear change in the material transmittance as a function of input laser light fluence (usually given in units of J/cm^2). As mentioned above, the nonlinear absorption coefficient of a third-order nonlinear medium can be written as $\alpha = \alpha_0 + \beta I$, where β is the nonlinear coefficient of absorption. β usually refers to two-photon absorption coefficient. However, two-step phenomena like excited state absorption (ESA) and free carrier absorption (FCA) may also contribute to nonlinear absorption. Such phenomena are collectively referred to as reverse saturable absorption (RSA).

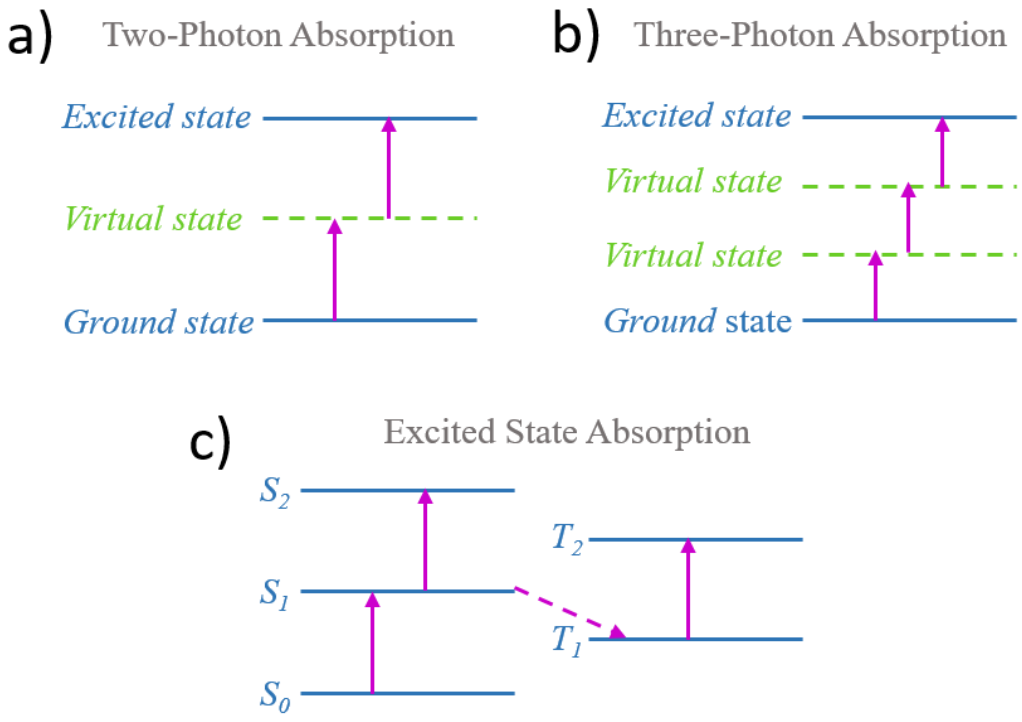

Figure 1.3. A schematic diagram of a) two-photon absorption, b) three-photon absorption and, c) excited state absorption. The blue solid lines represent real states and the green dashed lines represent virtual states, purple arrows represent electronic transitions.

1.2.1 Multiphoton absorption

In an insulator or semiconductor, due to the conservation of energy, linear electronic absorption can occur only if the photon energy is equal or greater than the bandgap energy. However, at high optical intensity it is possible to bridge the bandgap by simultaneous absorption of two or more lower-energy photons, only if the sum of photon energies exceeds the bandgap energy. Such processes are called multiphoton absorption (MPA)[28]. Many semiconducting and insulating nanomaterials exhibit MPA[29]. Since two- and

three-photon absorption (2PA and 3PA, respectively) processes are more common, we limit our discussion of MPA to these two cases. As shown in Fig. 1.3a, 2PA involves the simultaneous absorption of two photons to promote an electron from an initial state to a final state through a virtual intermediate level (represented by green dashed lines). With usually a lower transition probability, 3PA (see Fig. 1.3b) involves three photons and two intermediate states. Since the intermediate level is virtual, energy only needs to be conserved in the final state. MPA is an instantaneous process occurring in femtosecond timescales. Two- and three- photon absorption-based nanomaterials can be used for applications such as frequency conversion lasing, optical limiting, pulse stabilization, and reshaping. By assuming only one type of MPA dominates at any given time, the optical intensity I can be described as[10]:

$$\frac{dI}{dz} = -\alpha I - \gamma^n I^n, \tag{1.19}$$

where α is the linear absorption coefficient, z is propagation distance of light within the sample and γ^n is the n-photon absorption coefficient. For example, γ^2 represents the 2PA coefficient while γ^3 denotes 3PA. While the rate for linear absorption is simply proportional to the optical intensity, for MPA processes of order n, the absorption rate is proportional to the n^{th} power of the optical intensity. This implies that such absorption rates can be very small for low or moderate optical intensities, but can become dominant for very high optical intensities, which can be achieved with focused laser pulses.

Multiphoton absorption processes in transparent media are often accompanied by laser-induced damage/oxidation. Transparency of such medium means that linear electronic absorption is not possible for the considered optical wavelength; therefore, material remains virtually transparent to light with low optical intensity. However, MPA can become substantial at high enough optical intensity, so that energy can be deposited and a run-away process can start, which ultimately leads to optical damage of the material. This is also exploited in laser material processing on transparent materials such as BN, which is described in details in Chapter 3.

Another example is multiphoton fluorescence microscopy, where MPA (mostly two-photon or three-photon absorption) is often utilized and the excitation light from a femtosecond laser is strongly focused[30]. Compared with linear excitation, the practical advantage of multiphoton excitation is that a laser source with longer emission wavelength can be used, which in some cases is less harmful to live tissues. Also, longer-wavelength light can more easily propagate deeper into the material without being strongly absorbed, as long as the beam radius is large enough. The multiphoton fluorescence microscopy utilizes that intensity which is present only in the beam focus, where the optical intensities are substantially higher, and multiphoton absorption processes become strong. The preferential illumination in the beam focus helps one to obtain a higher longitudinal image resolution and less interference from fluorescence light generated in the beam path[30].

1.2.2 Excited state absorption

The mechanism of excited state absorption (ESA) can be viewed as analogous to a 2PA process with a real intermediate excited state instead of the virtual state, where the electron has sufficient lifetime to stay after been excited from ground state. In this process, the absorption cross section of the intermediate excited state is higher than the ground state, which leads to an enhanced absorption at higher input intensities. Typically, the ESA process is much stronger than 2PA, because the electrons stay at a real state during the excitation process[10]. The excited state absorption exists in fullerene systems, and it can be used in optical limiting due to its strong ESA coefficient [10]. Details will be explained in Chapter 2.

1.2.3 Saturable absorption

Saturable absorption is a property of a material where the transmission of light increases with increasing light intensity. Given sufficiently high intensity of photon-excitation, electrons in the ground state of a saturable absorber can be transferred to an excited state. During the very short time period (picoseconds) before electrons decay back to the ground state, the material stays transparent to the same wavelength of light. With its ground state bleached by the high intensity light beam, the material can no longer absorb additional photons leading to a saturation in its absorption. The key parameters for a saturable absorber are the range of working wavelength, the dynamic response, and its saturation intensity and fluence. Saturable absorbers commonly used for passive Q-switching in laser cavities. In particular, saturable absorption is only one of several mechanisms that produces self-pulsation in lasers, especially in semiconductor lasers[10]. Most materials show some

saturable absorption, but are often limited to higher optical intensities (sometimes close to the optical damage threshold). As described later in this thesis, many 2D materials exhibit strong SA.

The nonlinear light propagation equation is given below as:

$$\frac{dI}{dz} = -\frac{\alpha I}{1+\frac{I}{I_s}}, \tag{1.20}$$

where α is the linear absorption coefficient, I_s is the threshold saturable intensity where the absorption is 50% of linear absorption. To characterize the SA, an open aperture Z-scan is usually employed, which is explained in section 1.4 of this chapter.

Semiconducting materials can only absorb photons of energy equal or higher than its energy band gap. However, graphene is a gapless semiconductor with unique electronic properties where charge carriers show linear dispersion relation for visible light (less than 3 eV).[31] This enables graphene to function as a wide bandwidth saturable absorber. The optical nonlinearities are directly related to photocarrier density and carrier relaxation time. As shown in Fig. 1.4, the saturable absorption process can be depicted as follows. Absorption of light in graphene first leads to the electron excitation from its valence band to conduction band. When first arrived at conduction band, the hot electrons undergo a cooling process and attain a Fermi-Dirac distribution. The hot electrons can be further cooled through intraband phonon scattering, and eventually the electrons and holes recombine. If graphene is exposed to an intense light beam, the photo-generated carriers will quickly fill the band edge states and graphene will be unable to further absorb light; or in other words graphene attains the state of saturation absorption. As electron must obey

Pauli's principle, the photo-generated carrier prevent graphene from further absorption of photons, a property also known as Pauli blocking. Under low intensity light illumination, graphene exhibits a strong absorption of light. As the light intensity increases, graphene attains a state of saturation absorption and become transparent. This principle has been used in Q switching and mode-locking applications[8], [32].

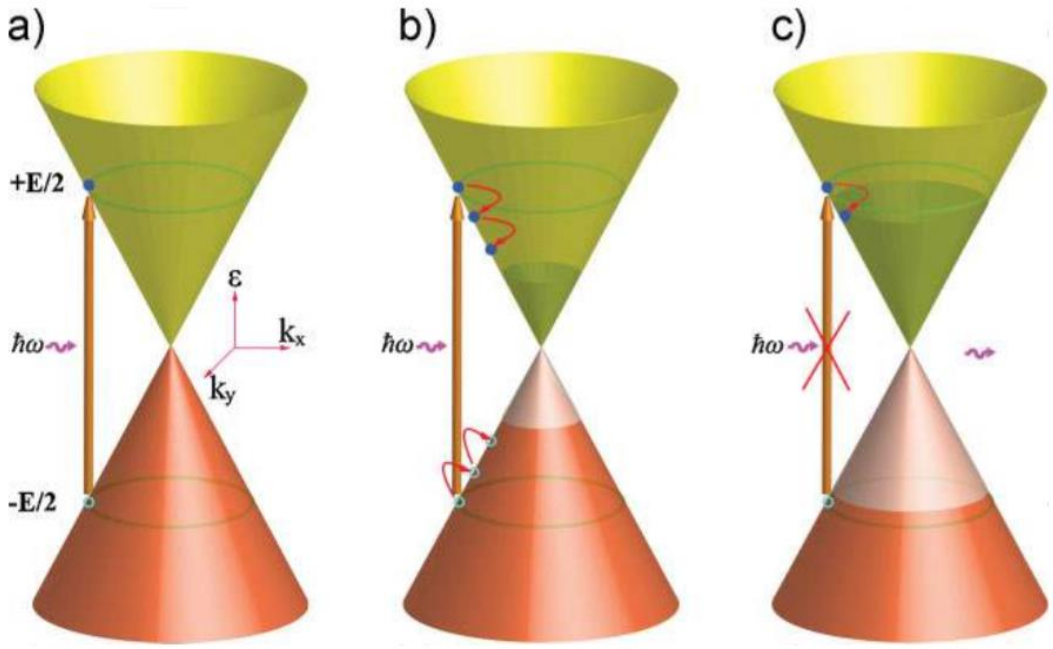

Figure 1.4. Saturable absorption process in graphene. a) Schematic of the excitation process responsible for absorption of light in graphene. The vertical arrow indicates optical interband transition. b) The photo-generated carriers thermalize and cool down within sub-picoseconds to form a hot Fermi–Dirac distribution. An equilibrium electron and hole distribution is attained through intraband phonon scattering and electron-hole

recombination. c) At high excitation intensity, the photo-generated carriers cause the states near the edge of the conduction and valence bands to fill, blocking further absorption. [32]

1.3 Nonlinear Refraction

Nonlinear refraction is described by the second term n_2 of the equation 1.16. It represents the material's refraction index that responds to light intensity nonlinearly. The dominant physical mechanism driving nonlinear refraction in a given medium can vary depending on the material, which is usually caused by optical Kerr effect. When a focused beam passes through the materials, a light intensity dependent refraction index is developed. The material will exhibit a spatially uneven distribution of refracted light, and the effect is equivalent to that of a lens and is also referred to as Kerr lensing. The nature of Kerr lensing is used in several applications including optical switching and laser mode-locking, especially in the ultrafast regime.

Nonlinear refraction can also occur due to thermal effects (usually referred to as thermal lensing), which is typically caused by the laser beam heating at the focal point, it builds up with a relatively long response time of a few milliseconds. Thermal nonlinearity can be dominant for continuous-wave (cw) laser excitation and significant for nanosecond laser pulse excitation. The nonlinear index of refraction can be determined using a closed aperture Z-scan measurement.

1.4 Experimental setup

The Z-scan technique is a sensitive and simple method for measuring nonlinear absorption and nonlinear refraction properties of a material. It has been used extensively to study the optical nonlinearity of various materials like semiconductors, nanocrystals, semiconductor-doped glasses, liquid crystals, organic materials, and biomaterials. Introduced by Sheik-Bahae et al.[10], [33] in the early 1990s, this widely used technique has many advantages over other nonlinear spectroscopic methods. In a typical Z-scan, the light-induced change in transmittance of the material due to optical nonlinearity is measured as a function of input light energy density (fluence) or intensity. A continuous variation of the input fluence is achieved by translating the sample under study (translation direction is along the z direction) through the focal region ($z = 0$) of a focused laser beam, and hence the name "Z-scan"). As the sample is translated in and out of the focal region, it is subjected to a consequent increase and decrease of the incident light intensity, resulting in wave front distortions (created by nonlinear optical effects in the sample). There are two types of Z-scan techniques, namely, the "closed aperture" Z-scan and the "open aperture" Z-scan. In the open aperture Z-scan, which is used for studying nonlinear absorption, the transmitted beam is collected by a detector, for different values of sample position z. In the closed aperture Z-scan, which is used for studying nonlinear refraction, the transmitted beam is passed through an aperture placed in the far field and then measured by a detector.

1.4.1 Open aperture Z-scan

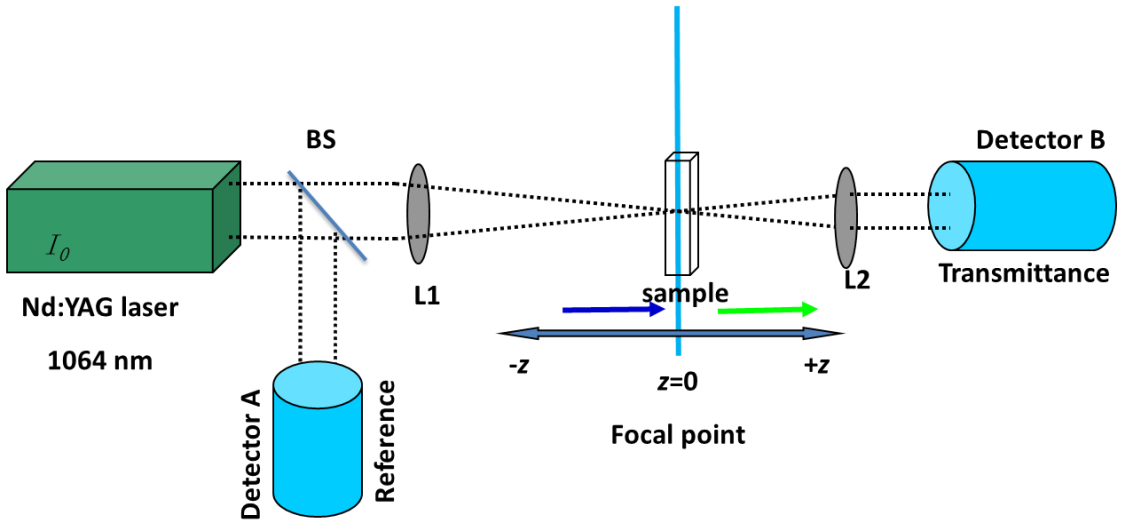

Figure 1.5. A schematic illustration of an open aperture Z-scan setup.

All Z-scan measurements described in this thesis were performed with linearly polarized 7 ns optical pulses from a Q-switched frequency-doubled Nd:YAG laser at 1064 nm. In our open aperture Z-scan setup (see Fig. 1.5), the laser beam was focused by a converging lens with a focal length of 20 cm on to a stable dispersion that was held in the 1 mm quartz cuvette (100-QS Hellma® Analytics) or a solid thin film and translated across the focal plane ($z = 0$) in the beam direction (z direction). At each z position, the position dependent transmittance was measured using a calibrated photodetector B (RjP-7620, Laserprobe, Inc.). A similar detector A was used for measuring the reference signal, and the sample signal was computed as the ratio of intensity measure by B compared to that of A (in order to minimize the influence from the laser intensity fluctuation). The open

aperture Z-scan is sensitive only to nonlinear absorption (NLA), which is the intensity induced transmission change. The absorptive nonlinearity will be maximum at the focal plane, where the intensity is highest. Thus, the open aperture scheme is employed to characterize materials that exhibit NLA, such as excited state absorption, two-photon absorption and saturable absorption.

1.4.2 Closed aperture Z-scan

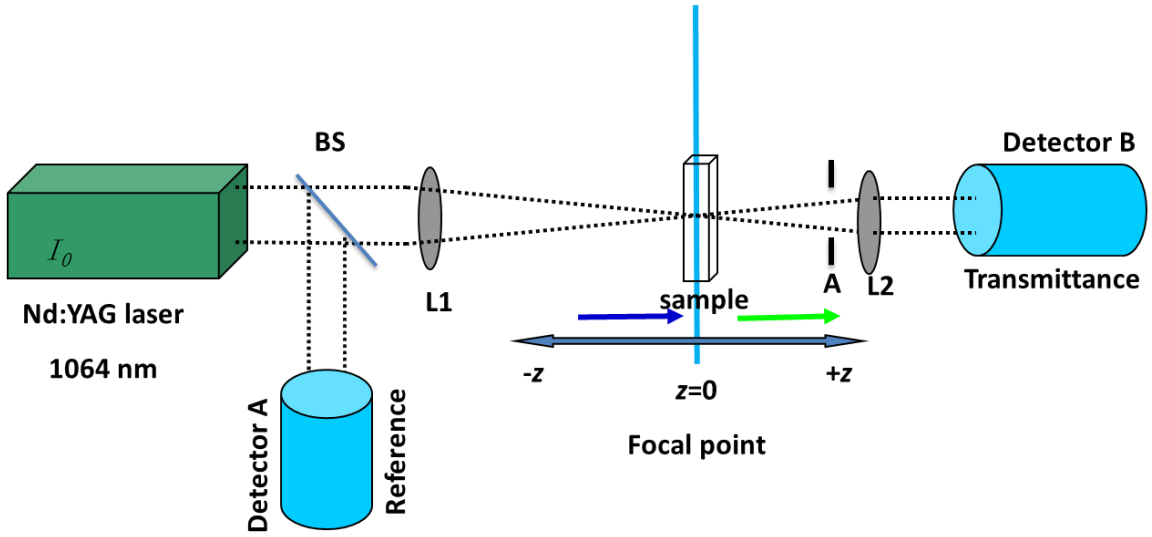

Figure 1.6. A schematic illustration of closed aperture Z-scan setup. A is for aperture.

Instead of using a lens to collect all the transmitted light, in a closed aperture Z-scan setup an aperture is used to selectively let the light pass at a certain solid angle (see Fig. 1.6). The sensitivity to nonlinear refraction results from the vital role played by aperture (Fig. 1.6). Even though closed aperture Z-scan is used mainly for measuring NLR properties, in practice, depending on the nature of the sample the closed aperture Z-scan data may also

contain contributions from NLA. To obtain the NLR coefficient in such a case, it is sufficient to normalize the closed aperture data using the open aperture data before analysis.

CHAPTER TWO

NONLINEAR OPTICAL PROPERTIES OF FULLERENES

Yongchang Dong, *et al*. "Passive Optical Switches Based on Endohedral Fullerenes". *Optical Materials* (2016) 53: 14–18. Reproduced in part with permission of Elsevier.

2.1 Excited state absorption in nanomaterials

As digital information technologies continue to evolve at much faster rates than the growth of Si-based processors, the encroachment of light-based technologies into computing seems inevitable.[34]–[36] With the advent of lasers, photonic crystals, and optical diodes[36], [37] photonic computing has made significant strides in information technology over the past 30 years. This continuing integration of light into all-optical computing, optoelectronic components, and emerging optogenetic technologies demands the ability to control and manipulate light in a predictable fashion, or by design.[38] Although there are different dynamic methods (e.g., Faraday rotator) to manipulate light, the presence of multiple optical components and the necessity for active feedback/control (e.g., magnetic fields in Faraday rotator) impedes their immediate utilization in many technologies.[38] Alternatively, passive control and manipulation of light in all-optical switches, photonic diodes, and optical limiting could be achieved by directly using intrinsic non-linear optical properties of materials[37], [38]. Of particular interest, in this chapter, is the use of all-optical switches and optical limiters for laser pulse-shaping and sensor protection. While an ideal optical switch is a nonlinear optical device that abruptly turns opaque (zero transmission) above a certain threshold intensity, an ideal optical limiter

exhibits a linear (/non-zero and constant) transmission below (/above) the threshold (Fig. 2.1). In reality, when the leading edge of a fast optical pulse is comparable to the electron-electron scattering times (hundreds of fs to sub-ps) of the optical switch material, the pulse may partially pass through the optical switch material before the material is non-linearly activated[38]–[40]. This yields a realistic switch/limiter response that is intermediate between an ideal limiter and an ideal switch, as shown in Fig. 2.1.

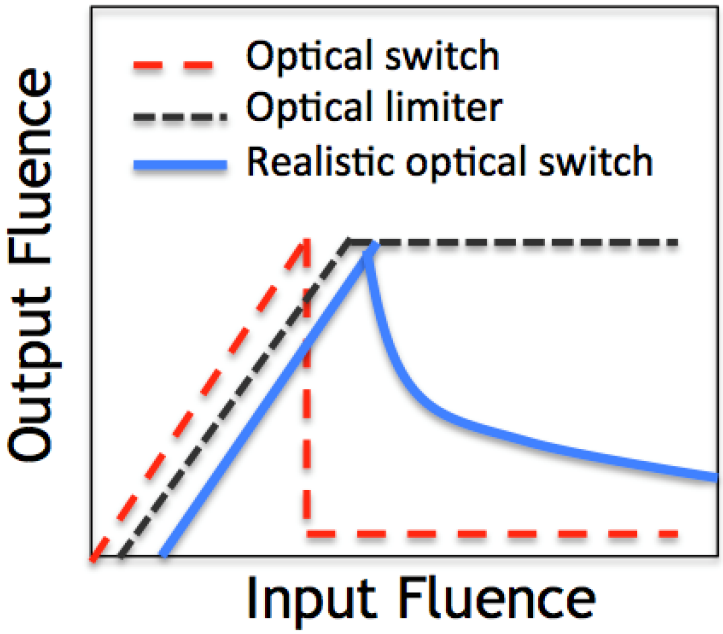

Fig. 2.1. A schematic showing the optical response of an ideal optical limiter (dashed black line), an ideal optical switch (red dashed line), and a realistic passive optical switch as a function of input fluence.

Table 2.1. Optical limiting threshold of various low dimensional nanostructures in comparison with $Sc_3N@C_{80}$, $Lu_3N@C_{80}$, $Y_3N@C_{80}$ and C_{60}.

Nanostructure (diameter size)	Pulse width: sample length	Linear transmission (%)	Threshold value (J/cm^2)	Reference
Pd nanowires (50nm)	7ns:1mm	80	0.9	Pan et al.[41]
Cu nanowires (50nm)	8ns:5mm	80	2.5	Pan et al.[41]
Ni nanowires (50nm)	7ns:1cm	80	1.2	Pan et al.[41]
Pt nanowires (50nm)	7ns:1cm	80	1.3	Pan et al.[41]
Ag nanowires (50nm)	7ns:1cm	80	1.7	Pan et al.[41]
Co nanowires (50nm)	7ns:1cm	80	4.2	Pan et al.[41]
CdS nanowires (4.5nm)	6ns:1mm	76	1.42 to 0.42	Muthukumar et al. [42]
CdS/Ag_2S nanoparticles (3.5nm)	4.1ns:2mm	68	0.5	Jia et al.[43]
Au NPs (22nm)	7ns:1mm	70	9.0	Pradhan et al.[44]
Au-graphene	7ns:1mm	70	0.4	Pradhan et al.[44]
C_{60} (0.7nm)	7ns:1mm	80	1.0	This work
$Sc_3N@C_{80}$ (0.7nm)	7ns:1mm	75	0.5	This work
$Lu_3N@C_{80}$ (0.7nm)	7ns:1mm	80	0.3	This work
$Y_3N@C_{80}$ (0.7nm)	7ns:1mm	80	0.4	This work

Realistic optical switches/limiters are useful in several applications, some of which include: i) pulse shaping where a long optical pulse with intensity spikes can be smoothed by selectively attenuating the high-intensity spikes that exclusively elicit non-linear responses in the switch[38], and ii) sensor protection for extending the dynamic range of the sensor by mitigating light-induced damage.[38], [43]–[47] With regards to sensor protection, the extensive deployment of lasers poses a serious threat for sensitive optical and electronic components/devices including eyes, now more than ever. Indeed, the strong absorption of biomolecules in the near-infrared (NIR) region exacerbates the possibility of NIR laser-induced injuries and accidents, making the need for effective protection against lasers a priority.[48], [49] The emergence of various nanomaterials and their heterostructures with unique non-linear properties (e.g., reverse saturable absorption in C_{60}) led to the realization of enhanced optical limiting materials.[39], [41]–[47], [50]–[57] Although nanomaterials display an improved optical limiting threshold (the input fluence at which the transmittance falls to 50% of its initial value) at higher input fluences >1 J/cm^2 (Table 1.1), it is challenging to achieve excellent optical limiting capability in the low fluence regime (<1 J/cm^2).[44] Furthermore, realistic optical switches should also exhibit a rapid decrease in transmission (ideally, the transmission should abruptly drop to zero above the threshold intensity, as shown in Fig. 2.1) in addition to a low-threshold.[38] In this regard, others and we previously found that tailoring the electronic band structure of nanomaterials via dopants & defects (e.g., oxidized graphene/B- or N-doping), and modulating electron scattering mechanisms through heterostructured geometries (e.g., Au nanoparticles of reduced graphene oxide) shows excellent promise for controlling non-

linear optical properties.[44], [58]–[61] Building on these results, in this article, we demonstrate the use of thermally stable endohedral cluster fullerenes ($Sc_3N@C_{80,}$ $Lu_3N@C_{80}$ and $Y_3N@C_{80}$) as potential passive realistic optical switch/limiter materials with low-fluence threshold and high-damage limits for pulsed ns 1064 nm wavelength. The excellent match between the HOMO-LUMO gap energy in $Lu_3N@C_{80}$ and 1064 nm excitiation energy leads to the realization of a threshold as low as ~0.3 J/cm^2, which is at least an order of magnitude lower compared to that exhibited by many nanomaterials, particularly C_{60} (Table 1.1). More importantly, the non-linear transmission through $Lu_3N@C_{80}$ decreases much more rapidly than for other nanomaterials, making it an ideal candidate for realistic optical switching. In addition to the low-fluence, our experiments show that $Sc_3N@C_{80,}$ $Lu_3N@C_{80}$, and $Y_3N@C_{80}$ can withstand high nanosecond pulsed-laser energies >0.5 mJ (average pulse energy) which is at least 10-100 times higher than for other metallic and dielectric materials[62], [63] and is on par with high-power Er/Yb doped optical fibers.[64]–[67]

2.2 Characterization of endohedral fullerenes

C_{60} (Carbon 60, 99.95+ %, ultra pure Vacuum oven dried) was purchased from SES research, Houston, TX. $Sc_3N@C_{80,}$ $Lu_3N@C_{80}$ and $Y_3N@C_{80}$ were obtained using an arc-discharge process described earlier.[68] To gauge the non-linear optical performance of C_{60}, $Sc_3N@C_{80,}$ $Lu_3N@C_{80}$ and $Y_3N@C_{80}$ we used a conventional open aperture Z-scan technique described in Chapter 1.[44], [69] All measurements were performed with linearly polarized 7 ns optical pulses from a Q-switched frequency-doubled Nd:YAG laser at 1064

nm. For our Z-scan setup, the laser beam was focused by a converging lens with a focal length of 20 cm on to a stable dispersion that was held in the 1 mm quartz cuvette (100-QS Hellma® Analytics) and translated across the focal plane in the beam direction (*z* direction). At each *z* position, the position dependent transmittance was measured using a calibrated photodetector (RjP-7620, Laserprobe, Inc.) to obtain the Z-scan curves shown in Figs. 2.2 and 2.3. C_{60}, $Sc_3N@C_{80}$, $Lu_3N@C_{80}$ and $Y_3N@C_{80}$ were suspended in toluene at 0.5 mg/ml concentration using aqueous bath sonication (Branson Aquasonic) for 30 minutes.

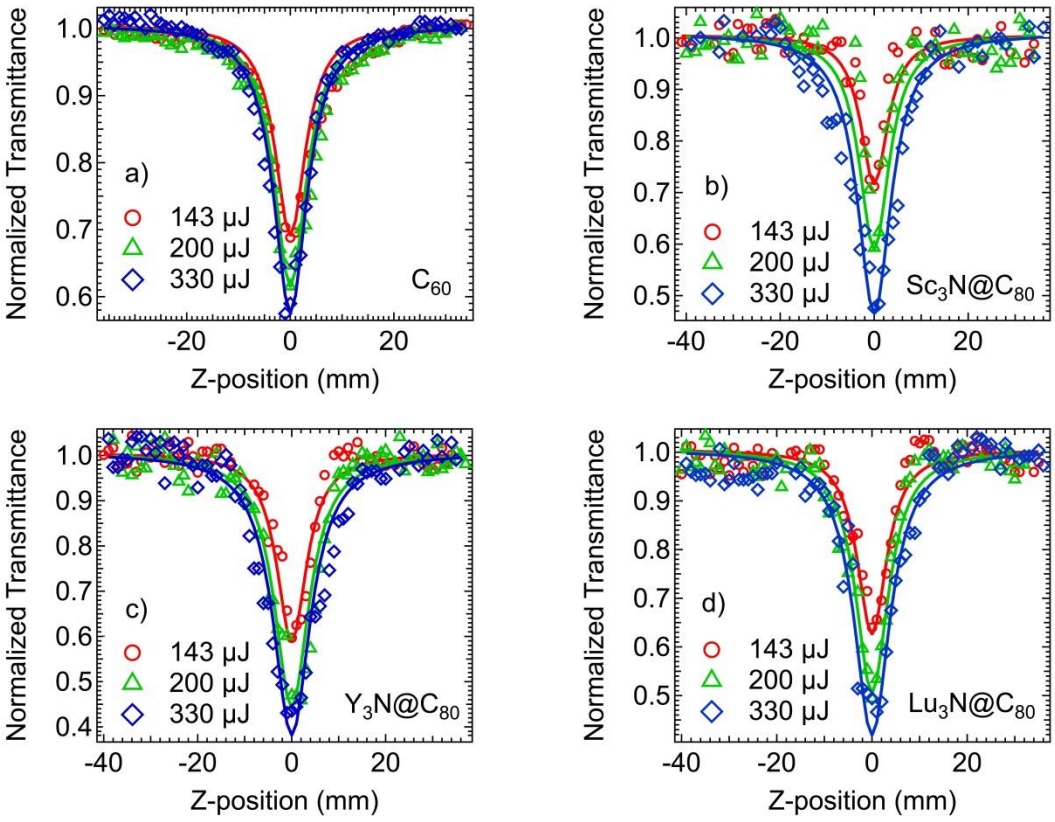

Fig. 2.2. Z-scan curves for C_{60} (a) and $Sc_3N@C_{80}$ (b) at different energies clearly show a valley indicating reverse saturable/two-photon response. The markers represent the experimental data and the solid lines are experimental fits obtained by solving a non-linear light propagation equation (cf. eqn. 2.2).

2.3 Excited state absorption in endohedral fullerenes

The open aperture Z-scan curves (shown in Fig. 2.2) often emerge from one or multiple non-linear phenomena (e.g., saturable, reverse saturable, or multi-photon absorption) occurring simultaneously in the photo-excited material under study. For instance, the nonlinear transmission for a sample exhibiting exclusively reverse saturable or two-photon absorption (RSA or 2PA) processes (e.g., C_{60} in Fig. 2.2a) is given by equation (1)

$$T = (1-R)^2 e^{\frac{-\alpha_0 L}{\sqrt{\pi} q_0}} \int_{-\infty}^{+\infty} ln(1 + {q_0}^2 e^{-t^2}) dt \tag{2.1}$$

where L and R are the sample length (1 mm) and surface reflectivity, respectively. In eqn. 2.1, α_0 is the unsaturated linear absorption coefficient, q_0 is given by $\beta(1-R)I_0 L_{\text{eff}}$, where β is the absorption coefficient for a RSA/2PA process. The effective length L_{eff} is given by $(1-\exp(-\alpha_0 L))/\alpha_0$. For materials that simultaneously exhibit more than one NLO process, such as saturable absorption competing with a RSA/2PA process (e.g., $Sc_3N@C_{80}$, $Lu_3N@C_{80}$ and $Y_3N@C_{80}$ in Fig. 2.2b, c, d), the nonlinear transmission of the sample is best described by the propagation equation as

$$\frac{dI}{dz'} = -\frac{\alpha_0 I}{1+\frac{I}{I_s}} - \beta I^2, \tag{2.2}$$

where I_s is the saturation absorption intensity. RSA is a non-linear optical phenomenon, which occurs when the photoexcited state exhibits higher absorption cross-section than the ground state. As shown in Fig. 2.2a, it is well known that C_{60} exhibits RSA,[39], [45], [56] when exposed to ns pulses, due to the excitation of ground-state electrons (in singlet state S_o) to the long-lived lowest triplet state T_1 (which has a higher absorption cross-section than S_o) through a fast and efficient intersystem crossing via a singlet state S_1. Our Z-scan curves for C_{60} (Fig. 2.2a) could be fitted well using a two-photon absorption process (eqn. 2.1) with β~4.5 x 10^{-9} cm/W, concurring with the previously observed properties of C_{60}.[70] Although the strong linear optical absorption of S_o-S_1 states (see Fig. 2.3a) leads to efficient RSA and optical limiting up to ~650 nm, the optical switching/limiting behavior of C_{60} is poor for near-infrared wavelengths such as 1064 nm (1.16 eV): a very commonly used ns pulsed laser wavelength.[71] To overcome this apparent challenge, we used Trimetallic Nitride Endohedral Fullerenes (TNEFs) which exhibits a HOMO-LUMO gap ~1.9-2.1 eV that can near-resonantly couple to 1064 nm (~1.16 eV) through 2PA.[68] The difference in linear absorption characteristics of TNEFs and C_{60} is clearly evident from the photographs of C_{60} and TNEFs solutions in toluene shown in the inset of Fig. 2.3a. Previously, it was demonstrated that the electronic structure of fullerenes could be modified through nitrogen, alkali and rare-earth alkali metals doping or by the encapsulation of endohedral atoms/clusters to achieve exotic quantum states of matter such as superconductivity.[72]–[74] These changes in the electronic properties could then also be used to realize passive optical switches, as demonstrated in Fig. 2.3b. The Z-scan curves for $Sc_3N@C_{80}$, $Lu_3N@C_{80}$ and $Y_3N@C_{80}$ (Fig. 2.2b-d) exhibited 2PA with some saturable

absorption (i.e., higher transmittance at non-linear intensities) with high I_s values (numerically fitted using eqn. 2). The 2PA coefficient β for $Sc_3N@C_{80}$ was found to be ~$5x10^{-9}$ cm/W, (for $Lu_3N@C_{80}$ ~$6x10^{-9}$ cm/W and $Y_3N@C_{80}$ ~$7x10^{-9}$ cm/W) which are higher than that of C_{60}. This increase in β may be attributed to the lower HOMO-LUMO gap of $Sc_3N@C_{80}$, ~1.9 eV[68], $Lu_3N@C_{80}$, ~2.05 eV, and $Y_3N@C_{80}$, ~2.04 eV compared to that for C_{60}, ~2.48 eV. It should be noted that the HOMO-LUMO gaps were obtained from the density functional theory calculations described in Ref. 29. The non-linear transmission of TNEFs decreases much more rapidly than for C_{60} (Fig. 2.3b) closer to the behavior of a realistic optical switch (Fig. 2.1). This rapid change in non-linear transmission could plausibly be attributed to: i) fast carrier relaxation rates (~ 100 ps resulting from the presence of tri metallic nitrides) compared to C_{60} (1.5 ns),[75] which in turn can lead to multiple excitation/de-excitations within the ns pulse width, and ii) the charge transfer between photo-excited fullerene cage to Sc_3N which rapidly depletes the excited state population to promote more electrons from the ground state through photo-excitations.[76] A very weak saturable absorption component (I_s ~10^{13}-10^{14} W/m2) was observed for $Sc_3N@C_{80}$ (Fig. 2.3b). Previously, Chemla *et al.* proposed that I_s in quantum wells and dots is mainly determined by a carrier-relaxation time through an inverse relation.[77] Although the exact electronic states involved in saturable absorptions cannot be identified solely through the Z-scan, the high-magnitude of I_s for TNEFs (in particular, $Sc_3N@C_{80}$) suggests that a short-lived LUMO excited state is involved in the saturable absorption, concurring with the data above. Symmetry breaking has been recently observed in the endofullerenes manifesting in the splittings of the three-fold degenerate ground states of

the endohedral[78]. The splitting of the ground states could give rise to the stronger absorption of photon energy between HOMO-LUMO gap. Interestingly, the optical switching/limiting response of TNEFs is highly prominent and exceeds the performance of C_{60} at 1064 nm despite the presence of a saturable absorption component. As shown in Fig. 2.4a, we observed that the linear transmittance at 1064 nm of $Sc_3N@C_{80}$ exhibits a rapid decrease as a function of concentration while it remains fairly in the same range for C_{60} and other TNEFs. This trend indicates possible intermolecular interactions in $Sc_3N@C_{80}$ that could increase the absorption at 1064 nm. In order to account for such concentration dependent effects, we also performed Z-scan experiments (Fig. 2.4b) at similar linear transmittance (~75 ± 5%) for all samples, in addition to the data at 0.5 mg/ml concentration (cf. Fig. 2.2). We found optical limiting in TNEFs ~0.3 - 0.5 J/cm^2 at 75% linear transmission while C_{60} did not exhibit <50% transmittance concurring with the results described in Fig. 2.2 (i.e., at 0.5 mg/ml concentration).

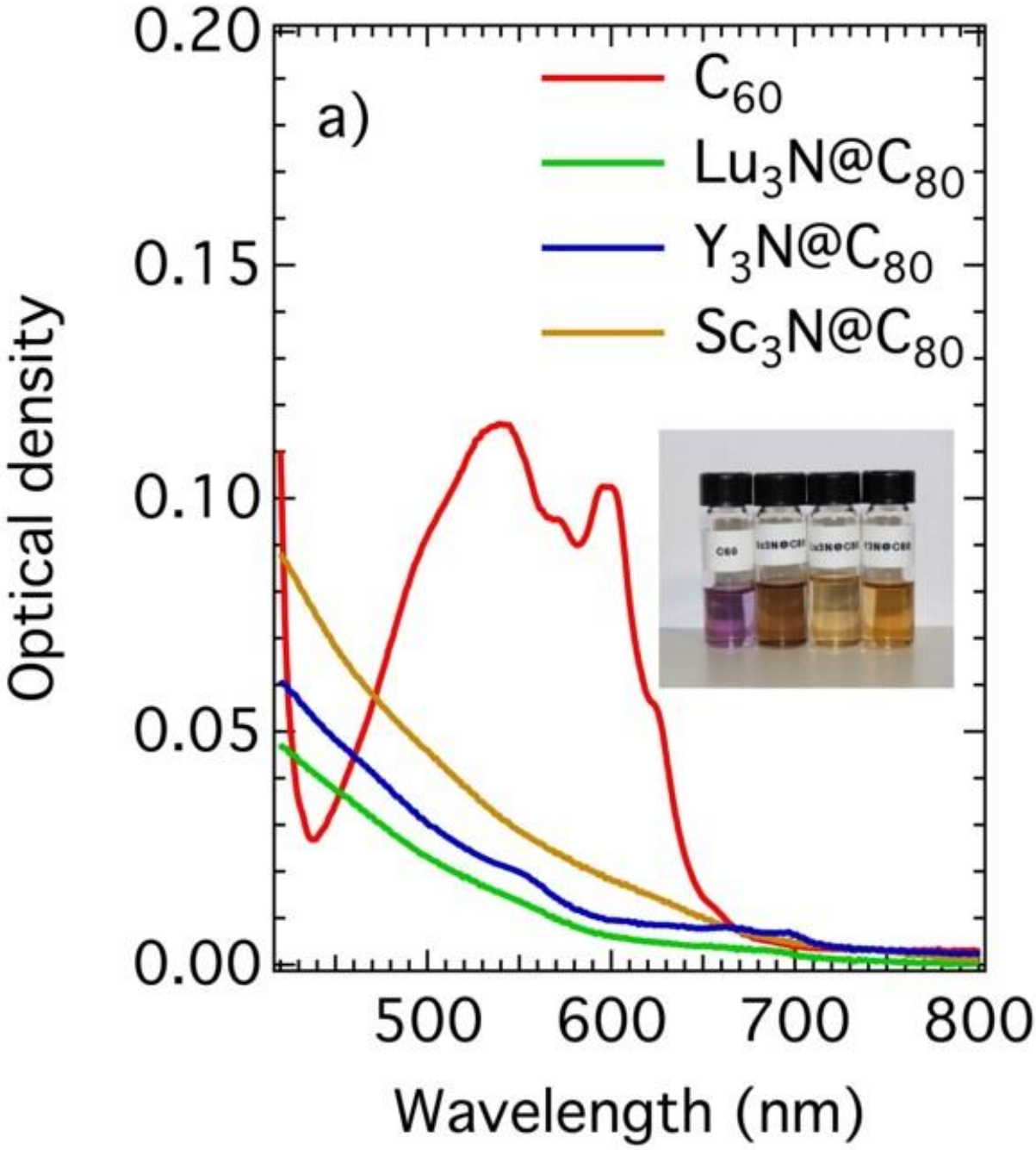
a)
C_{60}
$Lu_3N@C_{80}$
$Y_3N@C_{80}$
$Sc_3N@C_{80}$
Optical density
0.20
0.15
0.10
0.05
0.00
500
600
700
800
Wavelength (nm)

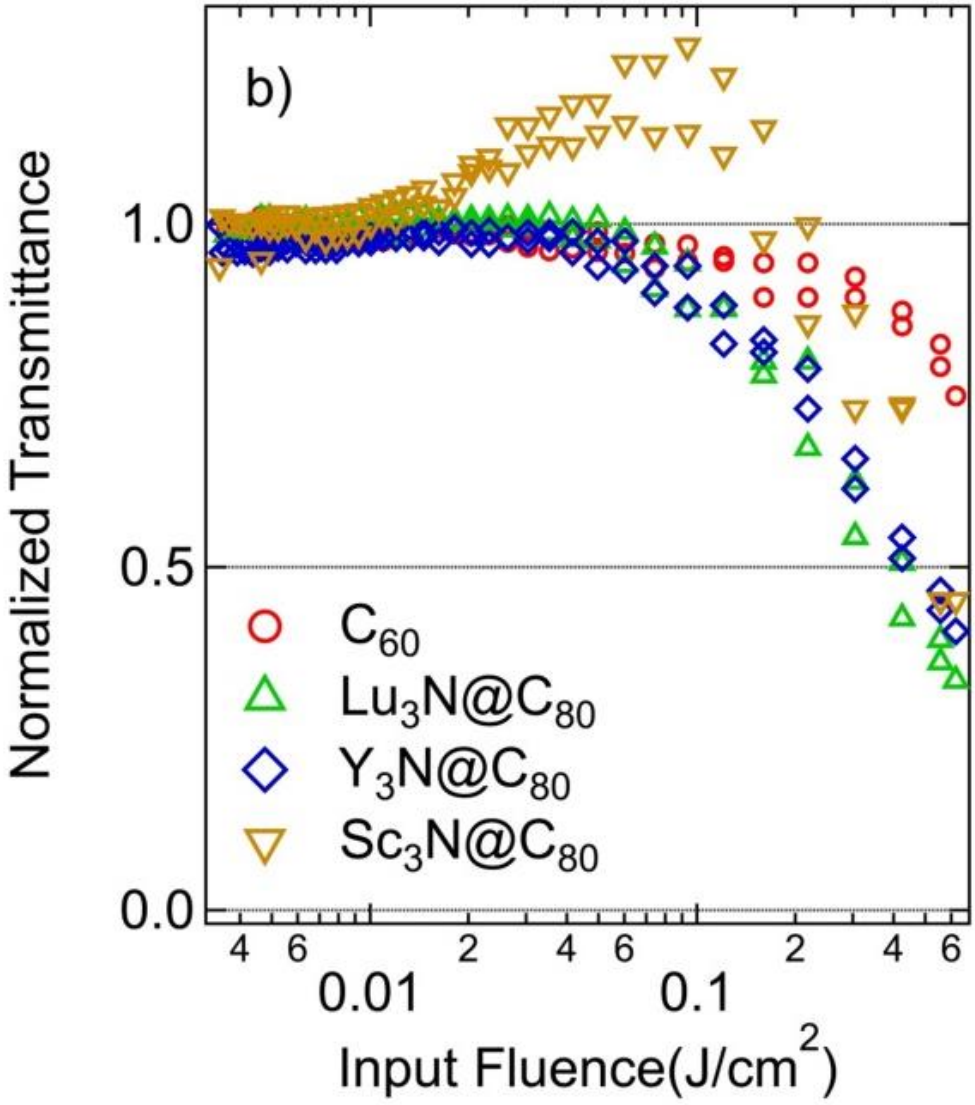

Fig. 2.3. (a) UV-Visible absorption spectrum for C_{60}, $Sc_3N@C_{80}$, $Lu_3N@C_{80}$ and $Y_3N@C_{80}$. The inset shows a digital photograph of C_{60}, $Sc_3N@C_{80}$, Lu_3N and Y_3N (from left to right) exhibiting different colors due to different HOMO-LUMO gaps. (b) The non-linear optical response curve obtained (same concentration, 0.5 mg/ml) using the Z-scan method (1064 nm, 7 ns) shows a rapid decrease in transmission for $Sc_3N@C_{80}$, $Lu_3N@C_{80}$ and $Y_3N@C_{80}$ relative to C_{60} at higher intensities similar to a realistic optical switch (cf.

Fig. 2.1). The dashed line indicates 50% transmittance of the incident light. $Sc_3N@C_{80}$, $Lu_3N@C_{80}$ and $Y_3N@C_{80}$ reach the 50% transmission (shown by dashed line) around a low threshold 0.3~0.5 J/cm^2 while C_{60} does not exhibit optical limiting (i.e., normalized transmittance remains >50%) below 1 J/cm^2. The arrow in (b) shows saturable absorption (normalized transmittance > 100% relative to linear transmittance) for $Sc_3N@C_{80}$.

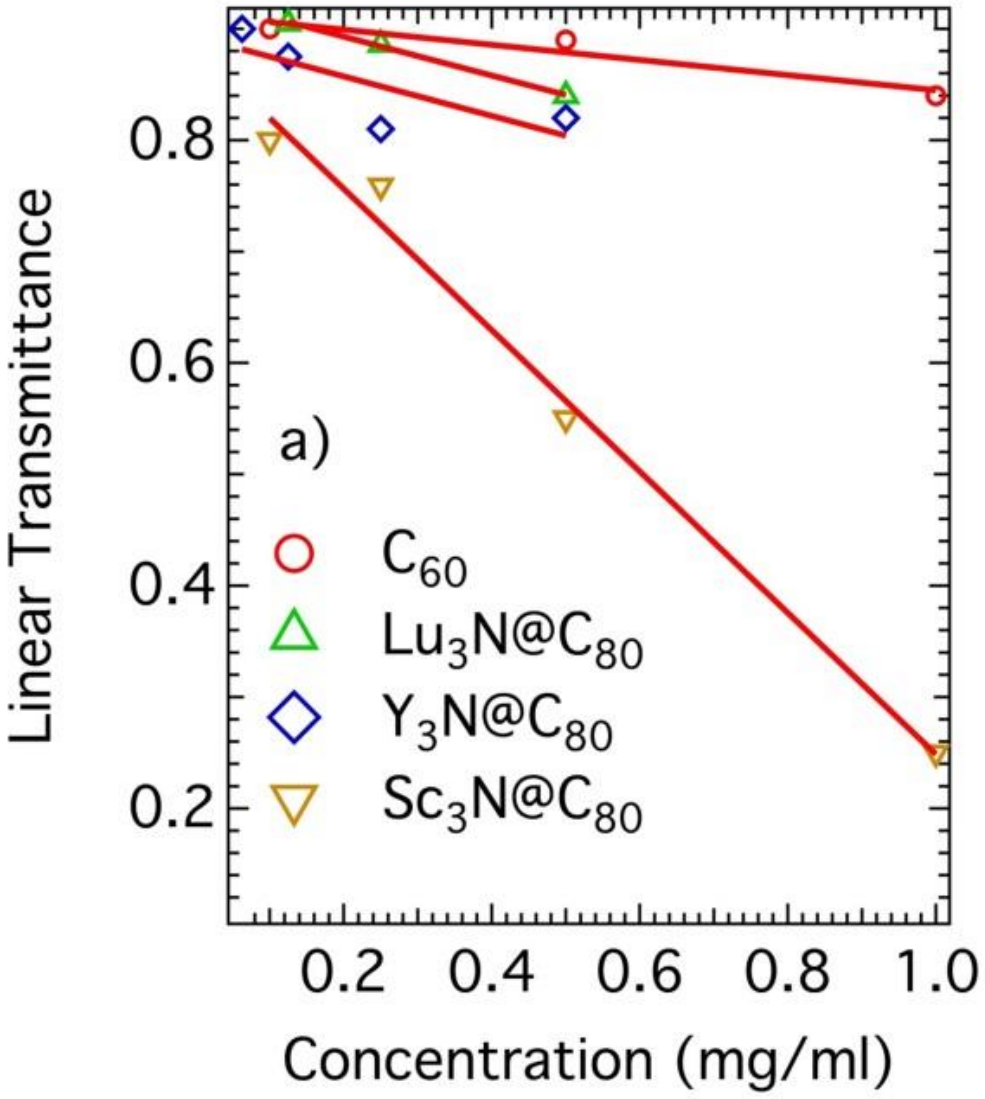

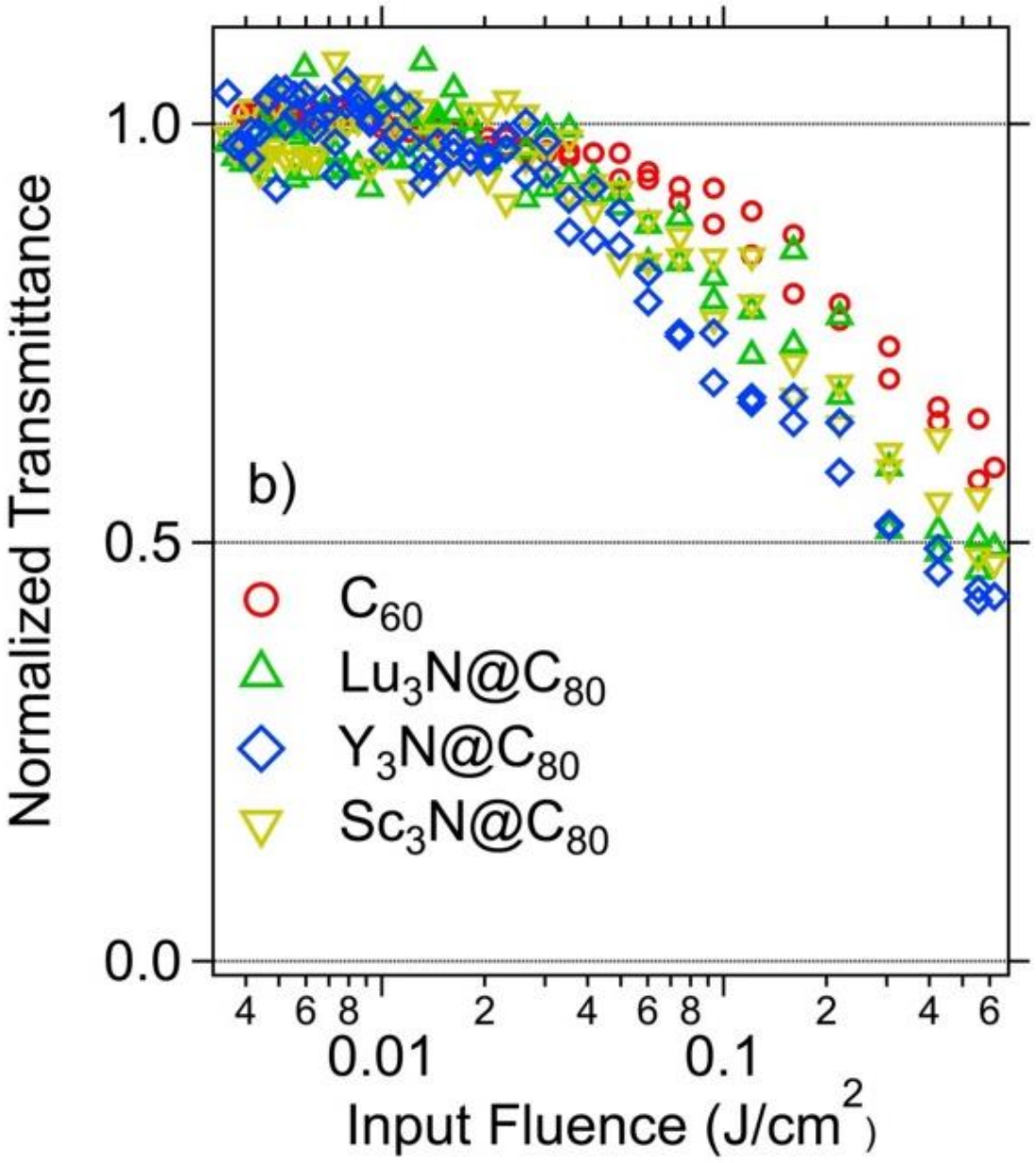

Fig. 2.4. (a) Linear Transmittance (measured with 1064nm, 7 ns laser) vs Concentration. Linear Transmittance of $Sc_3N@C_{80}$ appears to drop faster than C_{60}, $Lu_3N@C_{80}$ and $Y_3N@C_{80}$. (b) Non-linear optical response curve (same linear transmittance, 75%)

2.4 Conclusion

In summary, the lower HOMO-LUMO gap and intermolecular interactions in TNEFs allows strong non-linear absorption of 1064 nm wavelength in the ns regimen. Furthermore, the presence of the previously described charge transfer between the fullerene cage and trimetallic nitride is expected to increase the non-linear absorption at rates fast enough to provide a realistic optical switch response in TNEFs. Our results show that the TNEFs are excellent optical limiters with a low limiting threshold ~0.3 J/cm^2 at 1064 nm, high damage threshold >0.3 mJ, and can function as a realistic passive optical switches with a fast increase in absorption with increasing intensity.

CHAPTER THREE

NONLINEAR OPTICAL PROPERTIES OF BORON NITRIDE

Yongchang Dong, *et al*. "Conversion of intrinsic 5PA behavior in BN nanoplatelets to 2PA through photo-induced defects". Reproduced in part from a submitted manuscript.

3.1 Multiphoton absorption in nanomaterials

Two–dimensional (2D) materials exhibit unique optical properties that are different from their bulk. A testament to this fact is the recent rise of 2D materials in solar cells, light-emitting devices, photodetectors, and ultrafast lasers[79]–[82]. An interesting feature of light-matter interactions in many 2D materials[83]–[85] (*e.g.*, graphene, transition metal dichalcogenides, and phosphorene) is their increased transparency at higher light input fluences or the so-called nonlinear saturable absorption (SA)[37], [86]–[88]. The SA phenomenon is a direct consequence of dynamical interactions between electrons in 2D materials with the incident laser pulses, which allow for resonant or near-resonant excitation through single-photon absorption[37], [86]–[88]. In many 2D materials, the excited state absorption cross-section was experimentally found to be lower than that of the ground state absorption[86], [89]–[92]. Consequently, the absorption saturates at an input fluence that is sufficiently high for bleaching the ground state electrons. While this phenomenon is well-known in bulk materials (*e.g.*, Cr:YAG), the threshold SA fluence of 2D materials is significantly higher: a critical requirement for ultrafast laser pulse shaping. Many 2D materials (*e.g.*, graphene and MoS_2) are now being used as SA in mode locking and pulse-shaping in ultrafast lasers[84], [91], [93], [94]. Interestingly, other intriguing

nonlinear optical effects such as multi-photon or reverse saturable absorption, often exhibited by other nanomaterials (*e.g.*, C_{60}[37], [88], metal-oxide nanoparticles[95]–[97]) are rarely observed in the nonlinear optical (NLO) properties of 2D materials.

The recent realization of single/few-layer h-BN, which is an isostructural cousin to graphene with a wide band gap of ~5.5-6 eV[98], has opened new vistas for studying multiphoton absorption (MPA) in 2D materials. Previously, Kumbhakar *et al.*[99] reported a strong two photon absorption (2PA) in few-layer h-BN sheets when exposed to nanosecond pulses of a Nd:YAG at 1064 nm (corresponding to a single-photon energy of ~1.16 eV). This effect was attributed to the large transition dipole moment resulting from the electronegativity difference between B and N atoms. Furthermore, they reported an anomalously large value for 2PA cross-section at 1064 nm: ~52 times larger than the well-known efficient squaraine-bridged porphyrin dimer[100]. From a theoretical standpoint, h-BN should exhibit five-photon absorption (or 5PA) when excited with 1064 nm excitation via the simultaneous absorption of five photons corresponding to an energy ~5.80 eV. Given that the band gap of h-BN is ~5.5-6 eV, the conclusions drawn by Kumbhakar *et al.*[99] are peculiar because the energy of two photons from a 1064 nm Nd:YAG laser (two-photon energy ~2.32 eV) is insufficient to excite electrons across the band gap. Thus, a fundamental understanding of the nonlinear light-matter interactions in h-BN is still lacking.

Materials exhibiting a 5PA process (either at the bulk or nanoscale) have rarely been investigated in the literature due to the extremely low transition probability associated with a 5PA process[101]–[103]. Often, the necessary fluence for eliciting 5PA using

nanosecond pulses is well beyond the output of conventional lasers. In this study, we show that pristine h-BN nanoplatelets (BNNPs) inherently exhibit a high transition probability for 5PA when excited with 7 ns pulses of 1064 nm. Thus, BNNPs provide a unique platform for studying exquisite higher-order nonlinearties such as 5PA at low laser fluences (~0.2 J/cm^2) accessible through a ns pulsed Nd:YAG laser. Moreover, it is well known that MPA at higher fluence can either initiate photo-polymerization at the microscopic scale[104] or induce defects in the material under study via multiphoton ionization[105]. In case of BNNPs, we observed that a suspension of BNNPs in isopropyl alcohol (IPA) photo-transforms into doped BNNPs with altered configurations of N atoms when excited by a 1064 nm laser at high fluence. While BNNPs inherently exhibited 5PA at low laser fluence (< 0.6 J/cm^2), they instantaneous photo-transformation at high laser fluence and lead to 2PA. We used finite-element methods (COMSOL Multiphysics) to uncover that the high laser fluence raises the temperature of BNNPs to ~960 °C, which consequently promotes doping at the edge sites of BNNPs. In a separate experiment, we prepared O/C doped BNNPs via an alternate route, such as the high-energy ball-milling process, to confirm the influence of laser-induced transformation of the NLO properties in BNNPs, viz., the switching from 5PA to 2PA. Moreover, a clear evidence for the laser-induced doping which promotes the formation of B-O and C-N bonds was elicited through X-ray photoelectron spectroscopy of photo-transformed BNNPs. Lastly, the O/C induced electronic states obtained from our density-functional theory (DFT) calculations, provide a rationale explanation for the experimentally observed switching in the NLO properties of BNNPs at high laser fluences.

3.2 Characterization of boron nitride

Dispersion of BNNPs: The BNNPs (~1 mg/ml) were dispersed in IPA using a aqueous bath sonicator (Branson Aquasonic) for 5 minutes. Such dispersions were found to be stable for more than an hour, which enabled collection of reliable Z-scans for evaluating the NLO properties of BNNPs.

Sample preparation of ball milled BNNPs: Hexagonal boron nitride powder (1 μm, 98%) was purchased from Sigma Aldrich. For preparing doped BNNPs, BNNPs were ball milled with graphite (9:1 weight ratio) by a high-energy ball mill machine (MSK-SFM-3, MTI Corp.) for 2 hours.

Characterization: Raman spectroscopy was performed using a Renishaw in Via Raman Microscope equipped with a diode pumped laser source of 532 nm (CrystalLaser, Inc). High resolution X-ray diffraction (HR-XRD) was performed using a RIGAKU Ultima IV diffractometer, Cu K radiation, k ¼ 1.5406 A˚ on powder samples that were held in a standard Al sample holder. Quantitative analysis using Rietveld refinement was performed on the XRD peaks using PDXL software. TEM images were obtained using a Hitachi H-9500. X-ray photoelectron spectroscopy (XPS) studies were performed using a Kratos Axis Ultra DLD instrument, and the spectra were calibrated by the C1s line present at 284.6 eV.

Z-scan technique: For our Z-scan setup (see Fig. 3.1), a linearly polarized 7 ns optical pulsed beam from a Q-switched frequency-doubled Nd:YAG laser (a LabVIEW program synchronized the single-shot laser pulses with the moving stage and the resulting

repetition rate was ~1 Hz) at 1064nm, was focused by a converging lens (focal length of ~20 cm) to form an optical field of gradually changing laser intensity. The BNNP dispersions were found to have ~80% linear transmittance (0.8 mg/ml) at 1064 nm. The BNNPs/IPA dispersions were held in the 1 mm thick quartz cuvettes (100-QS Hellma® Analytics) and translated across the focal plane in the beam direction (*z*-direction). With the sample dispersions experiencing different optical intensities at each *z* position, the corresponding transmittance was recorded by a calibrated photodetector (RjP-7620, Laserprobe, Inc) placed on the sample translation axis (see Fig. 3.1). A photodetector was placed off-axis for obtaining nonlinear scattering data. A detailed description of the Z-scan technique can be found elsewhere[33], [37], [88], [106]–[110].

In our experiments, the open aperture Z-scan MPA coefficients were calculated from spectra under the assumption that only one type of MPA dominates at any given time. The optical intensity *I* can be described as[98]

$$\frac{dI}{dz'} = -\alpha_N I^{N-1}, \tag{3.1}$$

where z' is propagation distance of light within the sample and α_N is the N-photon absorption coefficient. For example, α_2 represents the 2PA coefficient while α_5 denotes 5PA.

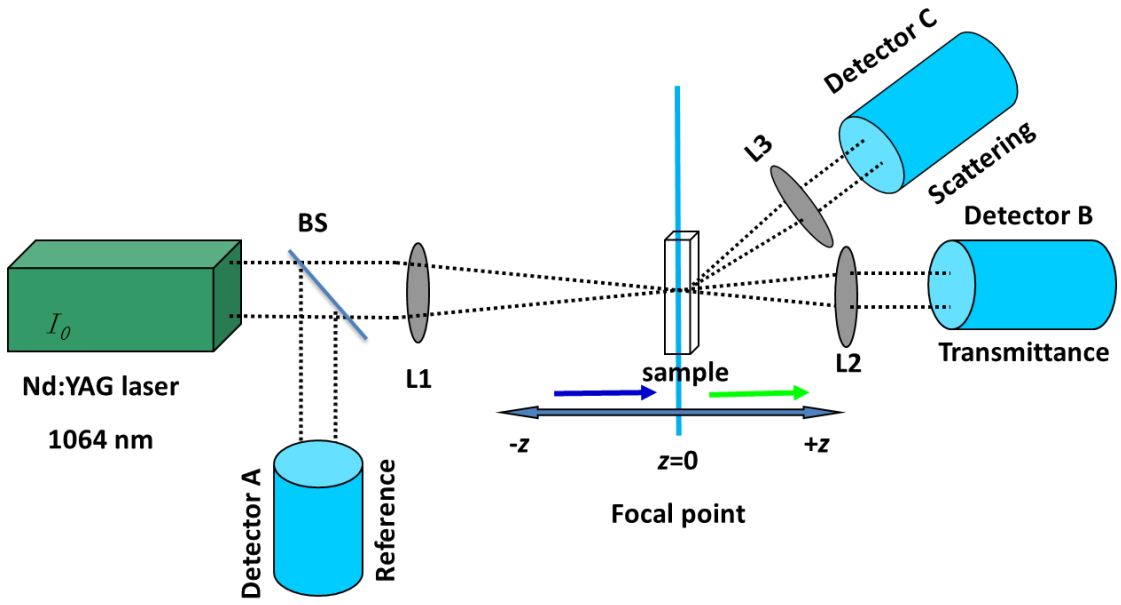

Figure. 3.1. As shown in the schematic of the experimental Z-scan setup, a sample is moved through the focal region (z = 0 mm being the focal point) of the incident laser beam focused by a converging lens. A reference photodetector (Detector A) is used for monitoring the fluctuations in the incident intensity. The changes in nonlinear transmission are recorded by an on-axis detector B while an off-axis detector C is used for measuring the nonlinear scattering.

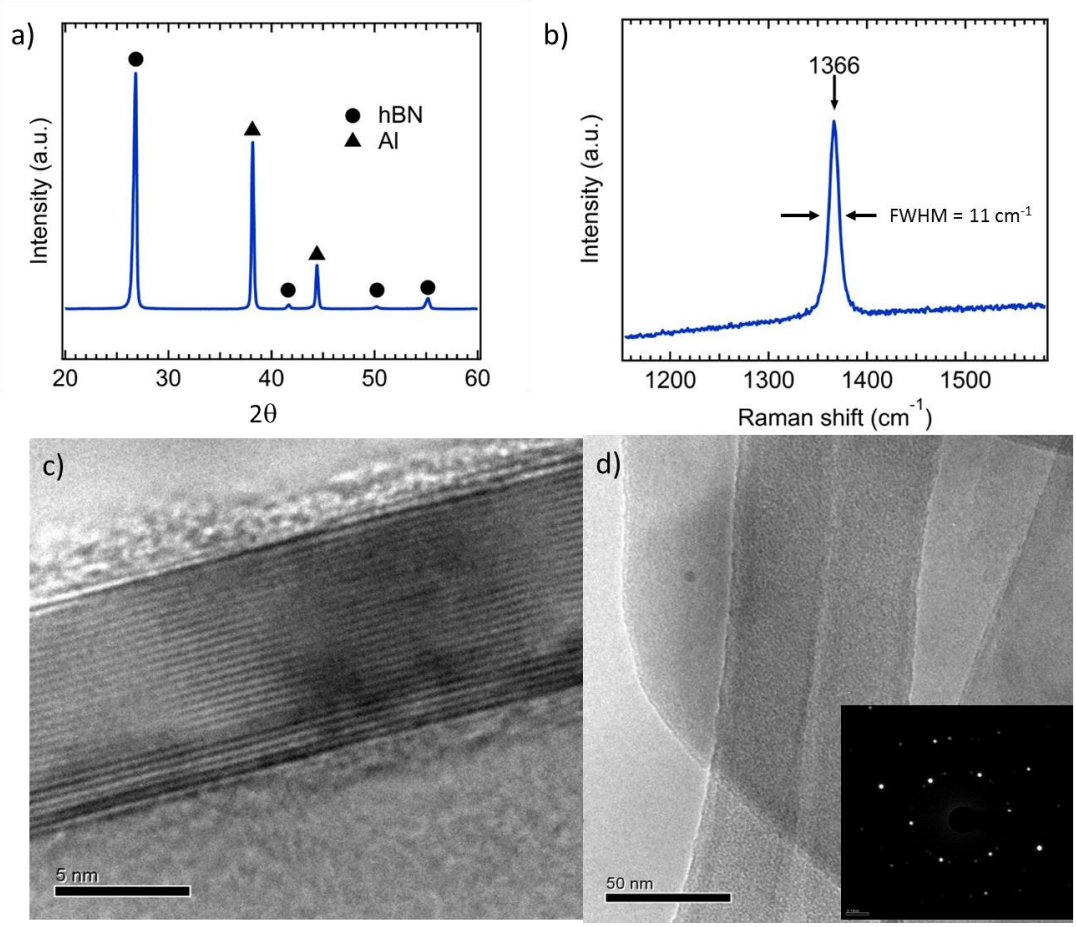

Figure. 3.2. a) XRD pattern of BNNPs held on an Al sample holder. b) Raman spectrum of pristine BNNPs using the 532 nm laser excitation. HRTEM images of BNNPs c) side view and d) top view. The inset of d) is the selected area electron diffraction of the BNNP.

3.3 Multiphoton absorption process in boron nitride

BNNPs (Sigma Aldrich) were characterized by X-ray diffraction (XRD), Raman spectroscopy, high-resolution transmission electron microscopy (HRTEM) and X-ray photoelectron spectroscopy (XPS). The four XRD peaks at ~26°, ~42°, ~50° and ~55° (Fig. 3.2) are due to diffraction from the (002), (100), (102) and (004) planes, and the

additional diffraction peaks at ~38° and ~44° stem from the Al sample holder. A lattice constant of 3.29 Å was deduced from the pattern in Fig. 3.2a for BNNPs, and its Raman spectrum (Fig. 3.2b) showed the characteristic E_{2g} band at 1366 cm^{-1} (FWHM = 11 cm^{-1}). The dynamic light scattering (DLS) measurements (Nanosizer S90, Malvern Instruments) revealed a lateral size of BNNPs as 745 ± 92 nm. HRTEM images of the BNNPs are shown in the Figs. 3.2c and d. We found that BNNPs were an average of ~20-25 layers in thickness which exhibited a hexagonal electron diffraction pattern indicating high crystallinity.

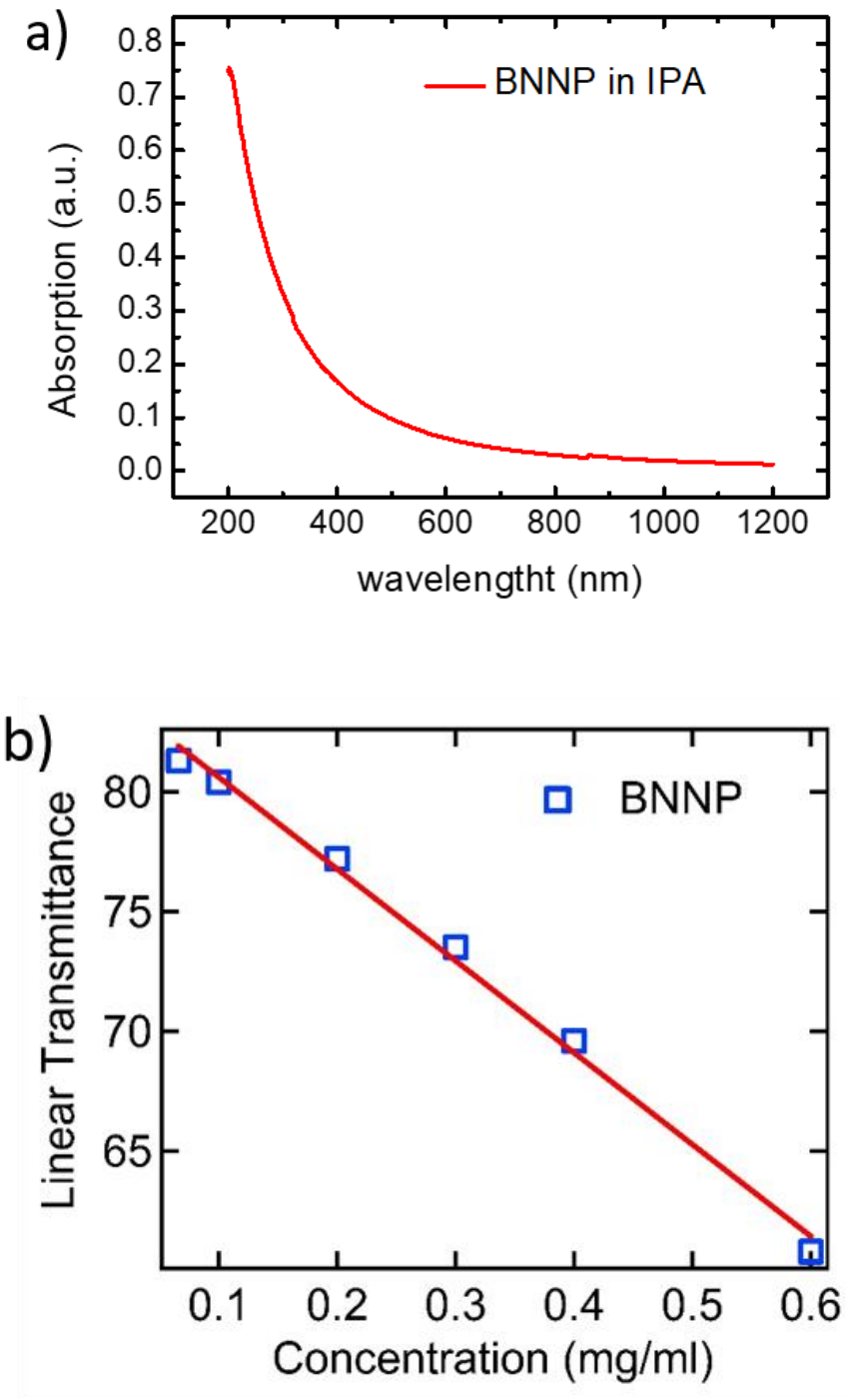

Figure 3.3. a) UV-Vis spectrum of BNNP dispersion in IPA. b) The linear transmittance of BNNP in IPA in different concentration measured at1064 nm.

We used the open aperture Z-scan method (see experimental section and Fig. 3.1 for a detailed description) for investigating the NLO properties of BNNPs (suspended in IPA) under varying 1064 nm (1.16 eV) laser fluences. The UV-Vis spectrum of BNNP is shown in Fig. 3.3. Fig. 3.4a shows a typical normalized transmission (T/T_0, where T and T_0 are the nonlinear and linear transmittance values) curve for BNNPs when excited with a laser energy of ~220 μJ (corresponding to a fluence of ~0.4 J/cm^2 at the focal point), which could be best fit to a 5PA process (solid trace in Fig. 3.4a). See Fig. 3.5 for the fitting accuracy. This observation suggests that the electrons at the valence band maximum in BNNPs (band gap of 5.5-6 eV[111]) can be excited to the conduction band through 5PA at input energies ~220 μJ. It should be mentioned that the possibility of nonlinear light scattering (NLS) leading to the response in Fig. 3.4a was ruled out by measuring the off-axis scattered light intensities (see Supplementary Information Fig. 3.6). Interestingly, when the laser fluence was increased to ~350 μJ (corresponding to a fluence of ~0.6 J/cm^2 at the focal point), an abrupt change in the lineshape of BNNPs' normalized transmittance past the focal point (Z= 0 mm) became evident (Fig. 3.4b). The pre-focus Z-scan data for 350 μJ in Fig. 3.4b, obtained as the sample approached the focal point (see blue arrow in Fig. 3.1), was best fitted to 5PA. However, the past-focus data (receding from the focal point, green arrow in Fig. 3.1) showed the presence of two-photon absorption or 2PA.

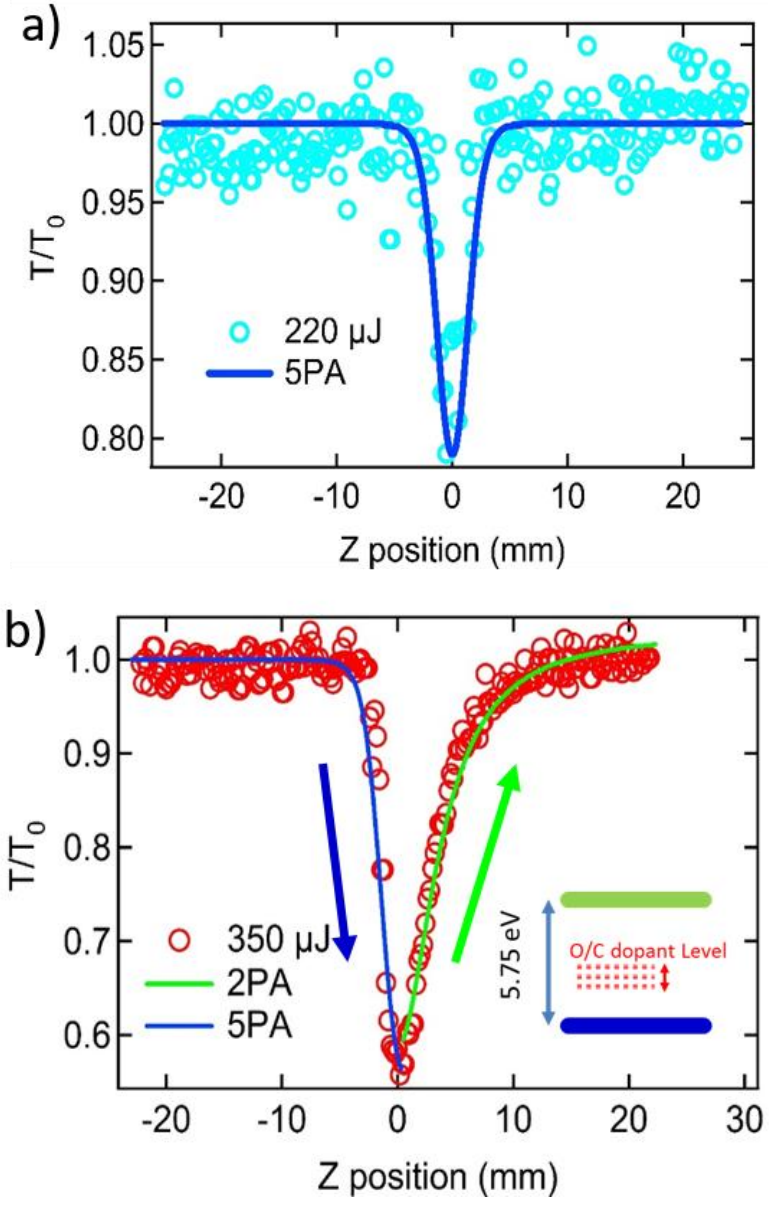

Figure 3.4. a) A dispersion of pristine BNNPs in IPA exhibits a 5PA response in a Z-scan curve collected with a laser fluence of 220 μJ. b) Upon increasing the laser fluence to 350 μJ, a 5PA response is observed, signaling an onset of photo-induced doping of BNNPs with carbon from the IPA. The coefficients for 2PA and 5PA found from the numerical fits

were 12 cm GW^{-1} and 2500 cm^7 GW^{-4}, respectively. A schematic inset showing the O/C dopant levels introduced into the wide band gap of h-BN. The presence of such levels at ~2-2.5 eV enable 2PA in the photo-transformed BNNPs.

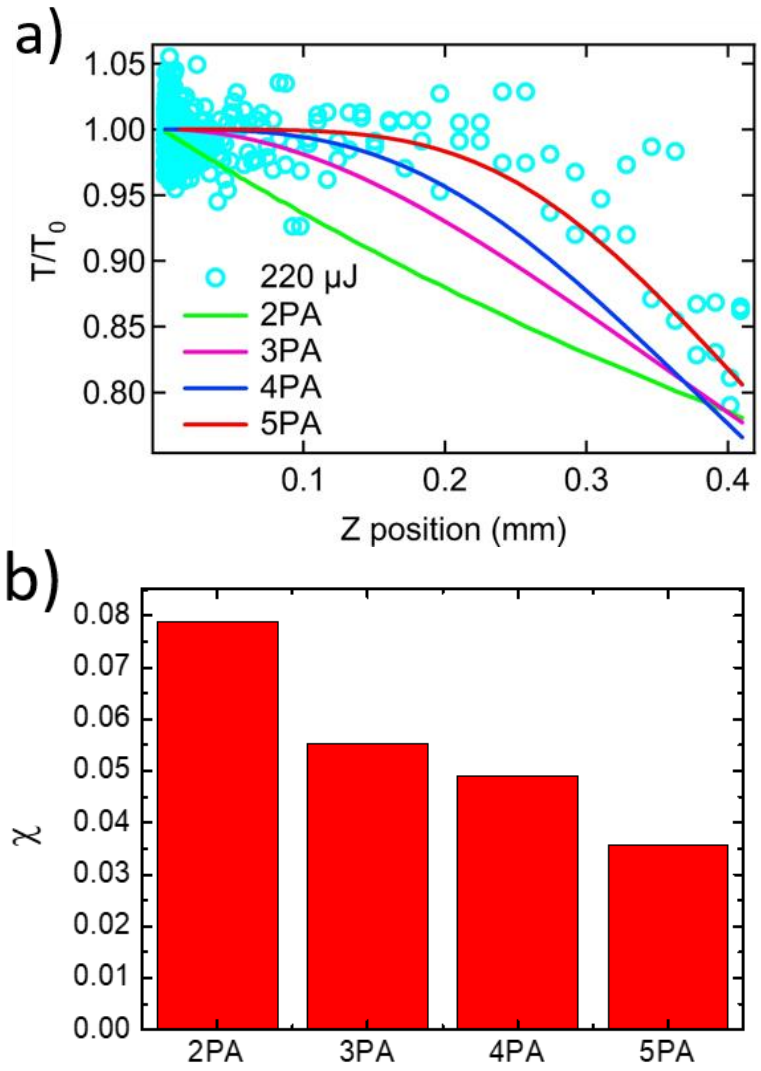

Figure 3.5. a) The 2PA, 3PA, 4PA and 5PA fitting of BNNP at 220 μJ experimental data. b) The reduced chi square value for each fitting in a), and suggests that the 5PA gives the best fit to the data.

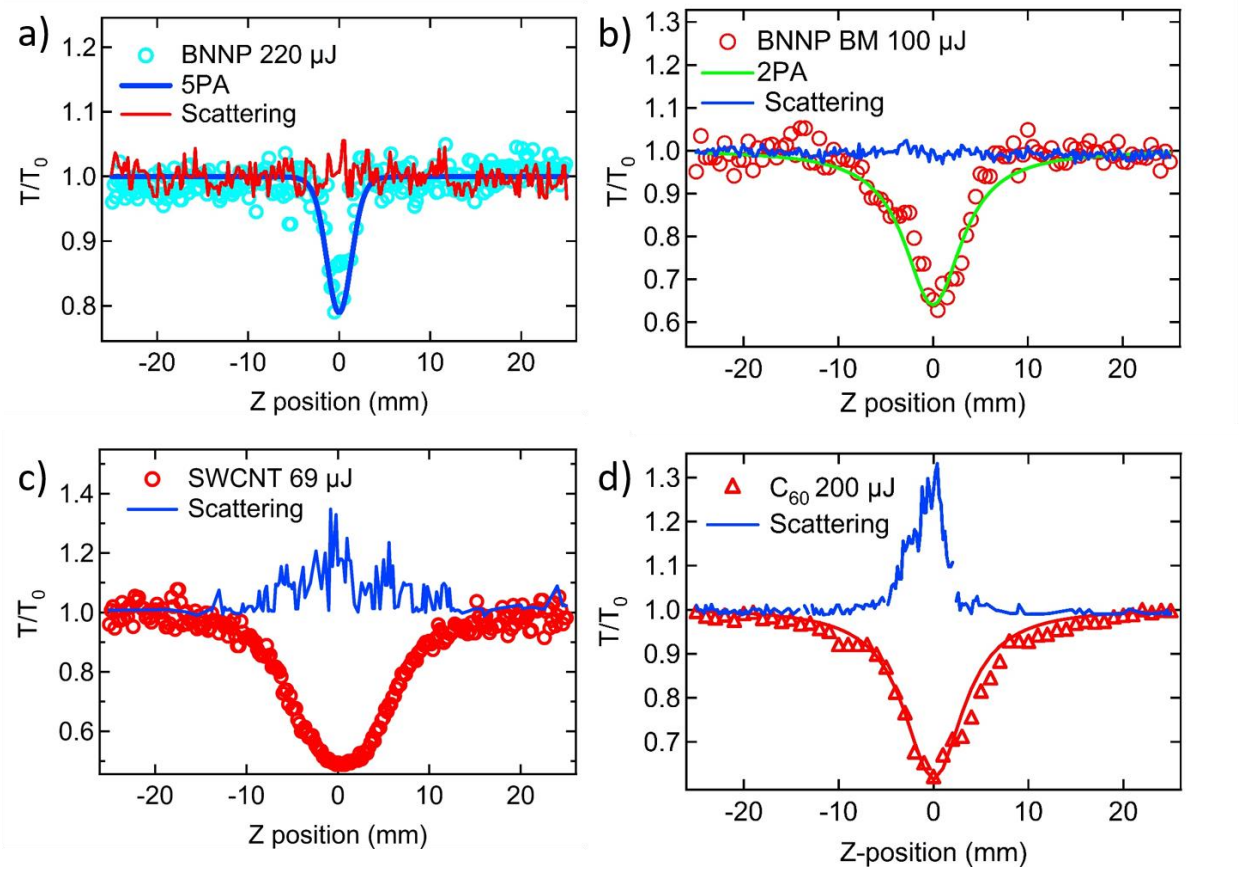

Figure 3.6. The Z scan transmission and scattering curves for a suspension a) BNNPs at 220 μJ & b) ball-milled BNNPs (BNNP BM) at 100 μJ. No scattering was observed in these cases. Our instrument was calibrated and tested using other nanomaterials, such as c) single-walled nanotubes (SWCNTs) and d) C_{60}, which are well-known for their nonlinear transmission properties[112]–[114].

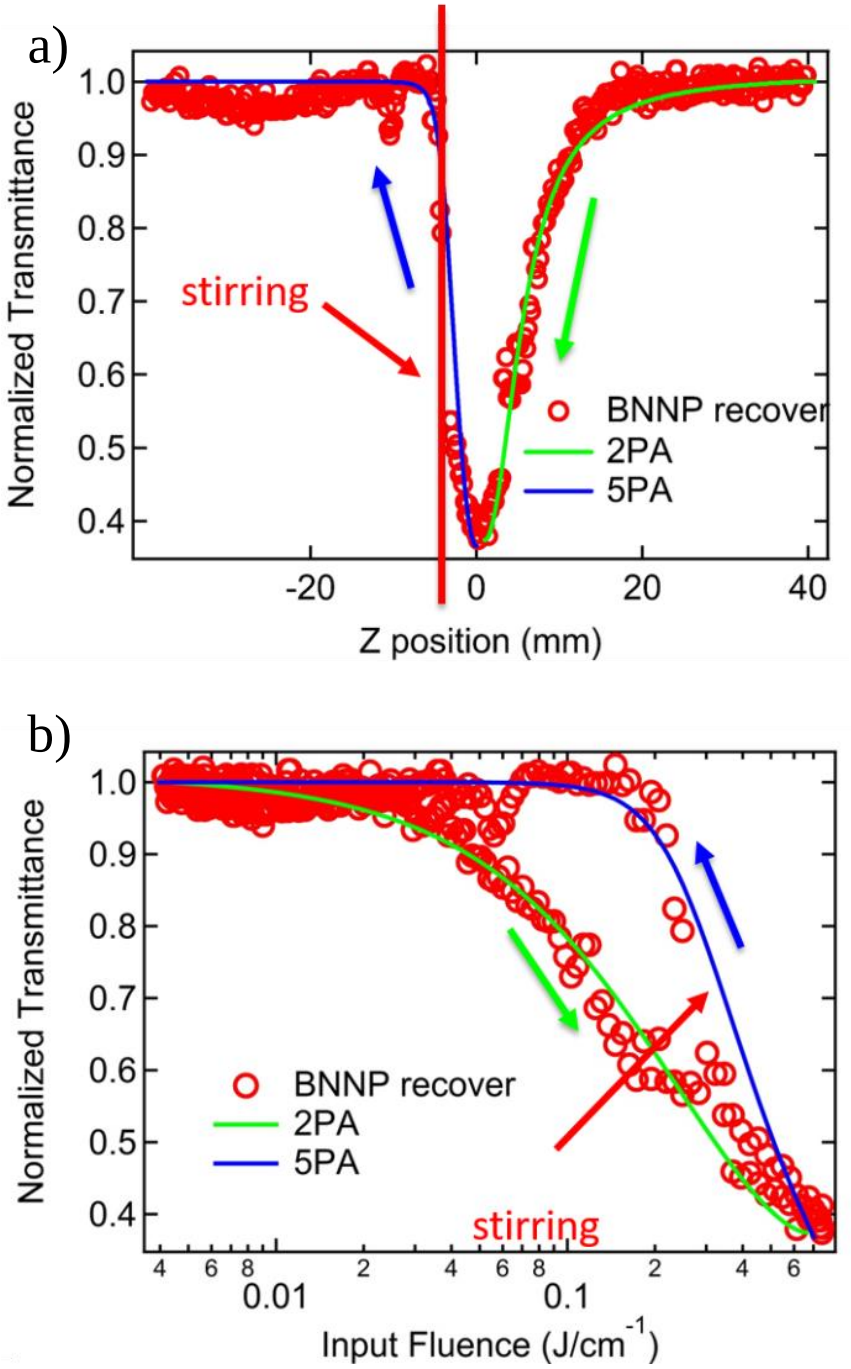

Figure 3.7. As discussed in Fig. 3.4b, BNNPs suspension exhibited 5PA as it was translated from z=-30 to 0 mm while an abrupt change to 2PA was observed upon passing the focal point (from z=0 to +30 mm) at an input fluence ~350 μJ. The BNNPs in the beam path

were photo-transformed through O/C doping at the focal point (z=0 mm). The same suspension was scanned in the reverse direction (z=+30 to 0 mm) and a 2PA was observed until the focal point. a) After the sample passed just beyond the focal point (z=-5 mm), the suspension was gently stirred (see red arrow) displacing the photo-transformed BNNPs away from the beam path. Subsequent Z-scan (z=-5 to -30 mm) showed that the intrinsic 5PA was recovered (data indicated by the red circles labeled as BNNP recover) confirming the effects of laser-induced doping. Panel b) shows the plot of normalized transmission as a function of input fluence, which was calculated from Fig. 3.5a using equation (1) described in the text.

In reality, BNNPs support 5PA as long as the input fluence is below the threshold value 0.6 $\pm$ 0.012 J/cm^2 - an inherent property of BNNPs which was overlooked in the study reported by Kumbhakar *et al*. Given that the laser beam radius at the focal point was ~100 μm, only a small amount of BNNPs within the beam path is expected be photo-transformed. To confirm this, we repeated the Z-scan on the same BNNPs dispersion after gently stirring it. As expected, the inherent 5PA response of BNNPs was recovered (Fig. 3.7) implying that photo-transformed BNNPs were no longer present in the beam path. Furthermore, we also ruled out NLS effects arising from micro-bubbles at high laser fluence by using an off-axis detector (see Fig.s 3.1 and 3.3). Based on the data presented in Fig. 3.4, we conclude that the much higher laser fluence used in the previous study by Kumbhakar *et al*[99] (3.9 J/cm^2, 1064 nm) precluded the authors from uncovering the inherent 5PA in h-BN.

3.4 Influence of dopants on NLO properties of boron nitride

We hypothesize that the high laser fluence promotes heteroatomic doping of oxygen/carbon (from IPA) into BNNPs, possibly at the edge sites due to its low formation energy[115], [116]. The presence of O/C dopants in BN lattice is known to introduce new electronic states within the band gap[117]–[121], which could explain the observation of 2PA at high laser flunces[122]. Indeed, recent spectroscopic studies (cathodo- and photo-luminescence, UV absorption, and scanning tunneling spectroscopy) on defected/doped h-BN crystals and nanostructures found clear spectral features at lower energies (~2-4 eV) in addition to the band gap ~5.75 eV due to the presence of dopant-induced electronic states[121], [123]. Similarly, our theoretical studies using density functional theory (see Fig. 3.8) along with earlier investigations employing local density approximation and GW approximation confirmed the presence mid-gap states for C/O dopants at ~1-4 eV. Based on our Z-scan results and existing spectroscopic studies[42], [58], [85], [88], we posit that the ground state electrons in doped BNNPs when excited with 1064 nm (or ~1.16 eV) photons are promoted to the C/O-dopant induced states present ~2-2.5 eV through a 2PA process (inset panel in Fig. 3.4b).

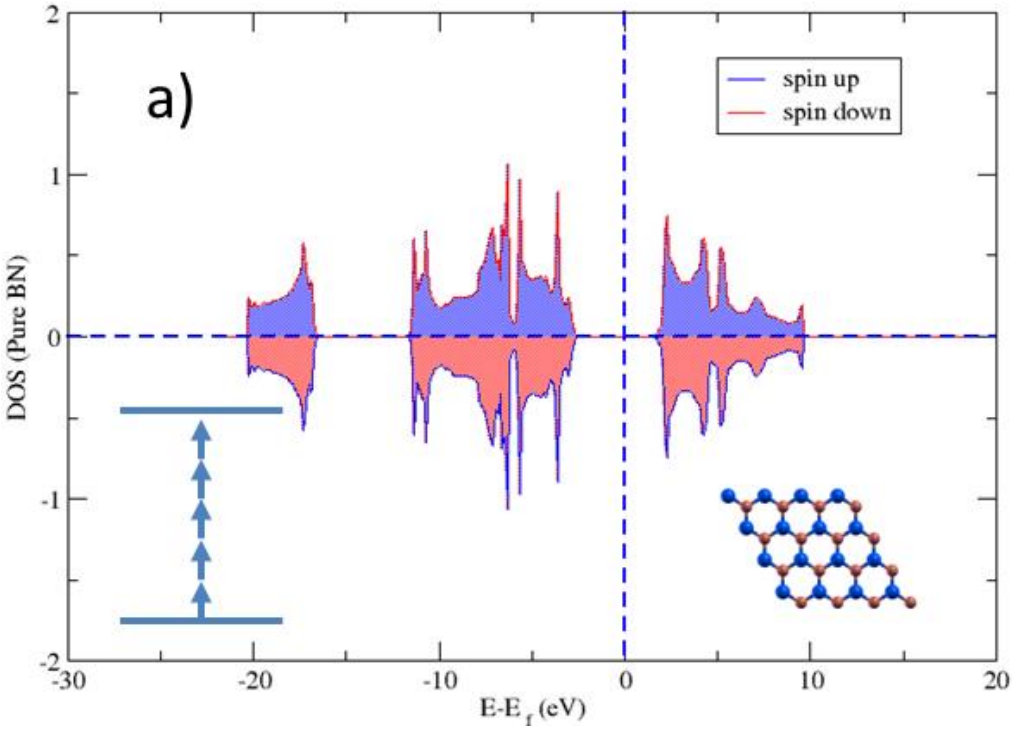
a)
spin up
spin down
DOS (Pure BN)
E-E f (eV)
2
1
0
-1
-2
-30
-20
-10
0
10
20

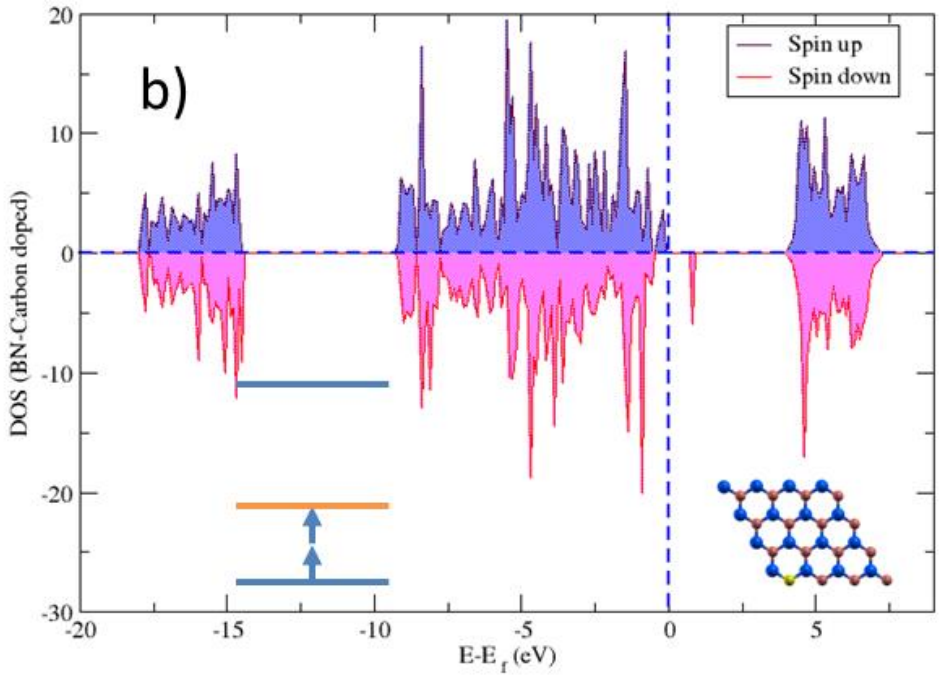
b)
Spin up
Spin down
DOS (BN-Carbon doped)
E-E f (eV)
20
10
0
-10
-20
-30
-20
-15
-10
-5
0
5

Figure 3.8. Building on previous research[124], we too conducted the first-principles calculations using Density Functional Theory (DFT), which included the van der Waals interaction in DFT-D2 approach under Generalized Gradient Approximation (GGA), to examine the electrical properties of pristine and carbon-doped h-BN. The density of states for the carbon doped h-BN showed the presence of new mid-gap states, which are responsible for the change in the non-linear optical properties from 5PA to 2PA. These mid-gap states have also been observed earlier from other DFT studies. Given that the energy cost for doping C into BN lattice is very high, O/C atoms are expected to bind at the edges of BN. The density of states of a) pure BNNP and b) carbon doped BNNP. The inset figures in a) and b) show the lattice of BNNP wherein the blue and purple colored atoms represent the boron and nitride atoms, respectively. The yellow colored atom in the BNNP (Panel b) represents an impurity atom, *viz.*, a carbon atom. The inset schematics represent the 5PA and 2PA processes in pure and carbon-doped BNNPs, and orange colored energy level represents the mid-gap states induced by the carbon dopants.

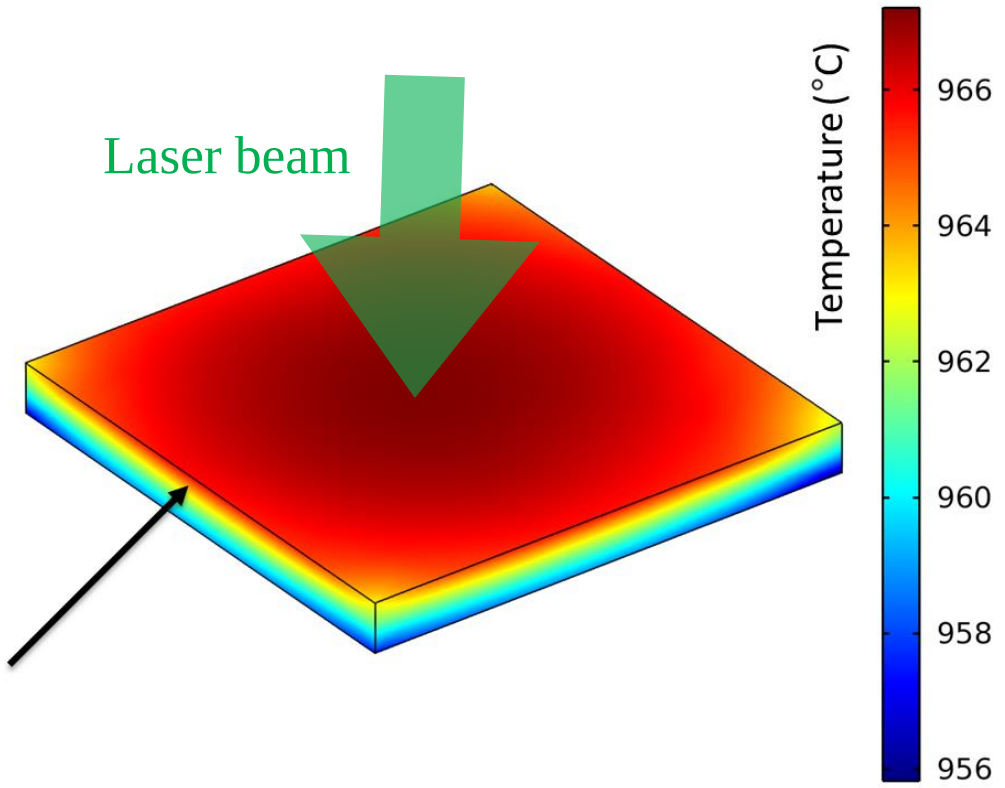

Figure 3.9. Finite element simulations of a BNNP (100 × 100 × 10 nm^3) in IPA liquid suspension after being exposed to a laser fluence of ~0.6 J/cm^2 for 7 ns.

We used finite-element method (COMSOL Multiphysics) with a heat transfer module to simulate the conditions at high laser fluence that could result in doping of O/C into BNNPs. The BNNPs were modeled as platelets with average dimensions 100 × 100 × 10 nm^3 (as gleaned from TEM images such as the one presented in Fig. 3.2c) and the laser fluence was matched to threshold values for eliciting a 2PA response, *i.e.*, ~7 ns pulse with energy density of ~0.6 J/cm^2 (*cf.* Fig. 3.4b). The temperature distribution of the BNNP

platelets after exposure to a single laser pulse is shown in Fig. 3.9. Our COMSOL simulation revealed that the laser rapidly (~7 ns) heats the surface of the BNNP and increases its temperature to 950-966 °C. The top surface edges of the BNNP were raised to a higher temperature relative those on the bottom layer because the heat diffusion rate is much faster in the lateral (6 W cm^{-1} $°C^{-1}$) than in the vertical (0.3 W cm^{-1} $°C^{-1}$) direction for h-BN[125]. The laser-induced increase in the temperature at the edges of BNNP platelets is much higher than the decomposition temperature of IPA (~400 °C), which possibly leads to IPA carbonization and a subsequent doping of BNNPs with carbon at its edge sites.

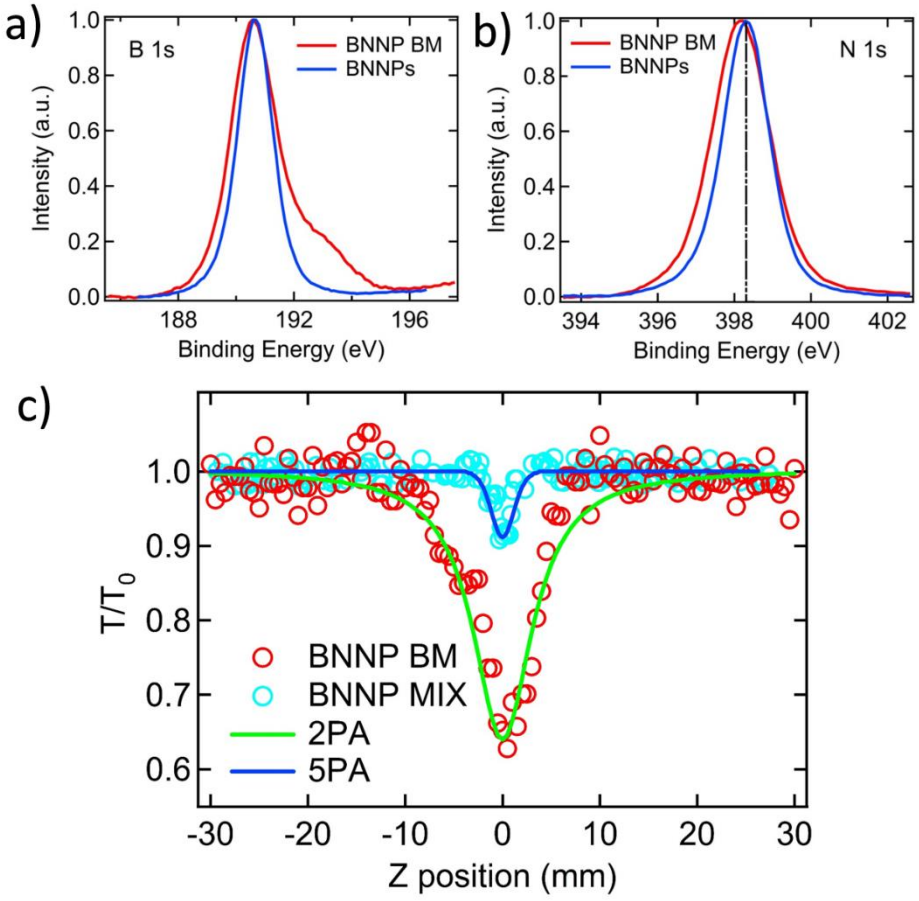

Figure 3.10. a) and b) show the XPS spectra of pristine and ball milled BNNPs. A new peak is observed ~193 eV in the B 1s spectrum, which is indicative of B-O bonds or the incorporation O atoms into BN lattice. The N 1s spectrum was found to broaden and downshift by ~0.2 eV possibly due to C doping. c) Z-scan curves for BNNP BM dispersion in IPA, which exhibits a 2PA response (red circles). The mixture of BNNPs and graphite powder, prior to ball milling, exhibited a 5PA response as expected (blue circles).

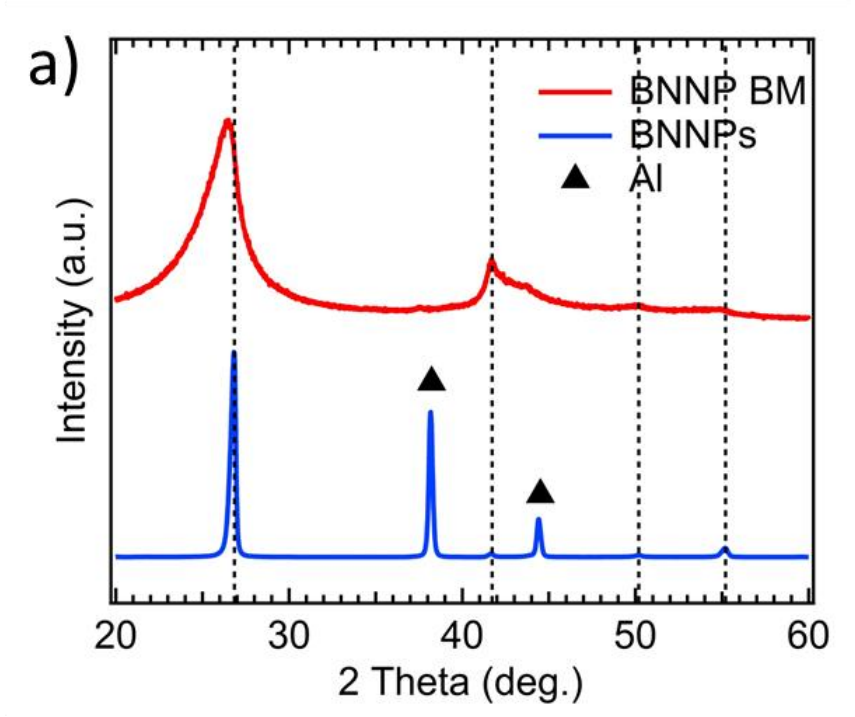
a)
BNNP BM
BNNPs
Al
Intensity (a.u.)
20
30
40
50
60
2 Theta (deg.)

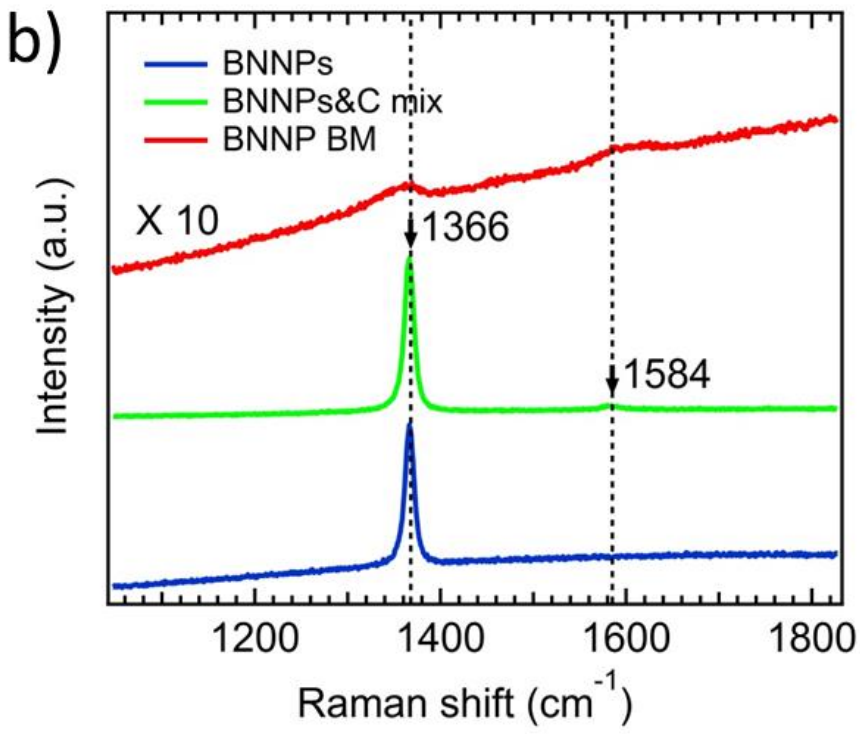
b)
BNNPs
BNNPs&C mix
BNNP BM
X 10
1366
1584
Intensity (a.u.)
1200
1400
1600
1800
Raman shift (cm-1)

Figure 3.11. a) Ball milling of BNNPs with graphite for 2 hours was found to broaden the featured peaks in addition to slightly shifting to a lower angle, when compared to corresponding features of pristine BNNPs. This indicates that the doping of carbon in the h-BN lattice creates stress in the lattice as well as decreases of the particles size. b) The Raman spectra of BNNPs and graphite powder mixture before and after ball milling. After ball milling, the 1366 cm^{-1} band in BN was suppressed suggesting a change in the crystal structure. As described in Figs. 3.10a and b, our XPS data showed clear evidence for O/C dopants that may have altered the crystal symmetry.

While conventional XPS is an excellent tool for confirming the presence of dopants in BNNPs, it is plagued by the presence of O/C peak of the IPA solvent used in this study. Moreover, only a small amount of BNNPs that are present within the beam path are photo-transformed. Thus, to confirm our hypothesis that BNNPs switch their NLO properties from 5PA to 2PA due to laser-induced doping of it edges with O/C, we intentionally doped BNNPs with O/C by ball milling a mixture of BNNPs and graphite powder. To this end, we mixed BNNPs and graphite in 9:1 weight ratio, which we refer to as "BNNP MIX". The Z-scan curves for BNNP MIX sample (discussed later in Fig. 3.10c), prior to ball milling, showed a clear 5PA signal intrinsic to BNNPs at a low laser fluence 100 μJ (~0.2 J/cm^2 at the focus). Next, the BNNP MIX sample was ball milled for 2 hours for doping O/C into the BN lattice. An extensive characterization toolset including XRD, Raman spectroscopy (Fig. 3.11) and XPS (Fig. 3.10) confirmed doping of both O and C atoms (~1-2 at. % as evinced from XPS in Figs. 3.10a and b) in ball milled BNNPs[118], [120], [126], which we henceforth refer to as BNNP BM sample. As shown in Figs. 3.10a and b, the B 1s and N 1s spectra from pristine and doped BNNPs show primary binding energies of 190.7 and 398.3 eV, respectively. We observed an extra peak ~192.8 eV in the B 1s spectrum (Fig. 3.10a), which is known to arise from B–O bonds, confirming O-doping in BNNP BM samples. Furthermore, we also found that the N 1s spectrum was slightly downshifted from ~398.3 to 398.1 eV, which was previously attributed to C-doping. [118], [126] As shown in Fig. 3.10c, we observed a 2PA response in the Z-scan curve for BNNP BM sample in IPA even at a low laser energy of 100 μJ (~0.2 J/cm^2 at the focus) while

BNNP MIX samples (prior to ball milling) exhibited the intrinsic 5PA response. The values of 2PA coefficients for BNNP BM and photo-transformed BNNPs in IPA were found to be very similar (Table 3.1). This implies that the mid-gap states supporting a 2PA response in BNNP BM and photo-transformed BNNPs are similar *viz.*, O/C dopant-induced electronic states present ~2-2.5 eV within the band gap of BN (*cf*. inset of Fig. 3.4b).

Table 3.1. The values of 2PA and 5PA coefficients for all the samples in this study.

sample	Laser Intensity	2PA	5PA
BNNPs	350 μJ	12 cm GW^{-1}	2500 cm^7 GW^{-4}
BNNPs BM	100 μJ	8 cm GW^{-1}	N/A

3.5 Conclusion

In summary, we report the discovery of a rarely observed nonlinear phenomenon, *i.e.*, five-photon absorption (5PA) in a 2D material, such as few-layer h-BN nanoplatelets (BNNPs). Importantly, through a systematic study we show that the nonlinear optical response of BNNPs dispersed in isopropyl alcohol (IPA) switches from a 5PA to a 2PA response when the laser fluence exceeds 0.6 J/cm^2 (at the focus or z=0) due to photoinduced O/C doping (from IPA) of BNNPs. Previous studies on the nonlinear optical properties of BNNPs (Kumbhakar *et al.* [99]) used very high laser fluence (~3.9 J/cm^2) and thus failed to uncover the inherent 5PA phenomenon in BNNPs. Our finite-element calculations using

COMSOL Multiphysics showed a rapid increase in the temperature of edge sites in BNNPs (> 960 ^{o}C) suitable for carbonizing IPA and doping of O/C atoms at edge sites in BNNPs. We associate the observation of a 2PA response at a high laser fluence in BNNPs with to the NLO properties of O/C doped BNNPs. This correlation was independently confirmed from Z-scan spectra of BNNPs doped with O/C atoms via ball milling with graphite. While XPS presented clear evidence of B-O and C-N bonds in the ball milled BNNPs, Z-scan spectra at low laser fluence showed a 2PA response, akin to the Z-scan spectra of photo-transformed BNNPs. Lastly, the 2PA coefficients in ball milled BNNPs and photo-transformed BNNPs were found to be similar, further confirming our hypothesis.

CHAPTER FOUR

NONLINEAR OPTICAL PROPERTIES OF MXENEs

Yongchang Dong, *et al*. "Saturable absorption in 2D Ti_3C_2 MXene thin films for passive photonic diodes". *Advanced Materials* (2018) 30, 1705714. Reproduced in part with permission of Wiley.

4.1 Saturable absorption in 2D materials

The unique light-matter interactions in two-dimensional (2D) materials are ideal for a wide range of applications in photonics, photovoltaics, and flexible electronics[127]–[129]. In the nonlinear regime, many 2D materials are known to exhibit increased transmittance with increasing light intensities through saturable absorption (SA)[130]–[142]. When the ground state absorption coefficient of a material is higher than that of its excited states, bleaching of the ground state electron population occurs at high light intensities and pump rates, leading to SA behavior. This could be understood in terms of a fluence-dependent absorption coefficient for a SA material (SAM) as $a(I) = \frac{a_0}{\left(1 + I/I_s\right)}$ (eqn 1.20), where α_0 is the linear absorption coefficient, I represents the incident fluence, and I_s is the saturation fluence. I_s is defined as the incident fluence at which the absorption coefficient is half of the linear absorption coefficient ($\alpha_0/2$). The maximum change in absorption of a SAM for a given wavelength determines the modulation depth (ΔT). SA behavior in materials can be beneficial for photonic applications such as passive mode locking, Q-switching of lasers

for the generation of short optical pulses, nonlinear filtering for pulse shaping, optical isolation, and optical signal processing[8], [127], [132], [135]. For example, a SAM placed in a laser cavity attenuates low-intensity leading and trailing parts of a pulse more effectively than the high-intensity pulse center due to increased transmittance (determined by the modulation depth) at higher light intensities. To produce lasers with short pulse-width (up to fs) and high repetition-rate (many pulses per second), a SAM that becomes easily and quickly saturated (i.e., low saturation fluence and fast recovery time) with a large modulation depth and a high damage threshold is imperative. Although semiconductor-based SAMs are widely available, they are plagued with many challenges such as low damage thresholds, slow recovery, and limited lifetime[143]–[146].

Alternatively, 2D materials such as graphene and transition metal dichalcogenides (e.g., MoS_2) that exhibit saturable absorption (SA) with an increased modulation depth up to ~ 20% and a fast recovery time of ~100 fs have been shown to outperform bulk SAMs for ultrafast pulse generation[84], [130]–[142], [147], [148]. Nonetheless, many challenges in 2D SAMs still exist, such as the need for a high modulation depth, low non-saturable loss, and high threshold for optical damage. Recently, Jhon *et al*. demonstrated that 2D titanium carbonitride MXene (Ti_3CNT_x) could be utilized as a material for femtosecond mode locking applications[149]. MXenes are 2D transition metal carbides and nitrides with the chemical formula $M_{n+1}X_nT_x$ (n = 1-3), where M is an early transition metal, X is carbon and/or nitrogen, and T_x represents surface termination groups such as =O, –OH, –F, etc.[150]–[152] Although Jhon *et al*. found that drop-casted Ti_3CNT_x films exhibited a relatively low modulation depth ~1.7%, the work shows the potential of MXenes in

photonic applications as SAMs[149]. In this regard, a fundamental understanding of the SA behavior in MXenes in dependence on thickness and film quality is necessary to engineer better SAMs for pulse shaping and mode locking applications.

In this Chapter, we experimentally show that $Ti_3C_2T_x$ MXene thin films, prepared using a new solution-processing technique, are excellent SAMs with high modulation depth of up to ~50% and high threshold ~70 mJ/cm^2 for optical damage. $Ti_3C_2T_x$ is the first MXene and the most studied which is synthesized by selective etching of Al from sputter-deposited epitaxial Ti_3AlC_2 MAX phase films. [153] The ability to intercalate and delaminate MXenes into a colloidal state has opened the door to fabricating MXene films *via* common solution processing techniques[154]. Recently, MXene films have been fabricated for various applications using spin/drop-casting[155], spray coating[156], and rolling[157]–[159]. However, the variability in the film uniformity and thickness prohibits a systematic study of SA behavior in MXenes. To overcome this challenge and produce very thin and uniform films, we implemented a simple and efficient interfacial film technique between two immiscible liquids (viz., water and toluene), previously used for other nanomaterials [160]–[163], to prepare thin $Ti_3C_2T_x$ MXene films (thickness *h* in the range of ~5 - 100 nm). Our nonlinear optical studies using the Z-scan method suggest that the SA behavior at 1064 nm in $Ti_3C_2T_x$ films arises from plasmon-induced increase in the ground state absorption. More importantly, the nonlinear optical absorption and the saturation fluence of $Ti_3C_2T_x$ films were found to vary with film thickness. This implies that nonlinear optical properties of $Ti_3C_2T_x$ films can be controllably tuned by varying their thickness to enable applications in Q-switching and mode locking. Lastly, we fabricated a

passive photonic diode by stacking $Ti_3C_2T_x$ MXenes with C_{60} (a reverse saturable absorber) in tandem to achieve nonreciprocal transmission of light, which is useful for optical isolator applications in fiber-based femtosecond lasers. We achieved a non-reciprocity factor as high as ~4 dB using $Ti_3C_2T_x$ MXenes/C_{60} bilayer structure for optical isolation without any phase-matching constraints or magnetic fields used in conventional optical isolators such as Faraday rotators.

4.2 Characterizations of MXene thin films

General characterization methods: The transmission spectra were measured from 200-1000 nm (UV-vis spectrometer QE Pro, Ocean Optics) using a bare cover glass as a baseline. X-ray diffraction patterns of film and MXene powder were measured by a powder diffractometer (PANalytical, Phillips MPD) with Cu $K_{<\alpha>}$ radiation (λ = 1.5425 Å, U = 45 kV, I = 40 mA). The morphology of the prepared MXene films was characterized using scanning electron microscope (SEM, HELIOS NANO LAB 600). AFM measurements were performed in a non-contact mode using AIST-NT SPM Smart system and cantilevers (HQ: NSC14/Al BS-50) from Micromasch. AIST-NT image analysis and processing (Version 3.2.14) software was used for AFM images analysis.

Synthesis of $Ti_3C_2T_x$ MXene

$Ti_3C_2T_x$ was synthesized by selective etching of aluminum atomic layers in Ti_3AlC_2 by MILD etching method described previously.[159], [164], [165] To synthesize MILD $Ti_3C_2T_x$, 1 g of lithium fluoride (LiF) was added to 20 mL of 6M hydrochloric acid (HCl) while stirring with a Teflon magnetic stir bar. Over the course of a few minutes, 1 g of Ti_3AlC_2 MAX phase was added to the LiF/HCl mixture and the reaction proceeded for 24

hours at 35 °C. After etching, the mixture was repeatedly washed with deionized water by centrifugation at 3500 rpm for 3 minutes and decanting of the acidic supernatant until a supernatant was obtained with a pH ~6. The supernatant was decanted, deionized water was added to the sediment, and the mixture was subjected to manual shaking for 5 minutes to delaminate the $Ti_3C_2T_x$ flakes. The solution was centrifuged for 1 hour at 3500 rpm and the supernatant was used for fabrication of $Ti_3C_2T_x$ films by the interfacial thin film technique.

Fabrication of MXene films by the interfacial thin film technique

About 50 mL of DI water was poured into a 100 mL glass beaker with a Teflon coated magnetic stir bar (Fig. 4.1). While vigorously stirring the DI water, a predetermined volume of $Ti_3C_2T_x$ aqueous colloid in the range 0.05, 0.1, 0.2, and 0.3 mL, was added into the glass vial for preparing thin films of different thicknesses. Under continued stirring, 4-6 mL of toluene was added into the vial and stirred vigorously for 20 minutes (Fig. 4.1a). Clean cover glass and silicon substrates (sonicated in acetone at room temperature for 40 minutes and dried) were hydrophilized by immersing into freshly prepared Piranha solution (3 parts of H_2SO_4 96% + 1 part of H_2O_2 30%) for 12 hours. After that, the substrates were rinsed with DI water, attached to a glass rod handle, and placed near the bottom of another 600 mL glass beaker filled with 400 mL water. The stirred $Ti_3C_2T_x$ MXene-toluene-water dispersion was quickly poured into the 600 mL glass beaker with the substrate attached to a glass rod and immersed in DI water. The beaker was left still for 20 minutes to allow layering out of the emulsion and the formation of the interfacial film (Fig. 4.1b). After the formation of $Ti_3C_2T_x$ thin film at the interface between water and toluene, the substrate was

slowly lifted toward the top of the beaker while keeping its surface oriented parallel to the interface. The MXene film coated the glass when it passed through the water-organic solvent interface. The coated substrate (with $Ti_3C_2T_x$ film on both sides, Fig. 4.1c) was detached from the glass rod and dried at ambient conditions in air for 12 hours. In the final step, the back side of the substrate was carefully rubbed with alcohol wetted paper to remove $Ti_3C_2T_x$ film so that only one side of the substrate remains coated (Fig. 4.1d).

Z-scan measurements and simulations: In our Z-scan setup (see Fig. 4.5a), a linearly polarized beam (7 ns, 1064 nm) from a Q-switched frequency-doubled Nd:YAG laser was focused by a converging lens (focal length of ~20 cm) to form an optical field of gradually changing laser intensity. The glass supported $Ti_3C_2T_x$ films were translated across the focal plane in the beam direction (*z*-direction) by placing them on a moving stage (PI instruments). A LabVIEW program synchronized the single-shot laser pulses with the moving stage and the resulting repetition rate was ~1 Hz. With the sample experiencing different optical intensities at each *z* position, the corresponding transmittance was recorded by a calibrated photodetector (RjP-7620, Laserprobe, Inc) placed on the sample translation axis. A more detailed description of our Z-scan technique can be found elsewhere[37], [59], [142], [166]. As described in the article, the space-time slicing model was performed by iteratively solving light propagation equations in MATLAB using Runge-Kutta method. All the parameters for the model including linear transmittance, pulse energy, pulse width, I_s, and β were extracted from experimental datasets.

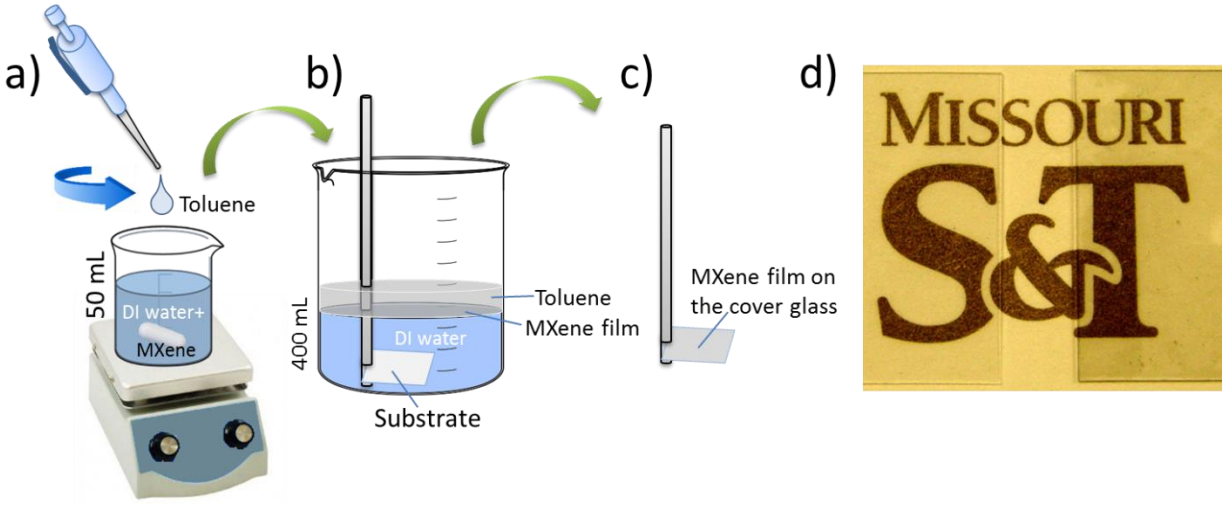

Figure 4.1. a-c) Procedure for preparing $Ti_3C_2T_x$ thin films with varying thicknesses (~ 5 – 67 nm) on glass and Si substrates via the interfacial film formation technique. d) The optical photograph shows transparent $Ti_3C_2T_x$ film (right side) uniformly covering a large area of 1 x 1 cm^2 glass substrates. Bare uncoated glass slide is shown on the left for comparison.

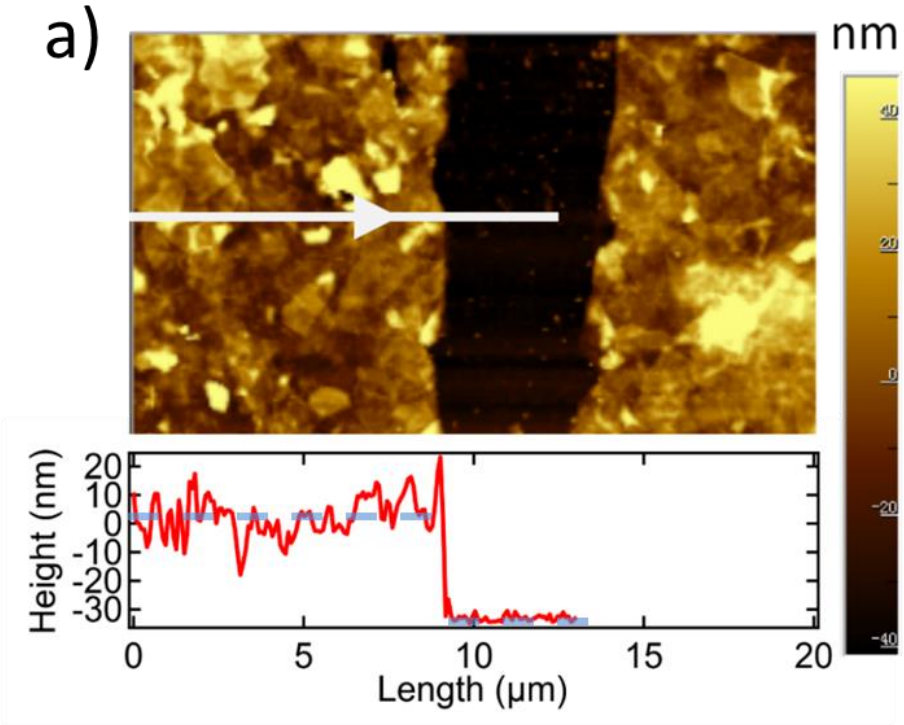
a)
nm
Height (nm)
Length (μm)

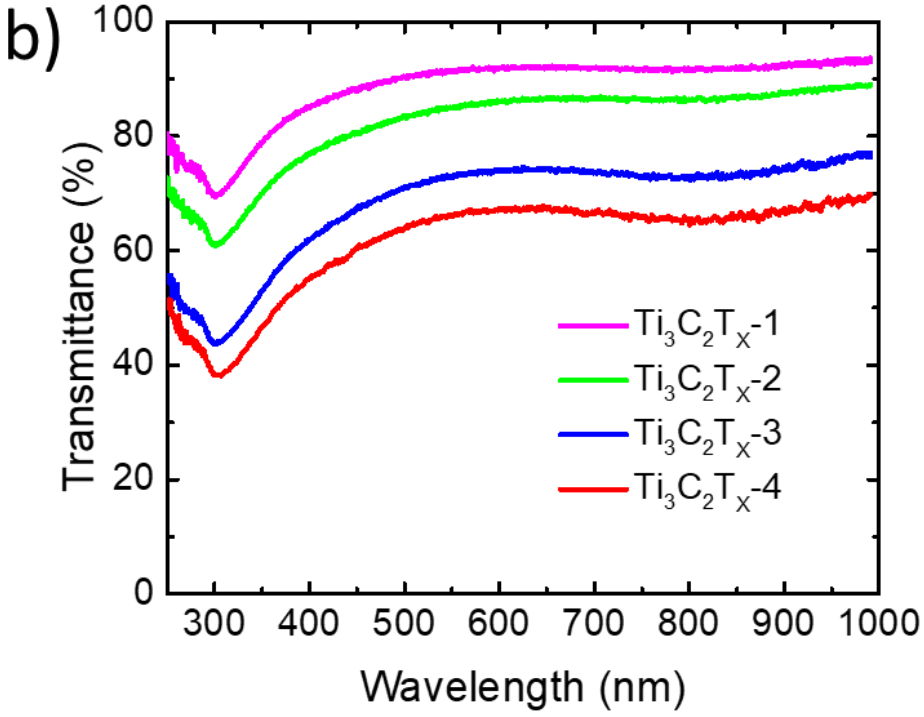
b)
Transmittance (%)
Wavelength (nm)
Ti3C2TX-1
Ti3C2TX-2
Ti3C2TX-3
Ti3C2TX-4

Figure 4.2. a) The average thicknesses and surface roughness of $Ti_3C_2T_x$ thin films were determined using atomic force microscopy (AFM). The white line represents the direction of the line scan, and the corresponding film thickness is shown in the panel below the AFM image. b) The UV-Vis spectra of the $Ti_3C_2T_x$ films with different thicknesses. Sample names are same as in Table 4.1.

Table 4.1. Parameters of $Ti_3C_2T_x$ thin films

Sample name	Thickness *h*, (nm)	Saturation fluence I_s, (W/cm^2)	Surface roughness, (nm)	Transmittance at 1000 nm (%)
$Ti_3C_2T_x$ -1	5	5.00E+9	3.6	93
$Ti_3C_2T_x$ -2	16	2.80E+9	4.2	89
$Ti_3C_2T_x$ -3	38	1.10E+9	8.7	77
$Ti_3C_2T_x$ -4	67	3.00E+8	11.8	69

a)

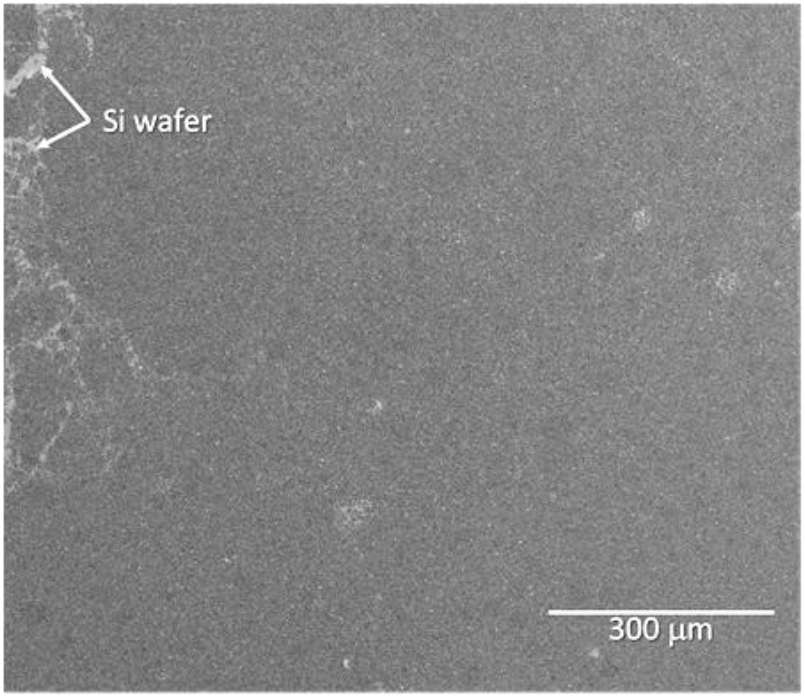
Si wafer
300 µm

b)

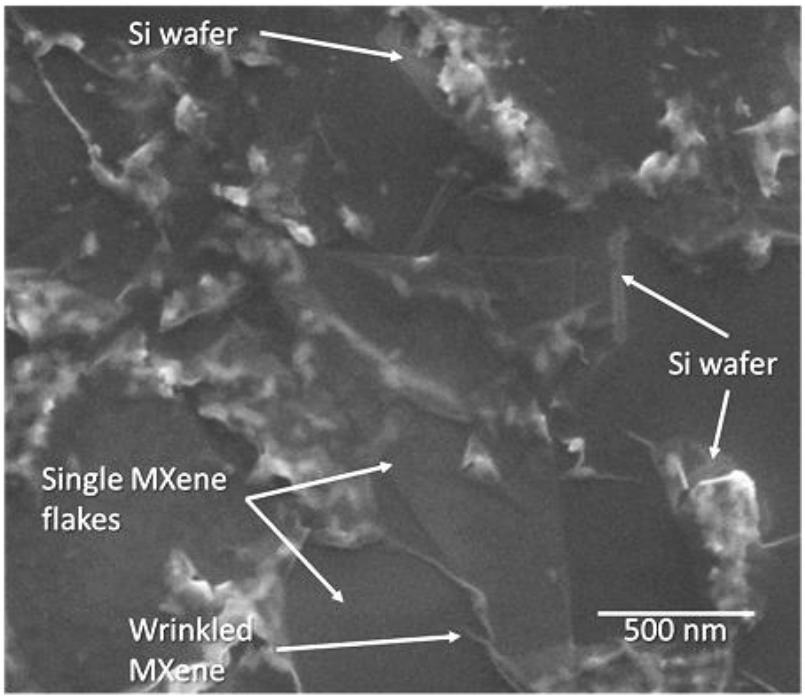
Si wafer
Si wafer
Single MXene flakes
Wrinkled MXene
500 nm

Figure 4.3. Low magnification scanning electron microscopy (SEM) image of the $Ti_3C_2T_x$−2 film shows smooth and uniform coverage of a large (~1 cm x 1 cm) area of the substrate (a). It also reveals micron-wide cracks in the film with the underlying Si wafer visible in the background. These large cracks were formed during film transfer from the liquid-liquid interface onto a solid support. Higher magnification SEM (b) shows thin individual semitransparent $Ti_3C_2T_x$ flakes of 1-2 micrometer lateral dimensions laying all in horizontal orientation, and touching or overlapping one another.

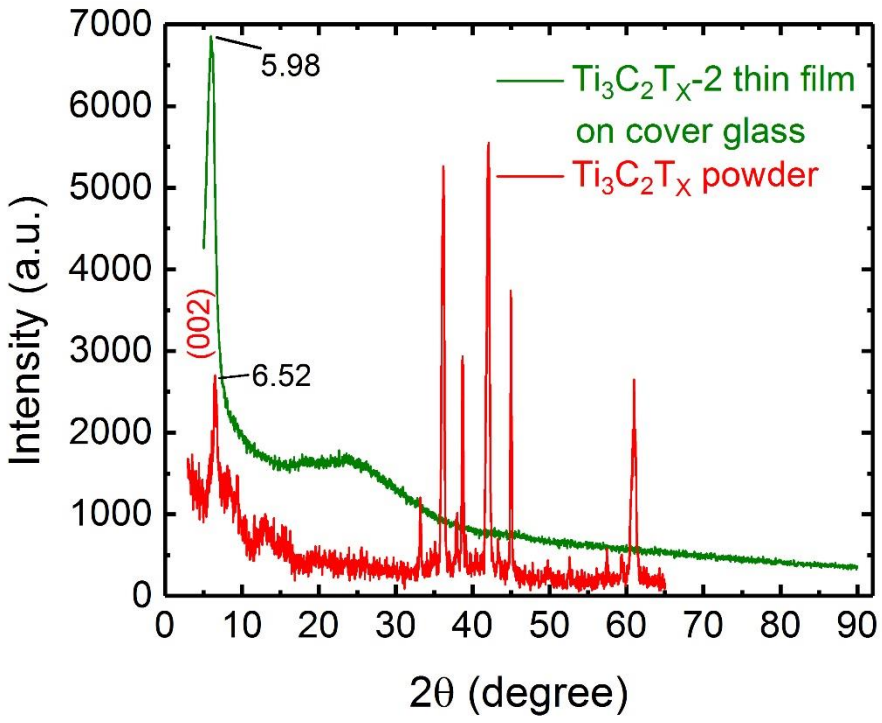

Figure 4.4. XRD pattern of $Ti_3C_2T_x$−2 film on cover glass shows the loss of registry in all directions except parallel to the glass surface. In contrast to multilayer $Ti_3C_2T_x$ there are no peaks in the 30 – 65 degrees range of 2θ. The disappearance of these peaks is indicative

of fully exfoliated $Ti_3C_2T_x$ flakes laying horizontally without any extended stacking in the vertical direction, i.e., forming a very thin film. The (002) peaks at 6.0° gives average separation distances of d_{hkl} = 1.48 nm for the deposited film.

4.3 Saturable absorption in MXene thin films and optical diode action

$Ti_3C_2T_x$ thin films were prepared on glass and Si substrates with varying thicknesses (h ~ 5 – 100 nm) using the interfacial film formation technique (Fig. 4.1). The films were characterized using scanning electron microscopy (SEM), atomic force microscopy (AFM), X-ray diffraction (XRD), and ultraviolet-visible (UV-vis) transmittance to evaluate their uniformity, thickness, composition, and linear optical absorbance, respectively (Fig. 4.2). As shown in Fig. 4.1d and SEM images (see Supporting Information, Fig. 4.3), the interfacial $Ti_3C_2T_x$ MXene films smoothly and uniformly covered large (~1 x 1 cm^2) area substrates. High magnification SEM (Fig. 4.3) showed thin individual transparent $Ti_3C_2T_x$ flakes of 1-2 μm lateral dimensions overlapping one another without any extended stacking in the vertical directions, which was also confirmed using XRD (see Fig. 4.4) and AFM (Fig. 4.2a). The average thicknesses and surface roughness of $Ti_3C_2T_x$ thin films were deduced from multiple AFM line scans (Fig. 4.2a and Table 4.1), which showed that the surface roughness of the $Ti_3C_2T_x$ thin films increased with increasing film thickness.

The linear optical transmittance of the $Ti_3C_2T_x$ films correlates well with their thicknesses (Fig. 4.2b, Table 4.1), and the transmittance at 1000 nm (relevant for nonlinear optical excitation ~1064 nm) is listed in Table 4.1. The $Ti_3C_2T_x$ films displayed a broad

valley in their optical transmission spectra ~780-800 nm. This is attributed to surface plasmon resonance in $Ti_3C_2T_x$ centered at 780 nm and was previously used for surface enhanced Raman spectroscopy with $Ti_3C_2T_x$ MXene substrates.[167] Previously, Dillon *et al*. measured the real and imaginary components of the dielectric constants, given by ε_1 and ε_2, for $Ti_3C_2T_x$ films using ellipsometry[168]. The imaginary component ε_2, was found to exhibit a peak ~ 800 nm, which concurs with the observed valley in the transmission spectra shown in Fig. 4.2b. Furthermore, Dillon *et al*. found a crossover from positive to negative values for ε_1 at wavelengths greater than 1130 nm, indicating the onset of free carrier oscillations at low photon energies (<1 eV) [168]. The crossover point for ε_1 was observed to be dependent upon film thickness with ε_1 in thinner films attaining negative values at longer wavelengths. This suggests that the nonlinear optical properties may also exhibit thickness dependence similar to linear transmission (Fig. 4.2b). Mauchamp *et al*. observed that $Ti_3C_2T_x$ films exhibit two surface plasmon peaks with an intense sharp peak ~0.3 eV (~4100 nm) and a broader shoulder ~1.2 eV (~1030 nm) using electron energy-loss spectroscopy[169]. In this work, we hypothesize that the SA behavior in $Ti_3C_2T_x$ MXene films arises from plasmon-induced increase in the ground state absorption at 1064 nm.

It is well known that surface plasmon resonances in noble metal nanoparticles such as Au and Ag strongly enhance light-matter interactions. In these materials, a strong plasmon-induced increase in the local electric field is known to enhance SA by increasing the absorption cross section of the ground state[170]–[173]. However, the observation of SA is often precluded due to a concomitant increase in free carrier oscillations and

excited state absorption in Au and Ag nanoparticles. The observation of SA behavior in metal nanoparticles necessitates careful tuning of size below 2 nm[174]. On the other hand, $Ti_3C_2T_x$ thin films exhibit increased ground state absorption at ~1064 nm (1.16 eV) due to the plasmon resonance, while free carrier oscillations (as evidenced from ε_1 crossover point[168]) occur at longer wavelengths or lower energies ~1130 nm (<1.1 eV). Thus, unlike noble metal nanoparticles, SA behavior arising from plasmon-induced increase in ground state absorption is visible in $Ti_3C_2T_x$ films with different thicknesses, as described below.

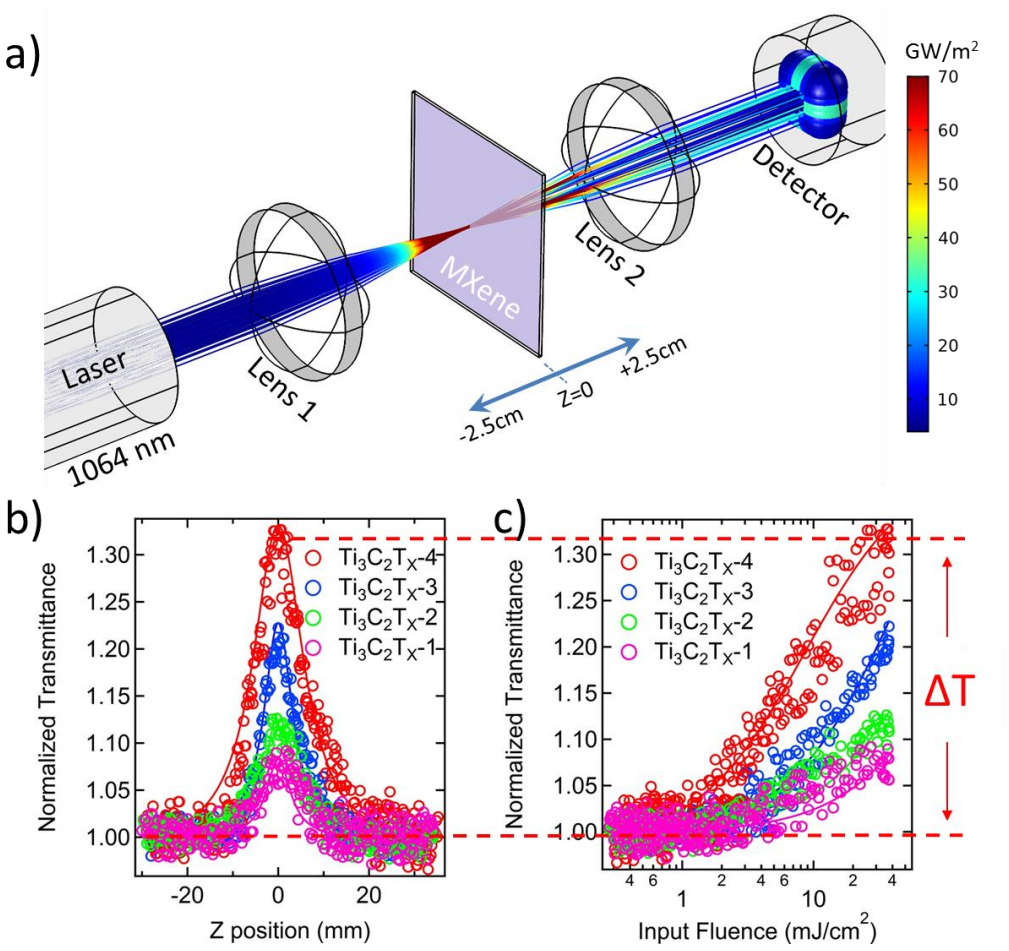

Figure 4.5. a) The $Ti_3C_2T_x$ thin films experience varying laser intensities when translated across the focal plane as illustrated by a COMSOL simulation of the field intensity. b) The position-dependent changes in the non-linear transmittance or the modulation depth (ΔT) of the $Ti_3C_2T_x$ films as measured by the Z-scan method. c) Nonlinear transmission of $Ti_3C_2T_x$ films plotted as a function of intensity at each sample position.

The open aperture Z-scan method was used to characterize the nonlinear optical properties of $Ti_3C_2T_x$ thin films. In the setup, a Q-switched frequency-doubled Nd:YAG laser beam (1064 nm, 7 ns) was focused using a converging lens (lens 1 in Fig. 4.5a, focal length: 20 cm) to a spot size of 100 μm onto a glass supported $Ti_3C_2T_x$ film mounted on a moving stage (Fig. 4.5a). The transmitted beam, whose intensity is dependent on the sample position, was focused using another converging lens (lens 2 in Fig. 4.5a) onto a photodetector, as shown in Fig. 4.5a. As shown in Fig. 4.5b, the Z-scan experiment measures the position-dependent change in the non-linear transmittance or the modulation depth of the $Ti_3C_2T_x$ films $\Delta T(z) = \frac{T_{NL}(z) - T_0}{T_0}$, where T_{NL} is the nonlinear transmission and T_0 is the corresponding linear transmittance at 1064 nm (plotted as ΔT vs. sample position or z). The $Ti_3C_2T_x$ thin films experience varying laser intensities when translated across the focal plane as illustrated by a COMSOL simulation of the field intensity in Fig. 4.5a, which is given by $I(z) = \frac{I_0}{1 + \left(z / w_0\right)^2}$, where I_0 is the intensity at the focal point (corresponding to z=0), z is the sample position, and w_0 is the laser beam width. Combining the equations for $\Delta T(z)$ and $I(z)$, the nonlinear transmission of $Ti_3C_2T_x$ films for a fluence of 40 mJ/cm^2 is calculated and plotted as a function of intensity at each sample position (Fig. 4.5c). The experimental data in Figs. 4.3b-c were fitted using the nonlinear light propagation equation, $\frac{dI}{dz} = -\alpha(I)I$ to obtain the saturation fluence for $Ti_3C_2T_x$ films of

different thicknesses (see Table 4.1). The following observations can be deduced from experimental data in Figs. 4.3b-c and the I_s extracted by fitting the data: i) the SA behavior is universal in $Ti_3C_2T_x$ irrespective of the film thickness, ii) the modulation depth is directly dependent upon the film thickness with higher ΔT for thicker films, and iii) I_s varies inversely with the film thickness (see Table 4.1 and Fig. 4.6a).

The universal observation of SA behavior for different thicknesses can be understood in terms of plasmon-induced increase in the ground state absorption at 1064 nm. Given that free carrier oscillations are more favorable at longer wavelengths >1130 nm (or lower energies <1.1 eV) in MXenes, the depletion of ground state population is more dominant at 1064 nm (~1.16 eV) resulting in increased nonlinear transmittance at higher fluences or SA behavior. Importantly, the modulation depth or ΔT for the thicker $Ti_3C_2T_x$ MXene thin films was found to be 30% at 40 mJ/cm^2, which is nearly five times the ΔT of a few-layer graphene (FLG exhibits ΔT ~6% at 40 mJ/cm^2, Fig. 4.7)[91], [175] measured in the same experimental setup. The large modulation depth of $Ti_3C_2T_x$ is highly useful for applications in mode locking and Q-switching.

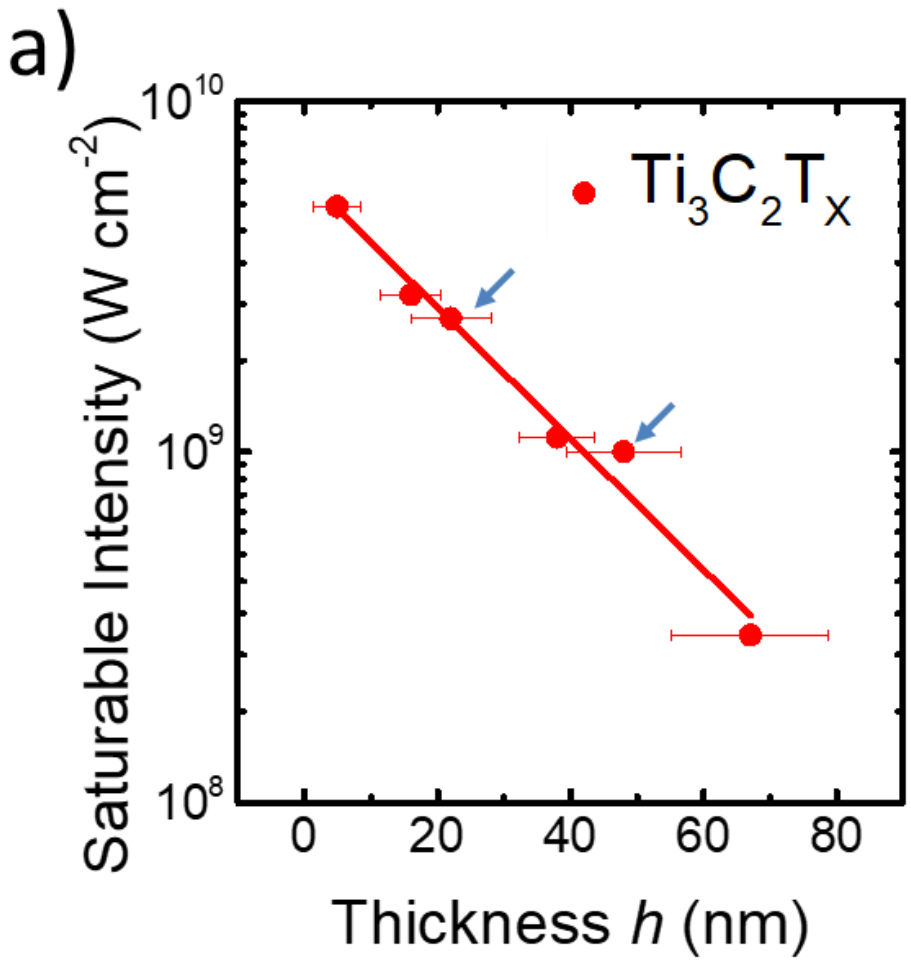
a)
Saturable Intensity (W cm-2)
10^10
10^9
10^8
0
20
40
60
80
Thickness h (nm)
Ti3C2Tx

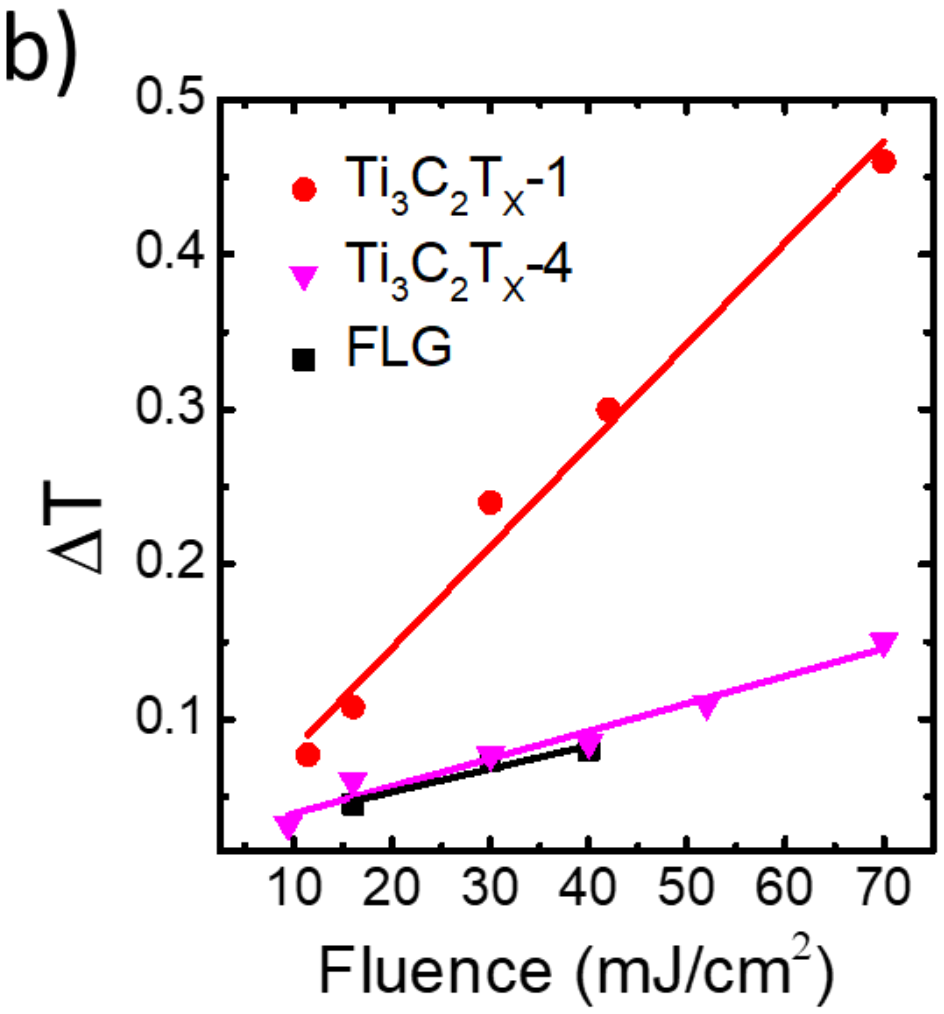

Figure 4.6. a) The saturation fluence (I_s) for $Ti_3C_2T_x$ thin films (at 40 mJ/cm^2) decreases significantly with increasing film thickness. I_s for two additional samples $Ti_3C_2T_x$-2 and $Ti_3C_2T_x$-3 are also shown in the plot (indicated by blue arrows). b) The SA behavior of $Ti_3C_2T_x$-1 and $Ti_3C_2T_x$-4 as a function of increasing laser energies. Refer to Table 4.1 for sample names.

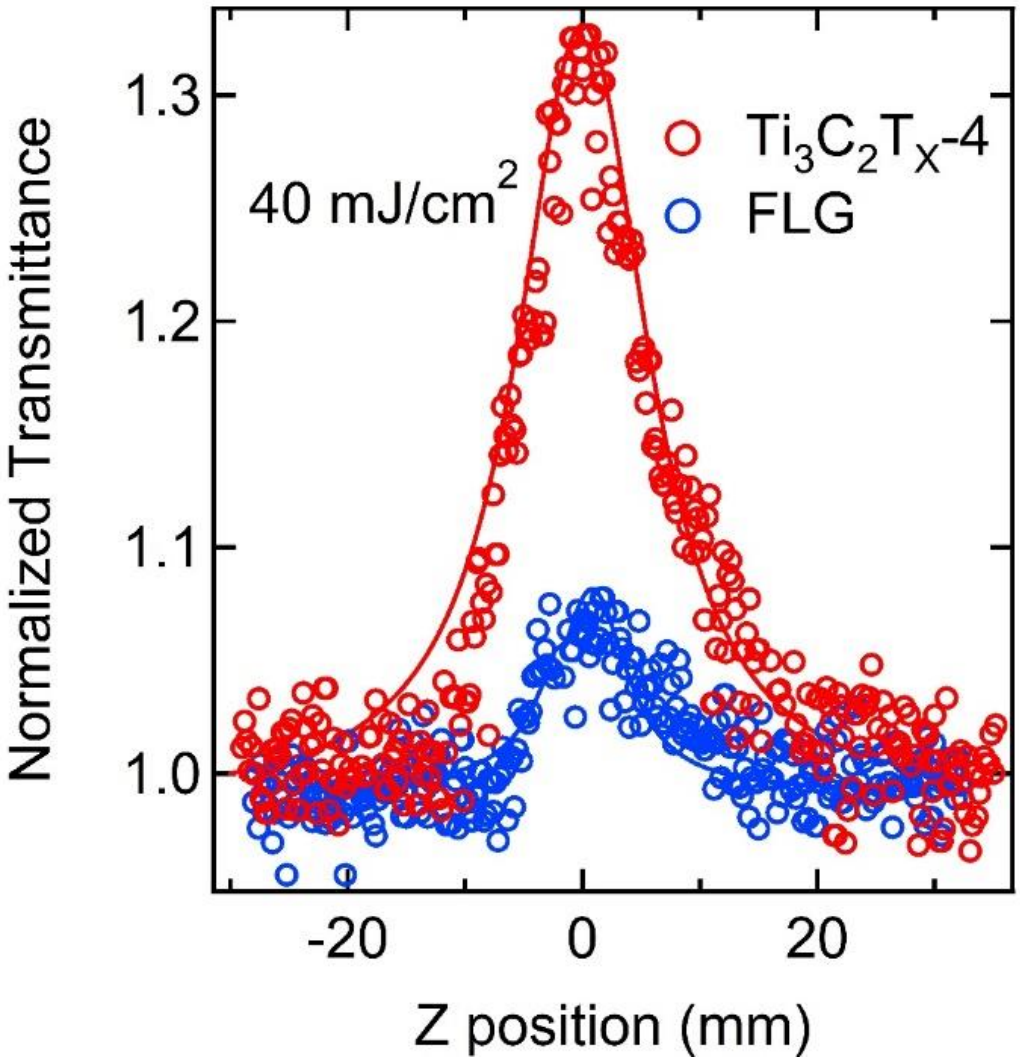

Figure 4.7. Normalized Z-scan transmittance of FLG and $Ti_3C_2T_x$-4.

As shown in Fig. 4.6a, we note that I_s for $Ti_3C_2T_x$ decreases significantly with increasing film thickness, which may be understood in terms of stronger optical absorption (*cf.* Table 4.1) and higher imaginary component of the dielectric constant for thicker $Ti_3C_2T_x$ films[168], as described below. The saturation carrier density (N_s) in 2D materials

could be estimated using a simplified approximation given by Bao *et al*. as $N_s = \frac{\alpha I_s \tau}{\hbar\omega}$, where α is the absorption coefficient, τ is the carrier relaxation time, $\hbar$ is reduced Planck's constant and ω is the excitation frequency[8]. Chemla *et al*. argued that in the case of 2D electron gas, absorption saturation occurs when photo-generated carrier density is about one charge carrier per exciton volume $4\pi a_o^3/3$ where a_0 is the Bohr radius[77]. Accordingly, I_s can be approximated as $I_s = 3\hbar\omega/(4\pi a_o^3 \alpha\tau)$. It then follows that for a given excitation, I_s is related to α through an inverse relation. Dillon *et al*.[168] experimentally showed that the imaginary component of the dielectric constant is higher for thicker films suggesting that I_s decreases with increasing thickness concurring with the data presented in Fig. 4.6a. A low saturation fluence allows SAMs inside the laser cavities to work effectively for pulse shaping applications. Although other 2D materials such as graphene and MoS_2 exhibit lower I_s than $Ti_3C_2T_x$ [149], they cannot withstand higher laser energies. On the other hand, the SA behavior in $Ti_3C_2T_x$ was found to be resilient at high laser energies (Fig. 4.6b), and the modulation depth increases with increasing laser energies similar to FLG. A maximum modulation depth ~50% was observed at 70 mJ/cm^2 for a 67 nm thick $Ti_3C_2T_x$ film. While the clear degradation of FLG was observed when the laser energy reached ~40 mJ/cm^2, both ~5 and 67 nm thick $Ti_3C_2T_x$ films were able to withstand high laser energy ~70 mJ/cm^2 (Fig. 4.6b). In Q-switched lasers, the laser-induced damage of the SA will lead to a severe instability of Q switching. In this regard, the use of $Ti_3C_2T_x$, and possibly other MXenes, as SAMs is more favorable compared to other 2D materials due to their higher damage threshold.

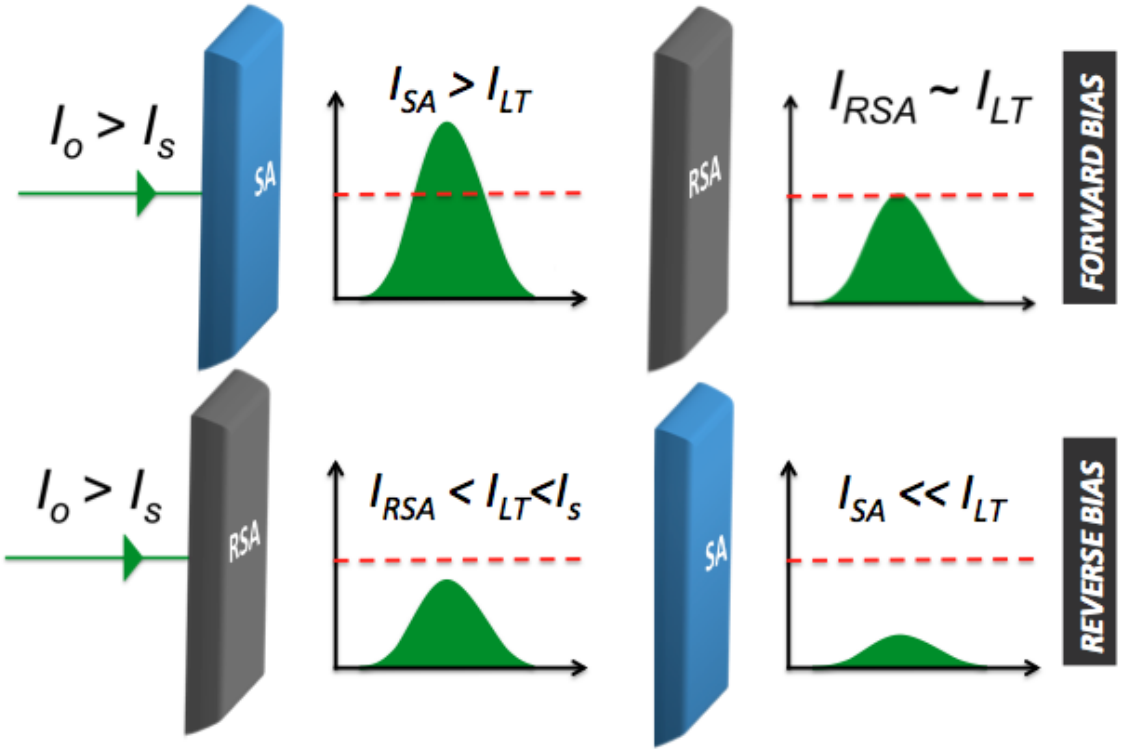

Figure 4.8. The mechanism of photonic diode action from a SA/RSA bilayer can be understood as follows. In the forward bias configuration of a photonic diode, when incident light intensity (I_o) is above the threshold (I_s), transmission through SA (I_{SA}) is increased beyond linear transmission (I_{LT}). The RSA layer then attenuates I_{SA} resulting in an output intensity ~I_{LT}. However, in a reverse bias configuration, the RSA attenuates light below I_S eliciting only a linear response in SA. Thus, the output intensity is lower than the intensity in the forward bias case.

We demonstrate that the SA behavior in $Ti_3C_2T_x$ MXene can be used to fabricate a photonic diode that exhibits nonreciprocal transmission of light similar to current flow in an electronic *p*-*n* junction diode. The time-reversal symmetry in the electromagnetic wave equation implies intrinsic reciprocity in light transmission, *i.e.*, swapping the light source

and detectors while keeping the sample fixed should not alter the transmission. We previously showed that the time-reversal symmetry could be broken using a bilayer structure containing a SAM and a reverse saturable absorption material (RSAM)[37]. While a SAM or RSAM exhibits spatially reciprocal light transmission, the transmission characteristics become non-reciprocal when a laser pulse with input fluence $F_{in} > I_s$ propagates *sequentially* through a SAM/RSAM bilayer (see supporting information Fig. 4.8). Here, we used C_{60} as a RSAM [71] and $Ti_3C_2T_x$ MXene as the SAM for achieving a photonic rectification (photonic diode) function. In the forward direction ($Ti_3C_2T_x$ MXene followed by C_{60}), input pulse shows an increased transmission through $Ti_3C_2T_x$ MXene (a SAM) when its input fluence $F_{in}>I_s$. Subsequently, this transmitted pulse is attenuated by C_{60} (a RSAM) through multi-photon absorption. The overall response is an increase in light transmission (higher than linear transmittance) if the SA effects overwhelm RSA. On the other hand, in the reverse direction (C_{60} followed by $Ti_3C_2T_x$ MXene), the input laser pulse with same fluence as in the forward direction ($F_{in} > I_s$) is attenuated below I_s by C_{60} due to multi-photon absorption[71], [166]. The transmitted laser pulse ($F_{transmitted} < I_S$) from C_{60} does not elicit a high transmittance through the $Ti_3C_2T_x$ film leading to decreased transmission (Fig. 4.8). We used a "space-time slicing" model to capture the diode action of the MXene/C_{60} bilayer on the basis of the following nonlinear light propagation equation $\frac{dI}{dz} = -\alpha(I)I$ with no *a priori* assumptions, wherein $\alpha(I) = \frac{\alpha_0}{1 + I/I_s}$ for $Ti_3C_2T_x$ MXene as stated noted previously in the discussion of Fig. 4.5. For C_{60}, $\alpha(I) = \alpha_0 + \beta I$ wherein β is the two-photon absorption coefficient of C_{60}. Our model extracts transmission

characteristics of $Ti_3C_2T_x$ MXene/C_{60} bilayers using experimentally determined parameters such as I_s and β, without the need to introduce free parameters. In forward bias (see Fig. 4.9a), a 7 ns Gaussian pulse was first sliced in time with equal width ~70 ps. Each temporally sliced part of the Gaussian pulse first propagates through SA (sliced in space with ~1 nm thickness for each slice) and the output intensity is calculated by solving the propagation equation for SA via Runge-Kutta method. The transmitted pulse from n^{th} space slice serves as the input pulse for n+1th slice. At the end of MXene layer (e.g., 67 nm in $Ti_3C_2T_x$-4), the output intensity is calculated by solving the propagation equation for ~50 slices of RSA (with ~1 nm thickness). In the reverse bias case, the order of solving the propagation equations was reversed. As observed in Fig. 4.9b, the output pulses from the $Ti_3C_2T_x$ MXene/C_{60} bilayer show different intensities in forward and reverse bias directions. Nonlinear transmission curves for the photonic diode (similar to Fig. 4.5c), generated by using different input pulse intensities in the space-time slicing model (Fig. 4.9c), showed that the transmission for $Ti_3C_2T_x$ MXene/C_{60} bilayer increases with intensity in the forward direction while it decreases in the reverse direction above 4 mJ/cm^2. Our experimental data for $Ti_3C_2T_x$/C_{60} bilayer concurs with the space-time slicing model showing nonreciprocal light transmission >1 mJ/cm^2 with an increasing difference between forward and reverse transmission characteristics (Fig. 4.10 and Table 4.2). We observed that the non-reciprocity factor (defined as the gain in dB = 10 log ($T_{forward}$/$T_{reverse}$), where $T_{forward}$ and $T_{reverse}$ are the nonlinear transmission values for forward and reverse directions shown in Fig. 4.9) could be tuned by varying $Ti_3C_2T_X$ MXene thickness and linear transmission (Table 4.2 and supporting information Fig. 4.11). Indeed, we achieved a

maximum nonreciprocity factor as high as ~4 dB with ~100 nm $Ti_3C_2T_X$ MXene/C_{60} bilayers. Unlike magneto-optical isolators in fiber-coupled lasers that are constructed based on Faraday rotators, MXene/C_{60} bilayers exhibit nonreciprocal transmission irrespective of angle of incidence or polarization in addition to being ultra-compact (~100 nm). Although the nonreciprocity factor is only moderate ~4 dB compared to traditional optical isolators that could achieve ~30-40 dB, the demonstrated photonic diode characteristics provide the basis for the use of a wide range of MXene compositions with better SA properties (e.g., Ti_2CT_x, Mo_2CT_x, Ti_3CNT_x, etc.) in photonic diodes and optical isolators without the need for bulky components or magnetic fields.

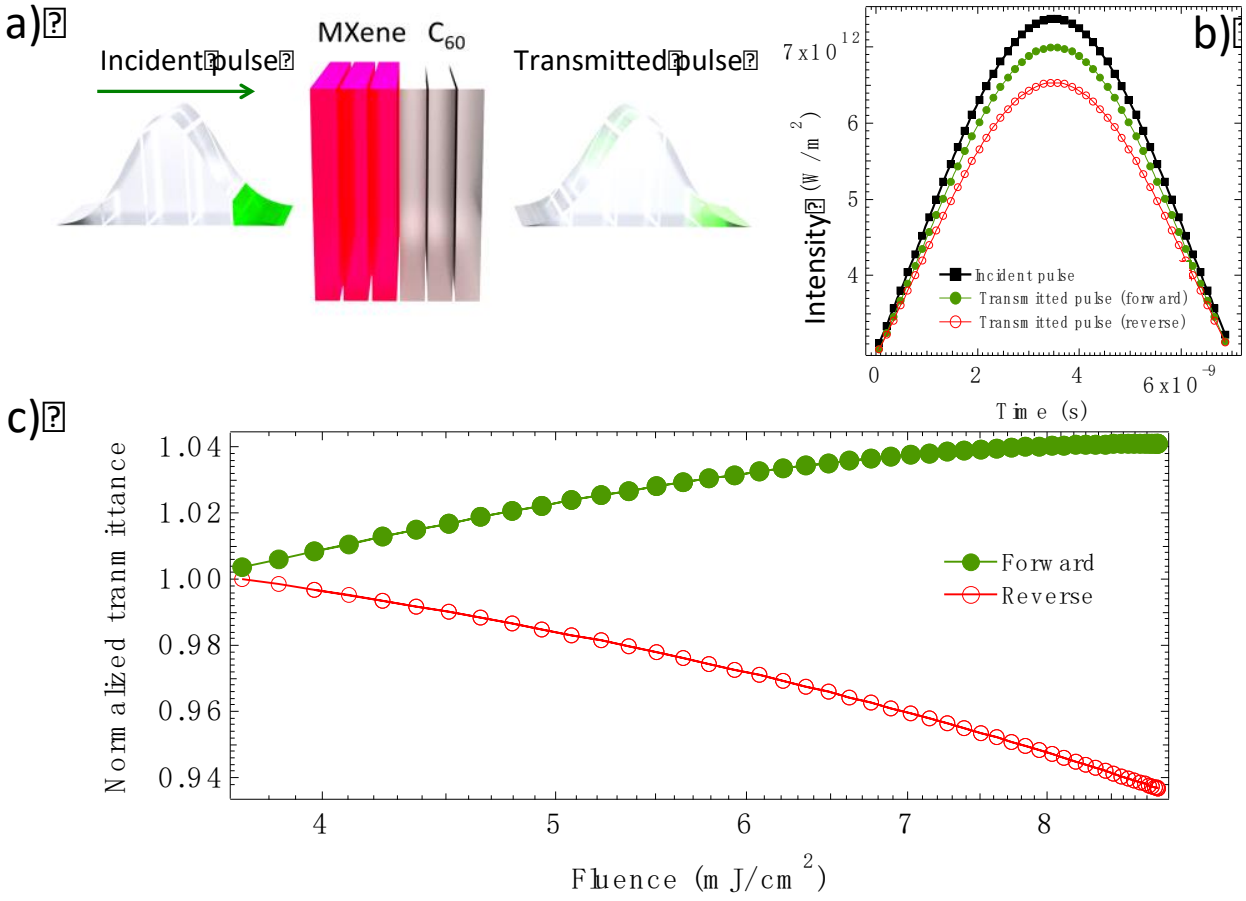

Figure 4.9. a) The non-reciprocal transmission characteristics are simulated by a "space-time slicing" model shown in the schematic, which solves the pulse propagation equations for $Ti_3C_2T_x$ MXene and C_{60} sequentially. The 7-ns laser pulse and the sample length are sliced in order to take into consideration the temporal and spatial variations in the input intensity, respectively. Each temporal slice passes through each of the sample slices whereby its intensity gets modified due to nonlinear as well as linear absorptions (SA in $Ti_3C_2T_x$ MXene slices and RSA in C_{60} slices). The output pulse is reconstructed from the modified temporal slices and the transmittance is calculated. b) An incident laser pulse with 20 μJ energy (40 mJ/cm^2 at z = 0) and 7 ns pulse width reconstructed after transmission in

forward ($Ti_3C_2T_x$ MXene/C_{60}) and reverse (C_{60}/$Ti_3C_2T_x$ MXene) directions using the space-time slicing model. c) Simulated nonlinear light transmission for a $Ti_3C_2T_x$ MXene/C_{60} bilayer using the space-time slicing model by varying the incident pulse energy.

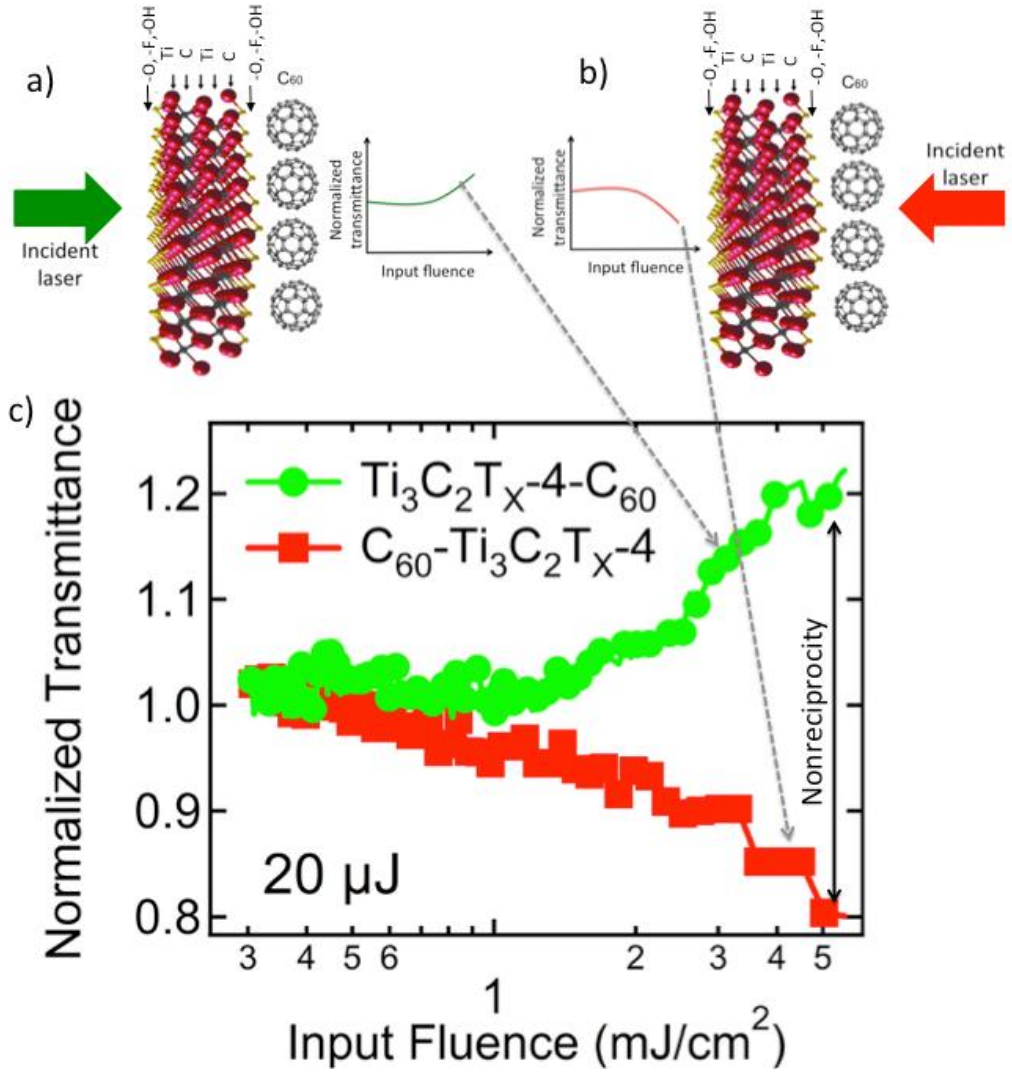

Figure 4.10. Optical diode action in a $Ti_3C_2T_x$-MXene/C_{60} bilayer. a) and b) show the schematics for forward and reverse bias configurations for the $Ti_3C_2T_x$-MXene/C_{60} bilayer. c) Experimental nonlinear transmission data obtained from the Z-scans on a

$Ti_3C_2T_x$-4 MXene/C_{60} bilayer. A ~40% change in transmittance was evident for an incident fluence of 5 mJ/cm^2.

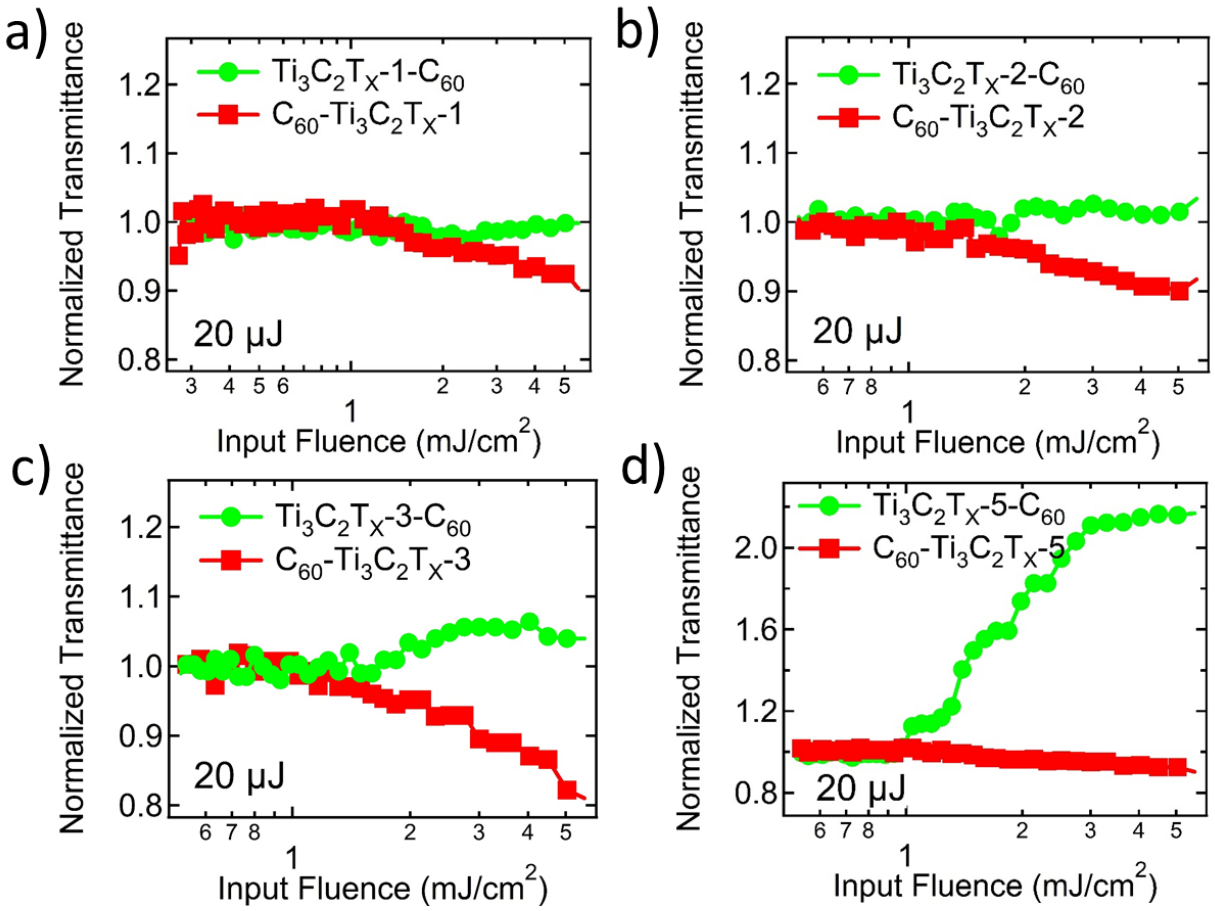

Figure 4.11. (a-d) Experimental nonlinear transmission data obtained from the Z-scans on $Ti_3C_2T_x$ MXene/C_{60} bilayers (at 5 mJ/cm^2) in which the thickness of the MXene was varied.

Table 4.2. Non-reciprocity factors for photonic diodes with different $Ti_3C_2T_x$ thicknesses

Sample name	Thickness *h*, (nm)	Non-reciprocity factor, at 5 mJ/cm^2 (dB)
$Ti_3C_2T_x$ -1	5	0.46
$Ti_3C_2T_x$ -2	16	0.63
$Ti_3C_2T_x$ -3	38	0.92
$Ti_3C_2T_x$ -4	67	1.80
$Ti_3C_2T_x$ -5	~100	4.13

4.4 Conclusion

In summary, this study identifies plasmon-induced increase in the ground state absorption well above the free carrier oscillation energy as the primary mechanism for SA in $Ti_3C_2T_x$ thin films fabricated by the interfacial technique. Our observations suggest that $Ti_3C_2T_x$ films are ideal for applications in modelocking and Q-switching because: i) $Ti_3C_2T_x$ films exhibited a significantly higher modulation depth up to ~50% (at least five times higher compared to FLG at 40 mJ/cm^2), ii) the saturation fluence of $Ti_3C_2T_x$ films is easily tunable by changing the film thickness, iii) MXenes are more resilient than other 2D materials with high damage thresholds ~70 mJ/cm^2. Lastly, the SA behavior in MXenes leads to the possibility of fabricating passive photonic diodes that are ultra-compact, independent of phase-matching and polarization conditions needed for conventional Faraday rotator based optical isolators.

CHAPTER FIVE

THZ SPECTROSCOPY STUDY OF MXENEs

Guangjiang Li, *et al*. "Equilibrium and non-equilibrium free carrier dynamics in two-dimensional $Ti_3C_2T_x$ MXenes: THz spectroscopy study". Reproduced in part from submitting manuscript.

5.1 The principle of THz spectroscopy

The recent emergence of two-dimensional (2D) materials facilitated the realization of novel optoelectronic and nanophotonic applications. In addition to extraordinary and strongly anisotropic electronic properties, many 2D materials exhibit strong light-matter interactions despite their atomic thickness [112], [133], [137], [140], [176]–[178]. Indeed, the strong optical absorption of single-layer graphene ~2.3% in visible and infrared regions was critical to the initial observations of exfoliated monolayers under an optical microscope [179]. Following the discovery of strong light-matter interactions in graphene, it was found that monolayers of other 2D materials such as MoS_2 and WSe_2 exhibit even higher optical absorption, ~10% in the visible region [180]. While the electronic and optical properties of graphene, MoS_2, and WSe_2 can be engineered by doping or through fabrication of layer-by-layer heterostructures, their applications in high-power lasers has been limited by low damage thresholds[149]. In this regard, others and we recently demonstrated that an emerging class of 2D titanium carbides and carbonitride, MXenes, are ideal for femtosecond mode locking and optical isolation applications due to their high,

≈70 mJ cm^{-2} threshold for light-induced damage with up to 50% modulation depth[178]. MXenes are 2D transition metal carbides and nitrides with the chemical formula $M_{n+1}X_nT_x$ (n = 1-3), where M is an early transition metal, X is carbon and/or nitrogen, and T_x represents surface termination groups such as =O, –OH, –F, etc [150], [152], [155], [164], [165], [168], [181]–[183]. MXene surfaces are passivated during synthesis without any dangling bonds, which allows for easy integration with photonic structures such as waveguides and cavities[149]. In addition to potenial photonic applications, layered 2D titanium carbides are actively researched as novel precious-metal-free conductive materials for electrochemical energy storage, with demonstrated ultrahigh volumetric capacitance up to 900 F/cm^3[150], transparent conductive electrodes and efficient photothermal convertors[155], [168]. Recent studies have demonstrated that efficiency of light-to-heat conversion in MXenes including $Ti_3C_2T_x$ can reach 100%, suggesting their applications in photothermal solar energy conversion devices as well as in novel photothermal tumor ablation approaches in oncology[184]. High electrical conductivity of $Ti_3C_2T_x$ results in a strong absorption across the microwave and terahertz (THz) range and makes it a promising new material for electromagnetic shielding[185]. Combined with thermoelectric properties of $Ti_3C_2T_x$ MXenes, rivaling those of carbon nanotube films, large THz absorption also suggests potential application in THz detectors[149], [186]. Considering a wide range of potential photonic, electronic and electrochemical applications of MXenes, it is imperative to address exisiting knowledge gap to elucidate intrinsic carrier zero-field mobility within individual nanosheets and in thin conductive films and understand the effects of

photoexcitation on conductivity and ultrafast nonequilibrium dynamics of photoexcited carriers.

We have used terahertz (THz) spectroscopy to study both equilibrium and non-equilibrium free carrier dynamics in a 16 nm thick $Ti_3C_2T_x$ MXene film. Picosecond-duration THz pulses with the bandwidth of 0.25-2 THz, or 1-10 meV, are uniquely suited for probing microscopic conductivity and free carrier dynamics. We report native frequency-dependent complex THz sheet conductivity, as well as the impact of photoexcitation with near-IR, 800 nm pulses on sheet conductivity and carrier mobility.

We find that the mobility of intrinsic carriers is within the individual metallic $Ti_3C_2T_x$ nanoplatelets is ~ 80 cm^2/Vs. Long-range mobility within the film appears to be strongly suppressed by grain boundaries between the nanoplatelets. We observe that photoexcitation with 800 nm pulses results in a transient suppression of conductivity that persists for hundreds of picoseconds. Like in graphene and other metallic systems, photoexcitation raises the temperature of the entire free carrier population, which then cools by emission of phonons and increasing the lattice temperature. Increased lattice temperature manifests in enhanced carrier scattering rate which leads to a suppressed conductivity. The conductivity recovers as the lattice cools by transfering heat both to the glass substrate underneath (vertically) and to the unexcited nanosheets within the sample (laterally). This process is significantly slower in $Ti_3C_2T_x$ film than in metallic graphene, lasting for hundreds of picoseconds compared to picoseconds time scale in graphene due to inherently lower thermal conductivity in a film composed of $Ti_3C_2T_x$ nanoplatelets with 100-500 nm lateral dimensions.

5.2 THz spectroscopy setup

5.2.a $Ti_3C_2T_x$ film

The fabrication $Ti_3C_2T_x$ film is described in 4.2. Representative atomic force microscopy images of the film studied here, labeled as $Ti_3C_2T_x$-4 (Fig. 5.1 (a-c)) show that it consists of crystalline platelets of the average height ~16 nm and lateral dimensions ~100-500 nm. Optical transmittance of the film is shown in Fig. 5.1(d). Despite the small thickness, the film is highly absorptive, with ~ 15% of incident light around 800 nm being absorbed.

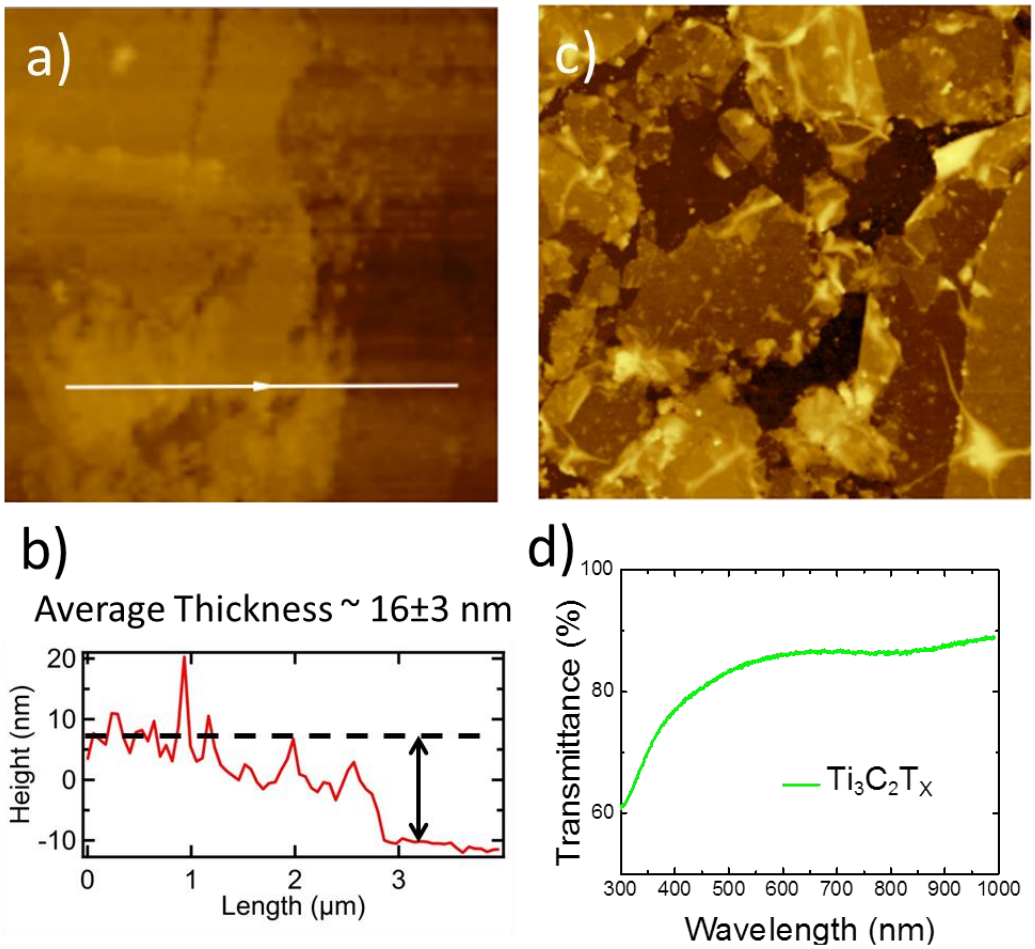

Figure 5.1. AFM characterization of $Ti_3C_2T_x$ films on glass substrates: individual nanosheets are ~ 16 nm thick (a,b) and have lateral dimensions of 2-5 μm (c). UV-VIS spectroscopy: film transmittance at 800 nm is ~ 85% (d).

5.2.b THz spectroscopy

We investigated native conductivity of the $Ti_3C_2T_x$ film using THz time-domain spectroscopy in the transmission configuration[187]–[189]. THz probe pulses were generated by optical rectification of 100 fs, 800 nm pulses in 1 mm thick [110] ZnTe crystal. A combination of three off-axis parabolic mirrors collimated and focused the emitted THz pulses into a ~ 2 mm spot. The sample was placed behind the 1.5 mm aperture in the center of the THz spot. At normal incidence, THz pulse probes conductivity in the basal plane of $Ti_3C_2T_x$ film. Transmitted THz pulses were detected using free-space electrooptic sampling in the second 1 mm thick [110] ZnTe crystal. Coherent detection of the amplitude and phase of THz probe pulses in the time domain allows extracting the frequency-dependent complex conductivity of the sample by comparing the THz pulses transmitted through the substrate alone and the sample of the substrate. We have also examined the effect of photoexcitation of conductivity and carrier dynamics using optical pump – THz probe measurements[189]–[193]. The sample was excited by 100 fs duration, 800 nm pulses. Optical pump beam was focused to a ~ 5 mm spot at the sample location, ensuring that the probe THz pulse interrogates optically-induced changes in the uniformly photoexcited portion of the MXene film.

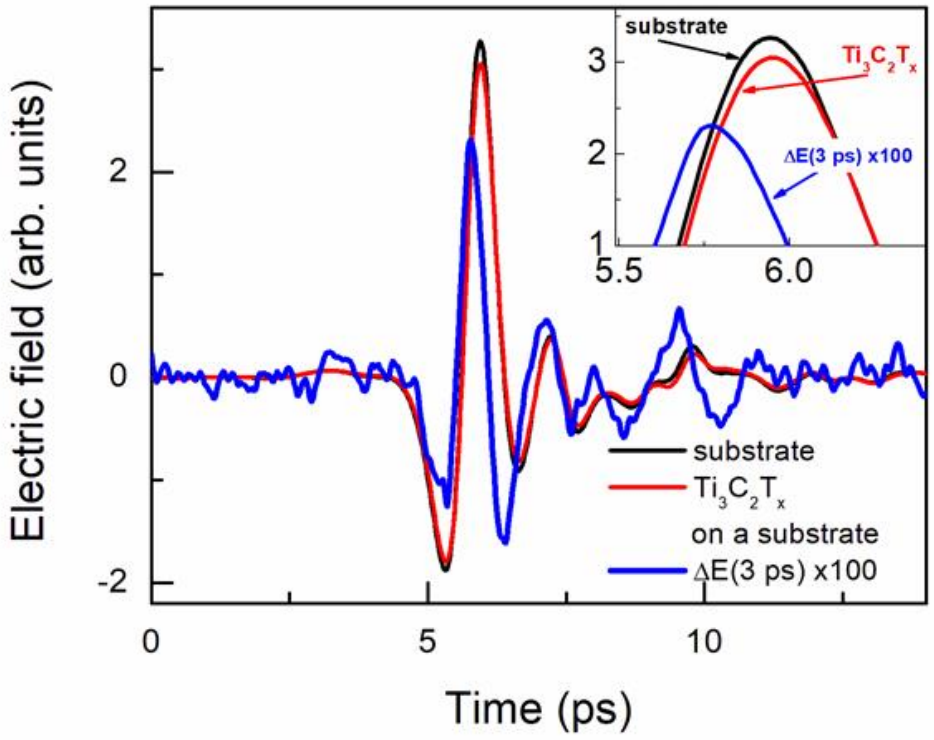

Figure 5.2. THz waveforms transmitted through the glass substrate ((black curve) and through the $Ti_3C_2T_x$ film on the substrate (red). Photoinduced change in THz waveform transmission 3 ps after photoexcitation with 280 μJ/cm^2, 800 nm, multiplied by 100 for clarity, is shown in blue. Inset shows expanded view of the same waveforms.

5.3 Probing MXene thin films with THz spectroscopy

5.3.1 THz time-domain spectroscopy: native native conductivity.

THz time domain spectroscopy is a non-contact probe of conductivity, as absorption of THz radiation is directly related to how conductive material is. Fig. 5.2 shows THz pulses transmitted through a glass substrate alone (black curve) and through a ~16 nm

thick $Ti_3C_2T_x$ film on a glass substrate. It also shows the change in transmission through the $Ti_3C_2T_x$ film induced by the photoexcitation, which will be discussed later. Assuming that the absorption in the film is responsible for the observed attenuation of the transmitted THz radiation which is estimated to be ~ 7.7% at the peak of THz waveform, we calculate the average absorption coefficient for stacked $Ti_3C_2T_x$ in the 02. – 2.0 THz range to be 46 000 cm^{-1}, in excellent agreement with theoretically predicted 45 000-60 000 cm^{-1} range[186]. Conductivity of the sample in the frequency domain can be calculated using a thin film approximation from the relation $\frac{E_{sample}(\omega)}{E_{substrate}(\omega)} = \frac{n+1}{n+1+Z_0\sigma(\omega)}$, where $Z_0 = 377\ \Omega$ is the impedance of the free space, and n is the substrate refractive index in THz range[189]. For glass, n≈1.96 and can be treated as dispersionless in the frequency range of interest[194].

Resulting complex sheet conductivity spectrum is shown in Fig. 5.3 (a). It exhibits suppression of the real conductivity at low frequencies and negative imaginary conductivity. These features are characteristic of a system where free carriers motion on the mesoscopic length scales is constrained by potential barriers, such as often seen in nanocrystalline or granular systems. Conductivity in such systems can be well-described by a classical Drude-Smith model, a modification of the free carrier Drude conductivity that accounts for localization of the mobile carriers on the length scales commensurate with their mean free path[187], [192], [195]–[201].

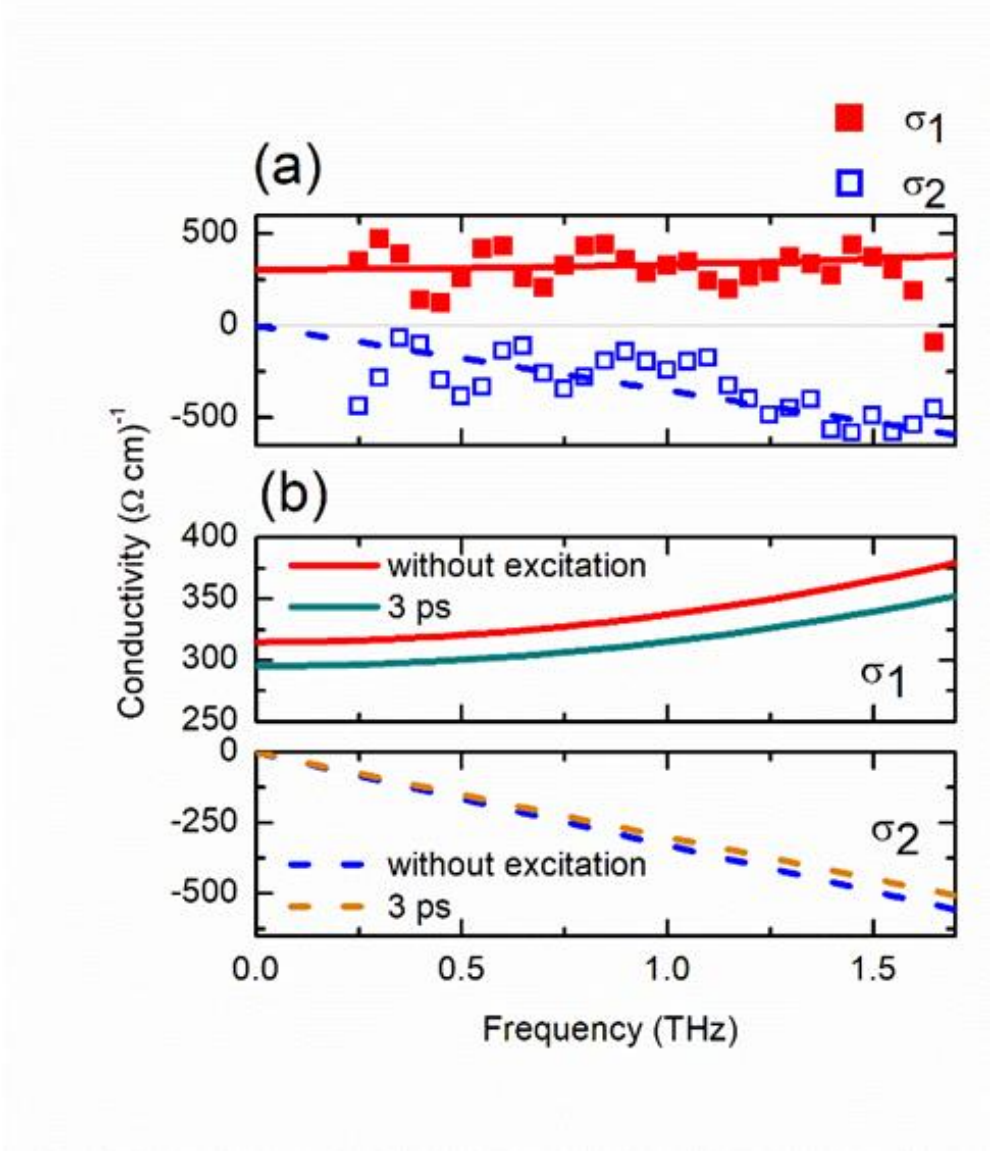
(a)
σ1
σ2
500
0
-500
(b)
400
350
300
250
without excitation
3 ps
σ1
0
-250
-500
σ2
without excitation
3 ps
0.0
0.5
1.0
1.5
Frequency (THz)
Conductivity (Ω cm)-1

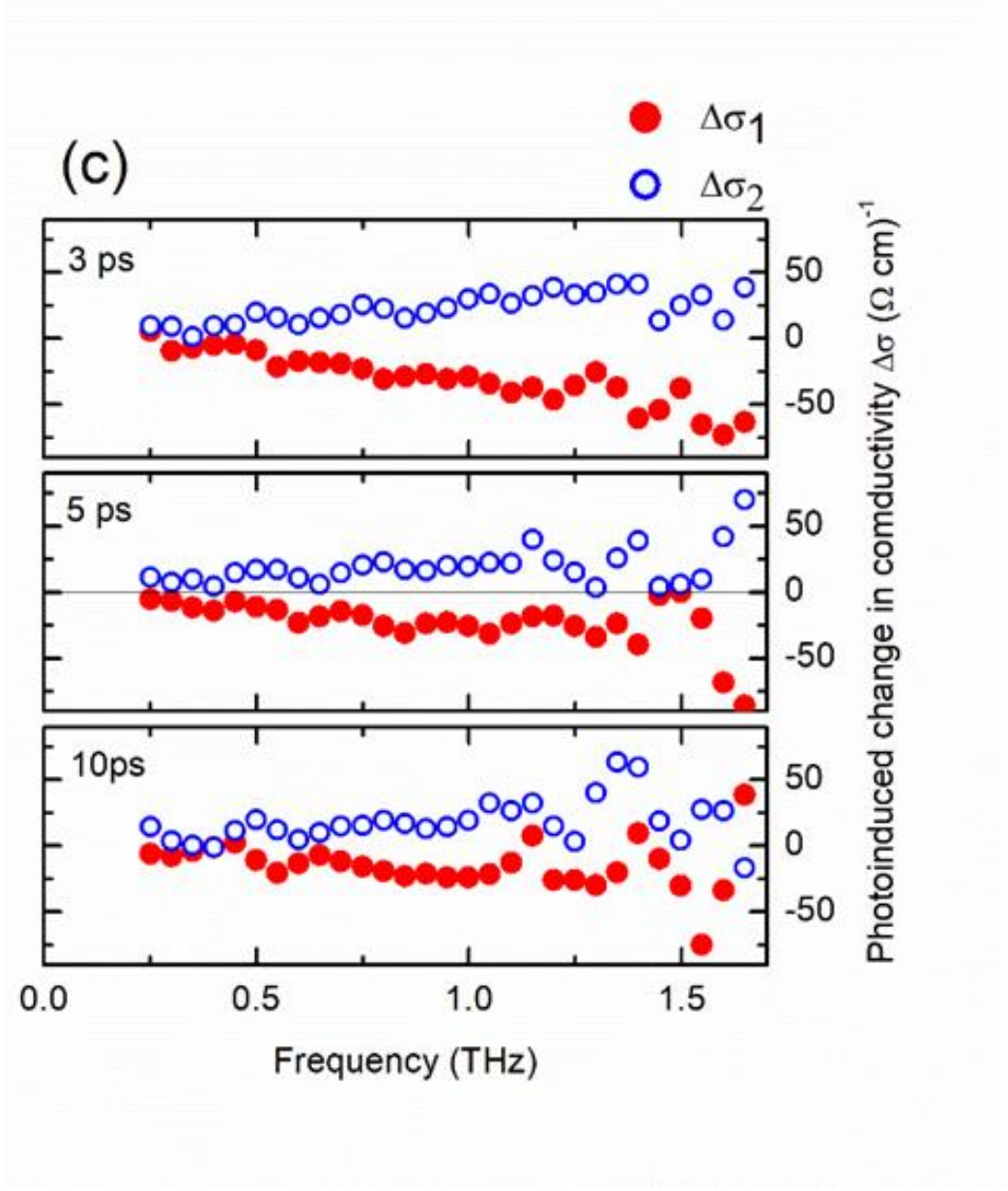

Figure 5.3. (a) Complex THz conductivity of the 16 nm $Ti_3C_2T_x$ film. Symbols represent experimental data extracted from THz waveforms in Fig. 5.2, and lines – global fit of the real and imaginary conductivity to the Drude-Smith model (solid red line –fit to σ_1, dashed blue line – fit to σ_1). (b) Drude-Smith fits to σ_1 and σ_2 without excitation (as

shown in (a)) and 3 ps following excitation with ~ 280 μJ/cm^2, 800 nm pulse. (c) Change in complex THz conductivity at different times after excitation.

In the Drude-Smith formalism, complex frequency-resolved conductivity is given as $\tilde{\sigma}(\omega) = \frac{\sigma_{DC}}{1-i\omega\tau_{DS}}\left(1 + \frac{c}{1-i\omega\tau_{DS}}\right)$. Here, $\sigma_{DC} = \sigma(0) = \frac{Ne^2\tau_{DS}}{m^*}$ is Drude weight, or the conductivity in DC limit, τ_{DS} is a phenomenological carrier scattering time which takes into account both the bulk scattering τ_{bulk} and characteristic time associated with grain boundary scattering $\tau_{boundary}$ as $\frac{1}{\tau_{DS}} = \frac{1}{\tau_{bulk}} + \frac{1}{\tau_{boundary}}$, N is the charge carrier density, and m^* is the carrier effective mass. Phenomenological *c*-parameter is a measure of carrier localization over the probed length scales. When *c*=0, the system is fully percolated and carriers free to move throughout the sample, as described by the Drude model. For *c=-1*, DC conductivity is suppressed as the carriers are localized over short distances. In Fig. 5.3(a), solid red symbols depict experimentally determined real conductivity, and open blue symbols – imaginary conductivity. Nearly dispersionless real conductivity at frequencies < 1.7 THz and a negative imaginary conductivity indicates a free carrier system with a short scattering time and localization over mesoscopic length scales due to the presence of the nanoplate boudaries that impede free carrier motion within the film. It should be noted that such complex conductivity spectra cannot be well-reproduced by the Lorentz conductivity model used to describe plasmon- and phonon-related effects, as frequency-dependent negative imaginary conductivity in the Lorentz model is accompanied by a significant dispersion in the real conductivity component[193]. Lines in

Fig. 5.3 (a) represent a global fit of real and imaginary conductivity to the Drude-Smith model with τ_{DS}=6±1 fs, and c=-0.97±0.03. Drude-Smith c-parameter that is close to -1 indicates that long-range conductivity in the film is strongly suppressed. However, even given this significant suppression of long-range transport, overall conductivity of the film is very high and extrapolates to ~ 300 $(\Omega\ \text{cm})^{-1}$ at ω=0 due to a very large, ~ $2\text{x}10^{21}$ cm^{-3} carrier density, calculated from the Drude-Smith fit to the THz conductivity using zone-center electron effective mass of 0.2845m_e[202]. Intrinsic carrier density determined from THz measurements is in reasonable agreement with the value determined from electrical measurements on individual nanosheets, 8±3 x 10^{21} cm^{-3}[203]. Underestimation of carrier density in THz measurements results from averaging over a large ~ 1.5 mm in diamater, area of the film that does not completely cover the surface (Fig. 5.1 (c)). We calculate intrinsic carrier mobility, or mobility of carriers over mesoscopic length scales within individual grains to be $\mu_{intrinsic} = \frac{e\tau_{DS}}{m^*}$ ≈34 cm^2/Vs. However, the long range mobility in this film is strongly suppressed, and can be estimated from the intrinsic mobility as $\mu_{long\ range} = \mu_{intrinsic}(1 + c)$. This calculation yields $\mu_{long\ range}$ ≈1 cm^2/Vs. It is in agreement with room temperature mobility within a singe nanosheet of 0.7±0.2 cm^2/Vs determined from electrical measurements[203] and supports our hypothesis that the free carrier motion is mainly impeded by the grain boundaries between different nanosheets within the thin film.

5.3.2 Optical pump - THz probe spectroscopy: non-equilibrium carrier dynamics

Many proposed applications for the MXenes involve their optical excitation. We have studies the effects of photoexcitation with ~ 100 fs, 800 nm pulses on THz

conductivity of the film. Linear optical absorbance of the film at 800 nm is ~ 15% based on UV-VIS measurements (Fig. 5.1 (d))[178]. At optical fluence of 280 μJ/cm^2, the absorbed photon flux is 17x10^{13} cm^{-2}. Resulting change in the THz pulse transmission at a given fixed time delay between the optical pump and THz probe was detected by modulating the optical pump beam using a chopper and recording the differential electric field ΔE. Resulting change in transmission of the THz probe pulse 3 ps after photoexcitation with ~ 280 μJ/cm^2 pulse compared to the transmission through the unpumped film are shown as a blue curve in Fig. 5.2, multiplied by 100 for clarity. While the change is small (<0.3%), it is clear that photoexcitation enhances THz transmission. Photoinduced transient changes in complex THz conductivity are summarized in Figure 5.3 (b,c). For a small differential change in transmission, complex differential change conductivity at a fixed pump-probe delay time was calculated as $\Delta\sigma(\omega) \approx -\frac{n+1}{Z_0}\frac{\Delta E(\omega)}{E(\omega)}$, where $E(\omega)$ is the electric field of the THz pulse transmitted through the unexcited film. Examples of the differential conductivity at 3 ps, 5 ps, and 10 ps after excitation with ~ 280 μJ/cm2 pulse are shown in 3 (c). Transient real photoconductivity is negatice at all these three time points, and in the entire sampled frequency range, demonstrating that photoexcitation suppresses conductivity of the film. This behavior is characteristic of metallic rather than semiconducting systems, and has been observed in graphene, thin metallic films and metallic RuO_2[9], [196], [199], [200], [204]–[208].

We analyze the temporal evolution of the complex conductivity following photoexcitation by fitting transient real ($\sigma_1(t)=\sigma_1+\Delta\sigma_1(t)$) and imaginary ($\sigma_2(t)=\sigma_2+\Delta\sigma_2(t)$) to the Drude-Smith model. Lines in Fig. 5.3 (b) represent the best fit to $\sigma_1(t)$ and $\sigma_2(t)$ at 3

ps following photoexcitation along with the best fit to THz conductivity in the unexcited film (Fig. 5.3 (a)). Like the intrinsic conductivity of unexcited sample described above, conductivity of the photoexcited sample is well-described by the Drude-Smith model with unchanged c-parameter $c=-0.97\pm0.03$, indicating that carriers in the remain localized by grain boundaries between different nanoplates even after photoexcitation. The observed change in carrier density is minimal, and can't be reliably determined within the error of our measurement. Intraband photoexcitation of metallic materials does not result in a free carrier density increase, but rather increases carrier scattering due to lattice heating as hot carriers couple to phonon modes[199]. Indeed, we find that the scattering time in the investigated time range 3-10 ps after optical excitation shows small but discernable decrease (Fig. 5.4), suggesting that increased carrier scattering in the major reason behind conductivity suppression. Improving the precision of both carrier density and the scattering rate would require THz measurements in the significantly broader spectral range.

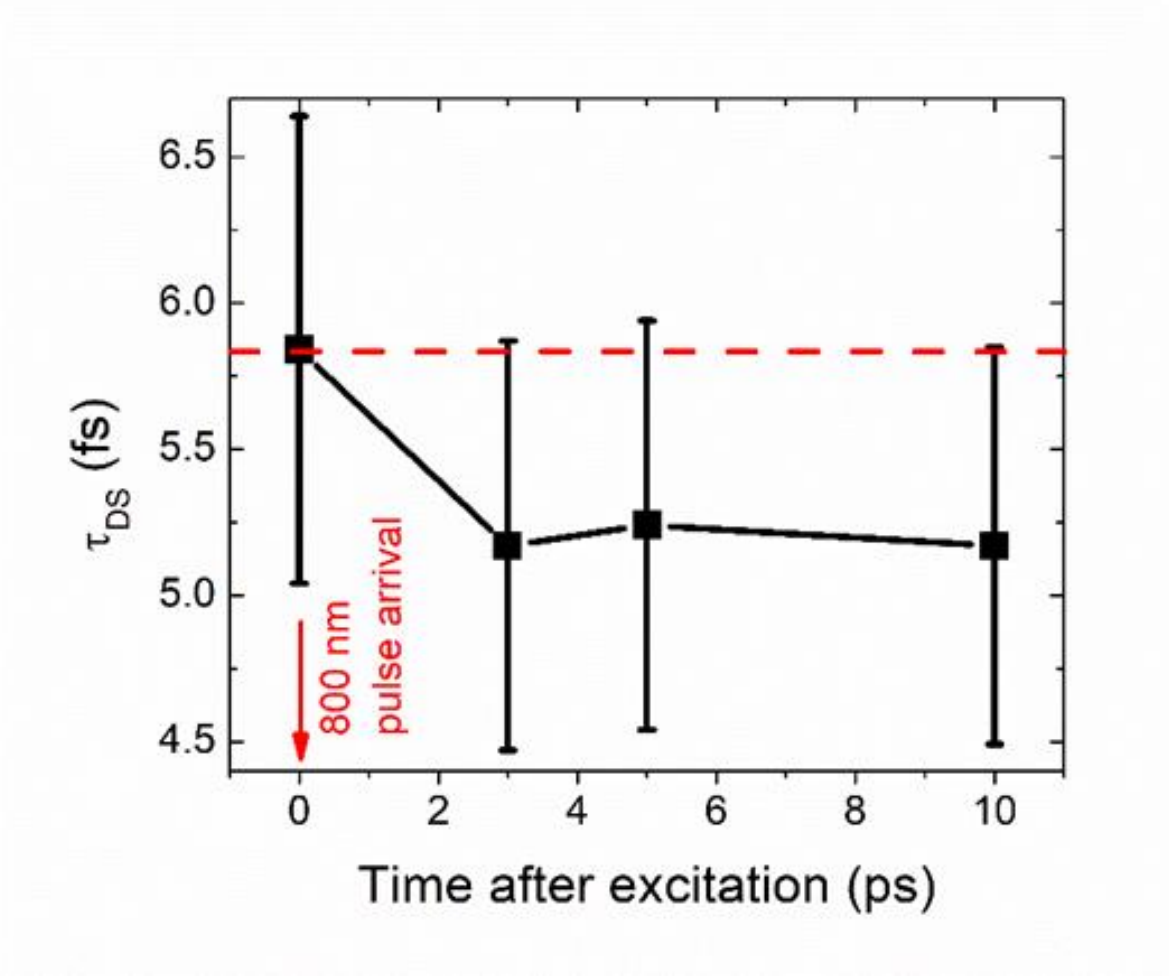

Figure 5.4. Change in the carrier scattering rate as a function of time following photoexcitation with ~ 280 μJ/cm^2, 800 nm pulse.

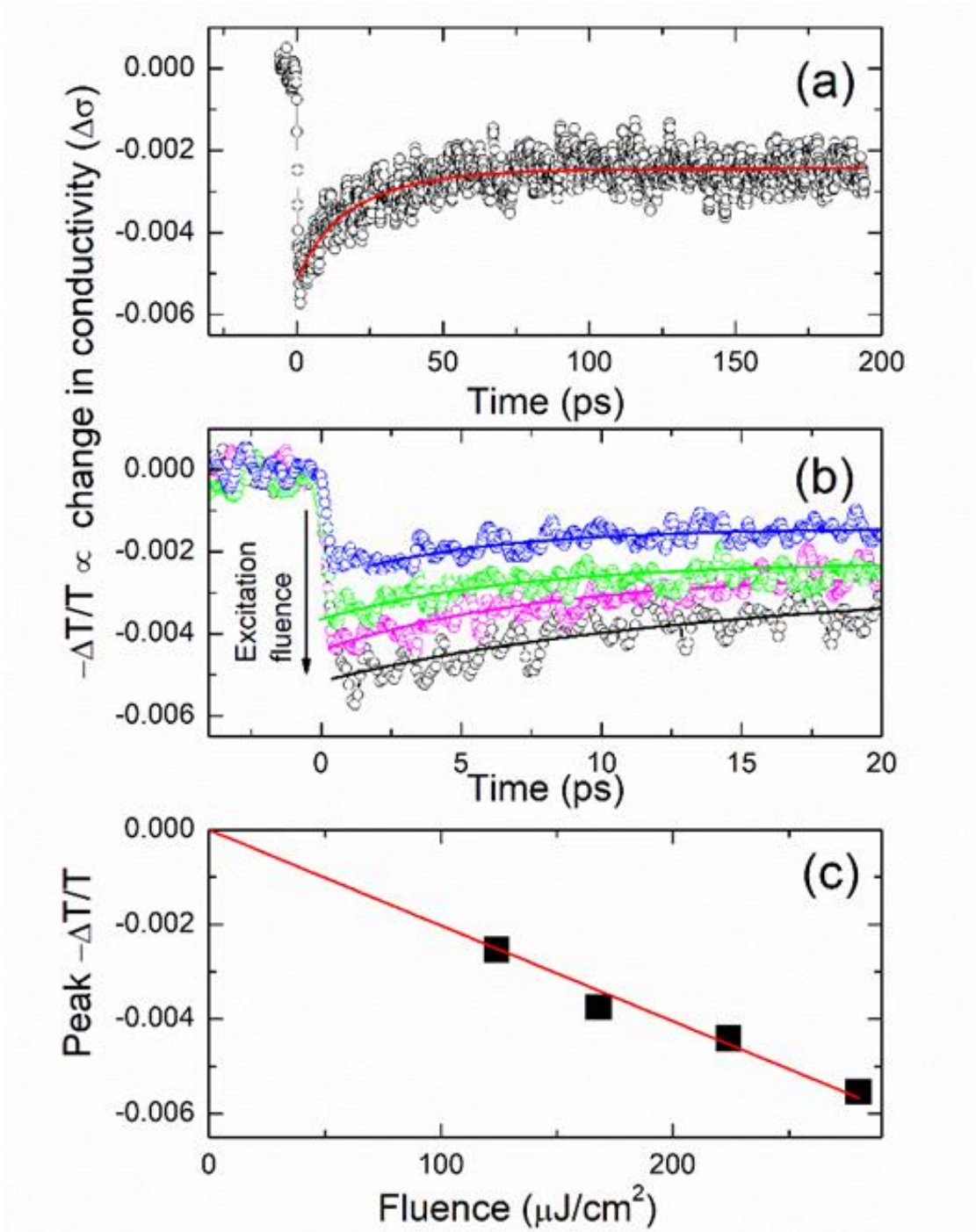

Figure 5.5. (a) Photoinduced change in the THz peak transmission as a function of time after photoexcitation with 280 μJ/cm^2, 800 nm pulse. Solid line shows the fit of THz transmission enhancement to a double-exponential decay. (b) Expanded view of transient peak THz transmission at different excitation fluence values from 120 μJ/cm^2 to 280 μJ/cm^2, and (c) the corresponding peak THz transmission change as a function of excitation fluence.

The dynamics of the observed conductivity suppression are examined in Fig. 5.5. By monitoring the transient change in the transmission of the THz pulse peak as a function of the pump-probe delay time, we have characterized the duration of the observed conductivity suppression. Instrument-limited rise time of conductivity suppression is followed by the long, slow decay that persists for 200 ps and possibly beyond, to the time scale not accessible in our experiments. Fig. 5.5 (a) shows transient enhancement of THz peak transmission following photoexcitation with ~ 280 μJ/cm^2 pulse. It can be fit to a bi-exponential decay (red solid line) with the fast component ~ 7±1 ps, a slower component ~ 22 ±2 ps, and a nearly constant offset that represents the long-lived component that we cannot reliably extract. This long decay of photoinduced conductivity suppression is similar to that observed in metallic (gold and chromium) thin films, and is significantly longer than in photoexcited graphene, which recovers within only a few picoseconds[9], [142], [196], [200], [205]–[208]. Decreasing excitation fluence to ~ 120 μJ/cm^2 linearly reduces the amplitude of the observed response but doesn't change the dynamics (Fig. 5.5(b,c)). In metallic materials with static density of free carriers, photoexcitation does not significantly increase free carrier density. Strong electron-phonon coupling facilitates rapid, over the sub-picosecond time scales, equilibration of hot free carrier population with the lattice, resulting in a transient increase of lattice temperature. Carrier scattering is increased at elevated lattice temperatures, and recovery of background conductivity over time scales of hundreds of picoseconds represents lattice cooling as heat is transferred to the substrate and laterally – to the unexcited portions of the film.

5.4 Conclusion

We have investigated equilibrium and non-equilibrium dynamics of charge carriers in $Ti_3C_2T_x$ nanoplates. We find that the nanoplates are metallic, with a high (~ $2x10^{21}$ cm^{-3}) intrinsic charge carrier density and relatively high (~34 cm^2/Vs) mobility of carriers within individual nanoplates. High carrier density gives rise to exceptionally large, ~ 46 000 cm^{-1} absorption in the THz range, putting $Ti_3C_2T_x$ forth as a potential THz detector material. Photoexcitation results in a transient reduction of conductivity, as hot carriers rapidly heat the lattice, and the elevated lattice temperature enhances carrier scattering. As the lattice cools over the time scales of hundreds of picoseconds by transferring heat to the substrate and to the unexcited portions of the film, conductivity of $Ti_3C_2T_x$ nanoplate film recovers. The possibility to suppress conductivity and enhance THz transmission in $Ti_3C_2T_x$ by photoexcitation makes this new 2D material an attractive candidate for THz modulation devices and variable electromagnetic shielding applications.

CHAPTER SIX

SUMMARY AND FUTURE WORK

In this thesis, we examined the excellent optical limiting properties of fullerenes. We also explored the SA properties of MXene ($Ti_3C_2T_x$) and successfully constructed an optical diode, which plays a key role in the realization and development of many photon technologies. Furthermore, novel nonlinear optical materials with an ultrafast response time, high resistance to bulk and surface laser damage, and low two-photon absorption were fabricated with a view to examine their optical nonlinearities. This thesis serves as a platform for advancing the design and fabrication of optoelectronic and photonic devices at nanoscale. For example, more than 60 possible members exisit in the MXene family of materials, and only 15 of them have been synthesized todate. They exhibit metallic to semiconducting behaviors, and their NLO properties are poorly understood.

REFERENCES

[1] Robert W. Boyd, *Nonlin Optics*, 3rd ed. .

[2] R. L. Sutherland, D. G. McLean, and S. Kirkpatrick, *Handbook of nonlinear optics*. Marcel Dekker, 2003.

[3] P. A. Franken, A. E. Hill, C. Peters, and G. Weinreich, "GENERATION OF OPTICAL HARMONICS," *Phys. Rev. Lett.*, vol. 7, no. 4, p. 118, 1961.

[4] G. B. Talapatra, N. Manickam, M. Samoc, M. E. Orczyk, S. P. Karna, and P. N. Prasad, "Nonlinear Optical Properties of the C, Molecule: Theoretical and Experimental Studies," *J. Phys. Chem*, vol. 96, pp. 5206–5208, 1992.

[5] S. R. Flom, R. G. S. Pong, F. J. Bartoli, and Z. H. Kafafi, "Resonant nonlinear optical response of the fullerenes C 60 and C 70," *Phys. Rev. B*, vol. 46, no. 23, pp. 15598–15601, Dec. 1992.

[6] Z. Jin, X. Sun, G. Xu, S. H. Goh, and W. Ji, "Nonlinear optical properties of some polymer/multi-walled carbon nanotube composites," *Chem. Phys. Lett.*, vol. 318, no. 6, pp. 505–510, Mar. 2000.

[7] J. Wang, Y. Chen, and W. J. Blau, "Carbon nanotubes and nanotube composites for nonlinear optical devices," *J. Mater. Chem.*, vol. 19, no. 40, p. 7425, Oct. 2009.

[8] Q. Bao *et al.*, "Monolayer graphene as a saturable absorber in a mode-locked laser," *Nano Res.*, vol. 4, no. 3, pp. 297–307, Mar. 2011.

[9] I. Ivanov, M. Bonn, Z. Mics, and D. Turchinovich, "Perspective on terahertz spectroscopy of graphene," *EPL (Europhysics Lett.*, vol. 111, no. 6, p. 67001, Sep. 2015.

[10] V. S. Muthukumar *et al.*, “Nonlinear Optical Absorption and Induced Thermal Scattering Studies in Organic and Inorganic Nanostructures,” in *Encyclopedia of Nanotechnology*, Dordrecht: Springer Netherlands, 2016, pp. 2954–2971.

[11] J. M. Pietryga *et al.*, “Spectroscopic and Device Aspects of Nanocrystal Quantum Dots,” *Chem. Rev.*, vol. 116, no. 18, pp. 10513–10622, Sep. 2016.

[12] G. Cao, *Nanostructures and Nanomaterials*. PUBLISHED BY IMPERIAL COLLEGE PRESS AND DISTRIBUTED BY WORLD SCIENTIFIC PUBLISHING CO., 2004.

[13] C. N. R. (Chintamani N. R. Rao, A. Müller, A. K. Cheetham, and John Wiley & Sons., *The chemistry of nanomaterials : synthesis, properties and applications in 2 volumes*. Wiley-VCH, 2004.

[14] J. T. Lue, “Physical Properties of Nanomaterials,” 2007.

[15] N. Bonini, R. Rao, A. M. Rao, N. Marzari, and J. Menéndez, “Lattice anharmonicity in low-dimensional carbon systems,” *Phys. status solidi*, vol. 245, no. 10, pp. 2149–2154, Oct. 2008.

[16] R. Rao, J. Menendez, C. D. Poweleit, and A. M. Rao, “Anharmonic Phonon Lifetimes in Carbon Nanotubes: Evidence for a One-Dimensional Phonon Decay Bottleneck,” *Phys. Rev. Lett.*, vol. 99, no. 4, p. 47403, Jul. 2007.

[17] B. R. Smith and S. S. Gambhir, “Nanomaterials for In Vivo Imaging,” *Chem. Rev.*, vol. 117, no. 3, pp. 901–986, Feb. 2017.

[18] Y.-X. Zhang and Y.-H. Wang, “Nonlinear optical properties of metal nanoparticles: a review.”

[19] P. C. Ray, “Size and Shape Dependent Second Order Nonlinear Optical Properties of Nanomaterials and Their Application in Biological and Chemical Sensing,” *Chem. Rev.*, vol. 110, no. 9, pp. 5332–5365, Sep. 2010.

[20] S. B. Lu *et al.*, “Broadband nonlinear optical response in multi-layer black phosphorus: an emerging infrared and mid-infrared optical material,” *Opt. Express*, vol. 23, no. 9, p. 11183, May 2015.

[21] A. K. Singh, D. Senapati, A. Neely, G. Kolawole, C. Hawker, and P. C. Ray, “Nonlinear optical properties of triangular silver nanomaterials,” *Chem. Phys. Lett.*, vol. 481, no. 1–3, pp. 94–98, Oct. 2009.

[22] R. Krischek *et al.*, “Ultraviolet enhancement cavity for ultrafast nonlinear optics and high-rate multiphoton entanglement experiments,” *Nat. Photonics*, vol. 4, no. 3, p. 170, Jan. 2010.

[23] K. Y. Song, M. G. Herrez, and L. Thvenaz, “Observation of pulse delaying and advancement in optical fibers using stimulated Brillouin scattering,” *Opt. Express*, vol. 13, no. 1, p. 82, Jan. 2005.

[24] C. W. Freudiger *et al.*, “Label-free biomedical imaging with high sensitivity by stimulated Raman scattering microscopy.,” *Science*, vol. 322, no. 5909, pp. 1857–61, Dec. 2008.

[25] J. B. Snow, S.-X. Qian, and R. K. Chang, “Stimulated Raman scattering from individual water and ethanol droplets at morphology-dependent resonances,” *Opt. Lett.*, vol. 10, no. 1, p. 37, Jan. 1985.

[26] B. B. Ivanova and M. Spiteller, “Noncentrosymmetric Crystals with Marked

Nonlinear Optical Properties," *J. Phys. Chem. A,* vol. 114, no. 15, pp. 5099–5103, Apr. 2010.

[27] A. Yariv, "The Application of Time Evolution Operators and Feynman Diagrams to Nonlinear Optics," *IEEE J. Quantum Electron.*, no. 12, 1977.

[28] V. Nathan, S. S. Mitra, and A. H. Guenther, "Review of multiphoton absorption in crystalline solids," *J. Opt. Soc. Am. B,* vol. 2, no. 2, p. 294, Feb. 1985.

[29] Richard A. Farrer, Francis L. Butterfield, † and Vincent W. Chen, and ‡ John T. Fourkas*, "Highly Efficient Multiphoton-Absorption-Induced Luminescence from Gold Nanoparticles," 2005.

[30] W. R. Zipfel, R. M. Williams, and W. W. Webb, "Nonlinear magic: multiphoton microscopy in the biosciences," *Nat. Biotechnol.*, vol. 21, no. 11, pp. 1369–1377, Nov. 2003.

[31] A. H. . Castro Neto, N. M. R. . Peres, K. S. . Novoselov, A. K. . Geim, and F. Guinea, "The electronic properties of graphene," *Rev. Mod. Phys.*, vol. 81, no. 1, pp. 109–162, 2009.

[32] Q. Bao *et al.*, "Atomic-Layer Graphene as a Saturable Absorber for Ultrafast Pulsed Lasers," *Adv. Funct. Mater.*, vol. 19, no. 19, pp. 3077–3083, Oct. 2009.

[33] M. Sheik-Bahae, A. A. Said, T.-H. Wei, D. J. Hagan, and E. W. Van Stryland, "Sensitive Measurement of Optical Nonlinearities Using a Single Beam," *IEEE J. Quantum Electron.*, vol. 26, no. 4, 1990.

[34] A. Biberman and K. Bergman, "Optical interconnection networks for high-performance computing systems.," *Rep. Prog. Phys.*, vol. 75, no. 4, p. 46402,

2012.

[35] A. Aspuru-Guzik and P. Walther, “Photonic quantum simulators,” *Nature Physics*, vol. 8, no. 4. pp. 285–291, 2012.

[36] D. Woods and T. J. Naughton, “Optical computing: Photonic neural networks,” *Nature Physics*, vol. 8, no. 4. pp. 257–259, 2012.

[37] B. Anand *et al.*, “Optical Diode Action from Axially Asymmetric Nonlinearity in an All-Carbon Solid-State Device,” *Nano Lett.*, vol. 13, no. 12, pp. 5771–5776, Dec. 2013.

[38] L. W. Tutt and T. F. Boggess, “A review of optical limiting mechanisms and devices using organics, fullerenes, semiconductors and other materials,” *Prog. Quantum Electron.*, vol. 17, no. 4, pp. 299–338, 1993.

[39] A. Kost, L. Tutt, M. B. Klein, T. K. Dougherty, and W. E. Elias, “Optical limiting with C(60) in polymethyl methacrylate.,” *Opt. Lett.*, vol. 18, no. 5, pp. 334–336, 1993.

[40] M. Yoda, *Encyclopedia of Nanotechnology*. 2012.

[41] H. Pan, W. Chen, Y. P. Feng, W. Ji, and J. Lin, “Optical limiting properties of metal nanowires,” *Appl. Phys. Lett.*, vol. 88, no. 22, pp. 17–20, 2006.

[42] V. S. Muthukumar *et al.*, “Optical limiting properties of CdS nanowires,” *Opt. Commun.*, vol. 283, no. 20, pp. 4104–4107, Oct. 2010.

[43] W. Jia, E. P. Douglas, F. Guo, and W. Sun, “Optical limiting of semiconductor nanoparticles for nanosecond laser pulses,” *Appl. Phys. Lett.*, vol. 85, no. 26, pp. 6326–6328, 2004.

[44] P. Pradhan *et al.*, “Optical limiting and nonlinear optical properties of gold-decorated graphene nanocomposites,” *Opt. Mater. (Amst).*, vol. 39, pp. 182–187, Jan. 2015.

[45] Y. Sun, J. E. Riggs, and B. Liu, “Optical Limiting Properties of [60]Fullerene Derivatives,” *Chem. Mater.*, vol. 9, no. 5, pp. 1268–1272, 1997.

[46] Y.-P. Sun and J. E. Riggs, “Organic and inorganic optical limiting materials. From fullerenes to nanoparticles,” *International Reviews in Physical Chemistry*, vol. 18, no. 1. pp. 43–90, 1999.

[47] J. Wang and W. J. Blau, “Inorganic and hybrid nanostructures for optical limiting,” *Journal of Optics A: Pure and Applied Optics*, vol. 11, no. 2. p. 24001, 2009.

[48] D. J. Payne *et al.*, “Comparative study of laser damage threshold energies in the artificial retina.,” *J. Biomed. Opt.*, vol. 4, no. 3, pp. 337–44, 1999.

[49] R. Brinkmann, G. Hüttmann, J. Rögener, J. Roider, R. Birngruber, and C. P. Lin, “Origin of retinal pigment epithelium cell damage by pulsed laser irradiance in the nanosecond to microsecond time regimen,” *Lasers Surg. Med.*, vol. 27, no. 5, pp. 451–464, 2000.

[50] N. MacKiewicz *et al.*, “Fullerene-functionalized carbon nanotubes as improved optical limiting devices,” *Carbon N. Y.*, vol. 49, no. 12, pp. 3998–4003, 2011.

[51] K. M. Nashold and D. P. Walter, “Investigations of optical limiting mechanisms in carbon particle suspensions and fullerene solutions,” *Journal of the Optical Society of America B*, vol. 12, no. 7. p. 1228, 1995.

[52] J. E. Riggs and Y.-P. Sun, “Optical limiting properties of mono- and multiple-functionalized fullerene derivatives,” *J. Chem. Phys.*, vol. 112, no. 9, pp. 4221–4230, 2000.

[53] C. Liu *et al.*, “Optical limiting property of molybdenum complex of fullerene C70,” *Opt. Commun.*, vol. 184, no. 1, pp. 309–313, 2000.

[54] A. W. Allaf and M. D. Zidan, “Optical limiting behavior of new fullerene derivatives,” *Opt. Lasers Eng.*, vol. 43, no. 1, pp. 57–62, 2005.

[55] A. R. Kost, J. E. Jensen, R. O. Loufty, and J. C. Wither, “Optical limiting with higher fullerenes,” *Appl. Phys. B Lasers Opt.*, vol. 80, no. 3, pp. 281–283, 2005.

[56] S. S. Harilal, C. V. Bindhu, V. P. N. Nampoori, and C. P. G. Vallabhan, “Optical limiting and thermal lensing studies in C[sub 60],” *J. Appl. Phys.*, vol. 86, no. 3, p. 1388, 1999.

[57] Q. Chang *et al.*, “Enhanced optical limiting properties in suspensions of CdO nanowires,” *Opt. Commun.*, vol. 274, no. 1, pp. 201–205, 2007.

[58] B. Anand *et al.*, “Nonlinear optical properties of boron doped single-walled carbon nanotubes,” *Nanoscale*, vol. 5, no. 16, p. 7271, 2013.

[59] R. Podila *et al.*, “Evidence for surface states in pristine and Co-doped ZnO nanostructures: magnetization and nonlinear optical studies.,” *Nanotechnology*, vol. 22, no. 9, p. 95703, 2011.

[60] B. Karthikeyan, C. S. S. Sandeep, T. Pandiyarajan, P. Venkatesan, and R. Philip, “Optical and nonlinear absorption properties of Na doped ZnO nanoparticle dispersions,” *Appl. Phys. Lett.*, vol. 95, no. 2, 2009.

[61] J. Zhao, X. Chen, and J. R. H. Xie, “Optical properties and photonic devices of doped carbon nanotubes,” *Analytica Chimica Acta*, vol. 568, no. 1–2. pp. 161–170, 2006.

[62] C. S. Kumar, *Mixed metal nanomaterials*, 3rd ed. John Wiley & SOns, 2009.

[63] C. M. Aguirre, C. E. Moran, J. F. Young, and N. J. Halas, “Laser-induced reshaping of metallodielectric nanoshells under femtosecond and nanosecond plasmon resonant illumination,” *J. Phys. Chem. B*, vol. 108, no. 22, pp. 7040–7045, 2004.

[64] C. D. Brooks and F. Di Teodoro, “High peak power operation and harmonic generation of a single-polarization, Yb-doped photonic crystal fiber amplifier,” *Opt. Commun.*, vol. 280, no. 2, pp. 424–430, 2007.

[65] S. Desmoulins and F. Di Teodoro, “High-gain Er-doped fiber amplifier generating eye-safe MW peak-power, mJ-energy pulses.,” *Opt. Express*, vol. 16, no. 4, pp. 2431–2437, 2008.

[66] M.-Y. Cheng, Y.-C. Chang, A. Galvanauskas, P. Mamidipudi, R. Changkakoti, and P. Gatchell, “High-energy and high-peak-power nanosecond pulse generation with beam quality control in 200-microm core highly multimode Yb-doped fiber amplifiers.,” *Opt. Lett.*, vol. 30, no. 4, pp. 358–360, 2005.

[67] A. V. Smith, B. T. Do, G. R. Hadley, and R. L. Farrow, “Optical damage limits to pulse energy from fibers,” *IEEE J. Sel. Top. Quantum Electron.*, vol. 15, no. 1, pp. 153–158, 2009.

[68] J. R. Pinzón *et al.*, “Metal nitride cluster fullerene M3N@C80 (M = Y, Sc) based

dyads: Synthesis, and electrochemical, theoretical and photophysical studies," *Chem. - A Eur. J.*, vol. 15, no. 4, pp. 864–877, 2009.

[69] "Sensitive Measurement of Optical Nonlinearities Using a Single Beam ." [Online]. Available: http://www.optics.unm.edu/sbahae/publications/z-scan-IEEE-JQE90.pdf. [Accessed: 01-Dec-2015].

[70] S. Couris, E. Koudoumas, A. A. Ruth, and S. Leach, "in toluene solution," *Journal of Physics B: Atomic, Molecular and Optical Physics*, vol. 28, no. 20. pp. 4537–4554, 1999.

[71] S. R. Mishra, H. S. Rawat, and S. C. Mehendale, "Reverse saturable absorption and optical limiting in C 60 solution in the near-infrared," *Appl. Phys. Lett.*, vol. 71, no. 1, pp. 46–48, 1997.

[72] M. S. Dresselhaus, G. Dresselhaus, A. M. Rao, and P. C. Eklund, "Optical properties of C60 and related materials," *Synth. Met.*, vol. 78, no. 3, pp. 313–325, 1996.

[73] S. Fleischer *et al.*, "Ultrafast dynamics of superconducting K3C60 and Rb3C60," *Physical Review B*, vol. 62, no. 2. pp. 1366–1378, 2000.

[74] P. W. Stephens *et al.*, "Structure of single-phase superconducting K3C60," *Nature*, vol. 351, no. 6328. pp. 632–634, 1991.

[75] M. Krause, H. Kuzmany, P. Georgi, L. Dunsch, K. Vietze, and G. Seifert, "Structure and stability of endohedral fullerene Sc3N@C80: A Raman, infrared, and theoretical analysis," *J. Chem. Phys.*, vol. 115, no. 14, pp. 6596–6605, 2001.

[76] J. R. Pinzón *et al.*, "Photoinduced Charge Transfer and Electrochemical Properties

of Triphenylamine Ih-Sc3 N@C80 Donor-Acceptor Conjugates," *J. Am. Chem. Soc.*, vol. 131, no. 22, pp. 7727–7734, 2009.

[77] D. S. Chemla and D. A. B. Miller, "Room-temperature excitonic nonlinear-optical effects in semiconductor quantum-well structures," *Journal of the Optical Society of America B*, vol. 2, no. 7. p. 1155, 1985.

[78] P. M. Felker, V. Vlček, I. Hietanen, S. FitzGerald, D. Neuhauser, and Z. Bačić, "Explaining the symmetry breaking observed in the endofullerenes $H_2@C_{60}$, $HF@C_{60}$, and $H_2O@C_{60}$," *Phys. Chem. Chem. Phys.*, vol. 19, no. 46, pp. 31274–31283, Nov. 2017.

[79] J. Wang *et al.*, "Recent advancements in boron nitride nanotubes," *Nanoscale*, vol. 2, no. 10, p. 2028, Oct. 2010.

[80] R. V. Gorbachev *et al.*, "Hunting for monolayer boron nitride: Optical and raman signatures," *Small*, vol. 7, no. 4, pp. 465–468, 2011.

[81] L. Lin, Y. Xu, S. Zhang, I. M. Ross, A. C. M. Ong, and D. a. Allwood, "Fabrication and luminescence of monolayered boron nitride quantum dots," *Small*, vol. 10, no. 1, pp. 60–65, 2014.

[82] A. L. Tiano *et al.*, "Boron Nitride Nanotube: Synthesis and Applications," *SPIE Conf.*, 2014.

[83] L. Zhibo, Z. Xiaoliang, Y. Xiaoqing, C. Yongsheng, and T. Jianguo, "Nonlinear optical properties of graphene-based materials," *Spec. ISSUE Graphene August*, vol. 5723, pp. 2971–2982, 2012.

[84] K. Wang *et al.*, "Broadband Ultrafast Nonlinear Absorption and Nonlinear

Refraction of Layered Molybdenum Dichalcogenide Semiconductors," *Nanoscale*, vol. 6, pp. 10530–10535, 2014.

[85] B. Anand *et al.*, "Optical diode action from axially asymmetric nonlinearity in an all-carbon solid-state device," *Nano Lett.*, vol. 13, no. 12, pp. 5771–5776, 2013.

[86] H. Zhang *et al.*, "Molybdenum disulfide (MoS 2) as a broadband saturable absorber for ultra-fast photonics," *Opt. Express*, vol. 22, no. 6, p. 7249, 2014.

[87] Z. Guo *et al.*, "From Black Phosphorus to Phosphorene: Basic Solvent Exfoliation, Evolution of Raman Scattering, and Applications to Ultrafast Photonics," *Adv. Funct. Mater.*, vol. 25, no. 45, pp. 6996–7002, Dec. 2015.

[88] Y. Dong, D. Saini, L. A. Echegoyen, and R. Podila, "Passive optical switches based on endohedral fullerenes," *Opt. Mater. (Amst).*, vol. 53, pp. 14–18, 2016.

[89] B. Zhu, X. Chen, and X. Cui, "Exciton Binding Energy of Monolayer WS 2," *Sci. Rep.*, vol. 5, 2014.

[90] R. W. Newson, J. Dean, B. Schmidt, and H. M. Driel, Van, "Ultrafast carrier kinetics in exfoliated graphene and thin graphite films," *Opt. Express*, vol. 17, no. 4, p. 2326, 2009.

[91] Q. Bao *et al.*, "Monolayer graphene as a saturable absorber in a mode-locked laser," *Nano Res.*, vol. 4, no. 3, pp. 297–307, Mar. 2011.

[92] A. H. Castro Neto, N. M. R. Peres, K. S. Novoselov, and A. K. Geim, "The electronic properties of graphene," *Reviews of Modern Physics*, vol. 81, no. 1. pp. 109–162, 2009.

[93] H. Zhang *et al.*, "Molybdenum disulfide (MoS_2) as a broadband saturable

absorber for ultra-fast photonics," *Opt. Express*, vol. 22, no. 6, p. 7249, Mar. 2014.

[94] H. Zhang *et al.*, "Z-scan measurement of the nonlinear refractive index of graphene," *Opt. Lett.*, vol. 37, no. 11, p. 1856, Jun. 2012.

[95] J. M. P. Almeida, D. S. Da Silva, L. R. P. Kassab, S. C. Zilio, C. R. Mendonça, and L. De Boni, "Universidade de São Paulo Ultrafast third-order optical nonlinearities of heavy metal oxide glasses containing gold nanoparticles Ultrafast third-order optical nonlinearities of heavy metal oxide glasses containing gold nanoparticles," *Opt. Mater. (Amst).*, vol. 36, no. 4, pp. 829–832, 2014.

[96] C. P. Singh, K. S. Bindra, G. M. Bhalerao, and S. M. Oak, "Investigation of optical limiting in iron oxide nanoparticles," *Opt. Express*, vol. 16, no. 12, p. 8440, 2008.

[97] A. Acharya, R. Behera, and G. S. Roy, "Non-linear characteristic of copper oxide (CuO) through Z-scan technique," *Am. J. Phys. Educ*, vol. 6, no. 3, 2012.

[98] W. C. Hurlbut, Y.-S. Lee, K. L. Vodopyanov, P. S. Kuo, and M. M. Fejer, "Multiphoton absorption and nonlinear refraction of GaAs in the mid-infrared," *Opt. Lett.*, vol. 32, no. 6, p. 668, 2007.

[99] P. Kumbhakar *et al.*, "Nonlinear Optical Properties and Temperature-Dependent UV-Vis Absorption and Photoluminescence Emission in 2D Hexagonal Boron Nitride Nanosheets," *Adv. Opt. Mater.*, vol. 3, no. 6, pp. 828–835, Jun. 2015.

[100] S. Webster *et al.*, "Linear and Nonlinear Spectroscopy of a Porphyrin−Squaraine−Porphyrin Conjugated System," *J. Phys. Chem. B*, vol. 113, no. 45, pp. 14854–14867, Nov. 2009.

[101] Q. Zheng, H. Zhu, S.-C. Chen, C. Tang, E. Ma, and X. Chen, "Frequency-

upconverted stimulated emission by simultaneous five-photon absorption," 2013.

[102] W. Chen *et al.*, "ARTICLE Giant five-photon absorption from multidimensional core-shell halide perovskite colloidal nanocrystals," 2017.

[103] D. H. Friese, R. Bast, and K. Ruud, "Five-Photon Absorption and Selective Enhancement of Multiphoton Absorption Processes.," *ACS photonics*, vol. 2, no. 5, pp. 572–577, May 2015.

[104] S. Kawata, H.-B. Sun, T. Tanaka, and K. Takada, "Finer features for functional microdevices," *Nature*, vol. 412, no. 6848, pp. 697–698, Aug. 2001.

[105] G. Mainfray and G. Manus, "Multiphoton ionization of atoms," *Reports Prog. Phys.*, vol. 54, no. 10, pp. 1333–1372, Oct. 1991.

[106] H. Zhang *et al.*, "Z-scan measurement of the nonlinear refractive index of graphene," *Opt. Lett.*, vol. 37, no. 11, p. 1856, Jun. 2012.

[107] E. Van Stryland and M. Sheik-Bahae, "Z-scan measurements of optical nonlinearities," *Charact. Tech. Tabul. Org. Nonlinear Mater.*, no. 3, pp. 655–692, 1998.

[108] T. Woldu, B. Raneesh, P. Sreekanth, M. V. Ramana Reddy, R. Philip, and N. Kalarikkal, "Size dependent nonlinear optical absorption in BaTiO3 nanoparticles," *Chem. Phys. Lett.*, vol. 625, pp. 58–63, Apr. 2015.

[109] R. Philip, G. R. Kumar, N. Sandhyarani, and T. Pradeep, "Picosecond optical nonlinearity in monolayer-protected gold, silver, and gold-silver alloy nanoclusters," *Phys. Rev. B*, vol. 62, no. 19, pp. 13160–13166, Nov. 2000.

[110] B. Anand *et al.*, "Dopant-configuration controlled carrier scattering in graphene,"

RSC Adv., vol. 5, no. 73, pp. 59556–59563, 2015.

[111] G. Cassabois, P. Valvin, and B. Gil, "Hexagonal boron nitride is an indirect bandgap semiconductor," *Nat. Photonics*, vol. 10, no. 4, pp. 262–267, 2016.

[112] B. Anand *et al.*, "Optical Diode Action from Axially Asymmetric Nonlinearity in an All-Carbon Solid-State Device," *Nano Lett.*, vol. 13, no. 12, pp. 5771–5776, Dec. 2013.

[113] T.-H. Wei, T.-H. Huangz, S. Yangô, D. Liuy, J.-K. Huy, and C.-W. Cheny, "Z-scan study of optical nonlinearity in C 60 -toluene solution."

[114] M. D. Zidan, A. W. Allaf, A. Allahham, and A. AL-Zier, "Z-scan measurements of single walled carbon nanotube doped acetylenedicarboxylic acid polymer under CW laser," *Opt. Laser Technol.*, vol. 80, pp. 72–76, Jun. 2016.

[115] A. Yamanaka and S. Okada, "Energetics and Electronic Structure of h-BN Nanoflakes," *Nat. Publ. Gr.*, 2016.

[116] M. ?M. Monshi, S. M. Aghaei, and I. Calizo, "Edge functionalized germanene nanoribbons: impact on electronic and magnetic properties," *RSC Adv.*, vol. 7, no. 31, pp. 18900–18908, Mar. 2017.

[117] C. Attaccalite, M. Bockstedte, A. Marini, A. Rubio, and L. Wirtz, "Coupling of excitons and defect states in boron-nitride nanostructures," *Phys. Rev. B*, vol. 83, 2011.

[118] C. Huang *et al.*, "Carbon-doped BN nanosheets for metal-free photoredox catalysis.," *Nat. Commun.*, vol. 6, p. 7698, 2015.

[119] L. A. Silva, S. C. Guerini, V. Lemos, and J. M. Filho, "Electronic and Structural

Properties of Oxygen-Doped BN Nanotubes," *IEEE Trans. Nanotechnol.*, vol. 5, no. 5, pp. 517–522, Sep. 2006.

[120] R. S. Singh, "Influence of oxygen impurity on electronic properties of carbon and boron nitride nanotubes: A comparative study," *AIP Adv.*, vol. 5, no. 11, p. 117150, Nov. 2015.

[121] Q. Weng, X. Wang, X. Wang, Y. Bando, and D. Golberg, "Functionalized hexagonal boron nitride nanomaterials: emerging properties and applications," *Chem. Soc. Rev.*, vol. 45, no. 14, pp. 3989–4012, Jul. 2016.

[122] F. Ma *et al.*, "'Thermal substitution' for preparing ternary BCN nanosheets with enhanced and controllable nonlinear optical performance," *J. Mater. Chem. C*, vol. 5, no. 10, pp. 2559–2565, Mar. 2017.

[123] W.-Q. Han, H.-G. Yu, and Z. Liu, "Convert graphene sheets to boron nitride and boron nitride?carbon sheets via a carbon-substitution reaction," *Appl. Phys. Lett.*, vol. 98, no. 20, p. 203112, May 2011.

[124] C. Attaccalite, M. Bockstedte, A. Marini, A. Rubio, and L. Wirtz, "Coupling of excitons and defect states in boron-nitride nanostructures," *Phys. Rev. B*, vol. 83, no. 14, p. 144115, Apr. 2011.

[125] P. Beiss, R. Ruthardt, and H. Warlimont, Eds., *Powder Metallurgy Data. Refractory, Hard and Intermetallic Materials*, vol. 2A2. Berlin/Heidelberg: Springer-Verlag, 2002.

[126] W. Lei *et al.*, "Oxygen-doped boron nitride nanosheets with excellent performance in hydrogen storage," *Nano Energy*, vol. 6, pp. 219–224, May 2014.

[127] Z. Luo *et al.*, “Nonlinear optical absorption of few-layer molybdenum diselenide (MoSe_2) for passively mode-locked soliton fiber laser [Invited],” *Photonics Res.*, vol. 3, no. 3, p. A79, Jun. 2015.

[128] J. S. Ponraj *et al.*, “Photonics and optoelectronics of two-dimensional materials beyond graphene,” *Nanotechnology*, vol. 27, no. 46, p. 462001, Nov. 2016.

[129] S. Das, R. Gulotty, A. V. Sumant, and A. Roelofs, “All Two-Dimensional, Flexible, Transparent, and Thinnest Thin Film Transistor,” *Nano Lett.*, vol. 14, no. 5, pp. 2861–2866, May 2014.

[130] G. Xing, H. Guo, X. Zhang, T. C. Sum, and C. H. A. Huan, “The Physics of ultrafast saturable absorption in graphene,” *Opt. Express*, vol. 18, no. 5, p. 4564, Mar. 2010.

[131] X. He *et al.*, “Nonlinear saturable absorption of nanoscaled Bi2Te3/PMMA composite film,” *Phys. E Low-Dimensional Syst. Nanostructures*, vol. 81, pp. 71–76, 2016.

[132] P. Tang *et al.*, “Topological insulator: Bi2Te3 saturable absorber for the passive Q-switching operation of an in-band pumped 1645-nm Er:YAG ceramic laser,” *IEEE Photonics J.*, vol. 5, no. 2, 2013.

[133] Z. Wang, H. Mu, J. Yuan, C. Zhao, Q. Bao, and H. Zhang, “Graphene-Bi2Te3 heterostructure as broadband saturable absorber for ultra-short pulse generation in Er-doped and Yb-doped fiber lasers,” *IEEE J. Sel. Top. Quantum Electron.*, vol. 23, no. 1, 2017.

[134] C. Zhao *et al.*, “Ultra-short pulse generation by a topological insulator based

saturable absorber," *Appl. Phys. Lett.*, vol. 101, no. 21, 2012.

[135] R. Khazaeizhad, S. H. Kassani, H. Jeong, D.-I. Yeom, and K. Oh, "Mode-locking of Er-doped fiber laser using a multilayer MoS2 thin film as a saturable absorber in both anomalous and normal dispersion regimes.," *Opt. Express*, vol. 22, no. 19, pp. 23732–42, 2014.

[136] K. Wang *et al.*, "Ultrafast saturable absorption of two dimensional MoS2 nanosheets," *ACS Nano*, vol. 7, no. 10, p. 9260, 2013.

[137] R. I. Woodward *et al.*, "Few-layer MoS2 saturable absorbers for short-pulse laser technology: current status and future perspectives Invited," *Photonics Res.*, vol. 3, no. 2, pp. A30–A42, 2015.

[138] Q. Ouyang, H. Yu, H. Wu, Z. Lei, L. Qi, and Y. Chen, "Graphene/MoS2 organic glasses: Fabrication and enhanced reverse saturable absorption properties," *Opt. Mater. (Amst).*, vol. 35, no. 12, pp. 2352–2356, 2013.

[139] K. Wang *et al.*, "Ultrafast saturable absorption of two-dimensional MoS2 nanosheets," *ACS Nano*, vol. 7, no. 10, pp. 9260–9267, 2013.

[140] S. Wang *et al.*, "Broadband few-layer MoS2 saturable absorbers," *Adv. Mater.*, vol. 26, no. 21, pp. 3538–3544, 2014.

[141] C. Lee and T. Schibli, "Ultra-short optical pulse generation with single-layer graphene," *J. Nonlinear Opt. Phys. Mater.*, p. 6, 2010.

[142] B. Anand *et al.*, "Dopant-configuration controlled carrier scattering in graphene," *RSC Adv.*, vol. 5, no. 73, pp. 59556–59563, 2015.

[143] O. Okhotnikov, A. Grudinin, and M. Pessa, "Ultra-fast fibre laser systems based

on SESAM technology: New horizons and applications," *New J. Phys.*, vol. 6, pp. 1–22, 2004.

[144] C. J. Saraceno *et al.*, "SESAM designs for ultrafast lasers," in *SPIE 8601, Fiber Lasers X: Technology, Systems, and Applications, 86010Q*, 2013, vol. 8601, p. 86010Q.

[145] I. T. Sorokina, E. Sorokin, and T. J. Carrig, "Femtosecond pulse generation from a SESAM mode-locked Cr:ZnSe laser," in *Conference on Lasers and Electro-Optics and 2006 Quantum Electronics and Laser Science Conference, CLEO/QELS 2006*, 2006.

[146] J. Zhang and M. Ni, "Study on damage mechanism of SESAM in high power ultrafast laser," *2011 International Conference on Multimedia Technology*. pp. 6050–6053, 2011.

[147] R. I. Woodward *et al.*, "Few-layer MoS 2 saturable absorbers for short-pulse laser technology: current status and future perspectives [Invited]," *Opt. Express*, vol. 23, no. 15, 2015.

[148] R. I. Woodward *et al.*, "Wideband saturable absorption in few-layer molybdenum diselenide (MoSe 2) for Q-switching Yb-, Er-and Tm-doped fiber lasers," *Opt. Express*, vol. 23, no. 15, 2015.

[149] Y. I. Jhon *et al.*, "Metallic MXene Saturable Absorber for Femtosecond Mode-Locked Lasers," *Advanced Materials*, 2017.

[150] B. Anasori, M. R. Lukatskaya, and Y. Gogotsi, "2D metal carbides and nitrides (MXenes) for energy storage," *Nat. Rev. Mater.*, vol. 2, p. 16098, 2017.

[151] B. Anasori *et al.*, “Two-Dimensional, Ordered, Double Transition Metals Carbides (MXenes),” *ACS Nano*, vol. 9, no. 10, pp. 9507–9516, 2015.

[152] M. Naguib, V. N. Mochalin, M. W. Barsoum, and Y. Gogotsi, “25th anniversary article: MXenes: A new family of two-dimensional materials,” *Adv. Mater.*, vol. 26, no. 7, pp. 992–1005, 2014.

[153] J. Halim *et al.*, “Transparent Conductive Two-Dimensional Titanium Carbide Epitaxial Thin Films,” *Chem. Mater.*, vol. 26, no. 7, pp. 2374–2381, Apr. 2014.

[154] O. Mashtalir *et al.*, “Intercalation and delamination of layered carbides and carbonitrides,” *Nat. Commun.*, vol. 4, p. 1716, Apr. 2013.

[155] C. J. Zhang *et al.*, “Transparent, Flexible, and Conductive 2D Titanium Carbide (MXene) Films with High Volumetric Capacitance,” *Adv. Mater.*, p. 1702678, Jul. 2017.

[156] K. Hantanasirisakul *et al.*, “Fabrication of Ti3C2Tx MXene Transparent Thin Films with Tunable Optoelectronic Properties,” *Adv. Electron. Mater.*, vol. 2, no. 6, p. 1600050, Jun. 2016.

[157] M. Ghidiu, M. R. Lukatskaya, M.-Q. Zhao, Y. Gogotsi, and M. W. Barsoum, “Conductive two-dimensional titanium carbide ‘clay’ with high volumetric capacitance,” *Nature*, vol. 516, 2014.

[158] A. Ali, A. Belaidi, S. Ali, M. I. Helal, and K. A. Mahmoud, “Transparent and conductive Ti3C2Tx (MXene) thin film fabrication by electrohydrodynamic atomization technique,” *J. Mater. Sci. Mater. Electron.*, vol. 27, no. 5, pp. 5440–5445, May 2016.

[159] M. Alhabeb *et al.*, “Guidelines for Synthesis and Processing of Two-Dimensional Titanium Carbide ($Ti_3C_2T_x$ MXene),” *Chem. Mater.*, p. acs.chemmater.7b02847, Sep. 2017.

[160] E. Nossol and A. J. G. Zarbin, “A Simple and Innovative Route to Prepare a Novel Carbon Nanotube/Prussian Blue Electrode and its Utilization as a Highly Sensitive H_2O_2 Amperometric Sensor,” *Adv. Funct. Mater.*, vol. 19, no. 24, pp. 3980–3986, Dec. 2009.

[161] S. H. Domingues *et al.*, “Transparent and conductive thin films of graphene/polyaniline nanocomposites prepared through interfacial polymerization,” *Chem. Commun.*, vol. 47, no. 9, pp. 2592–2594, 2011.

[162] R. V. Salvatierra, M. M. Oliveira, and A. J. G. Zarbin, “One-Pot Synthesis and Processing of Transparent, Conducting, and Freestanding Carbon Nanotubes/Polyaniline Composite Films,” *Chem. Mater.*, vol. 22, no. 18, pp. 5222–5234, Sep. 2010.

[163] V. H. R. Souza *et al.*, “Flexible, Transparent and Thin Films of Carbon Nanomaterials as Electrodes for Electrochemical Applications,” *Electrochim. Acta*, vol. 197, pp. 200–209, Apr. 2016.

[164] A. Lipatov, M. Alhabeb, M. R. Lukatskaya, A. Boson, Y. Gogotsi, and A. Sinitskii, “Effect of Synthesis on Quality, Electronic Properties and Environmental Stability of Individual Monolayer Ti3C2 MXene Flakes,” *Adv. Electron. Mater.*, vol. 2, no. 12, p. 1600255, Dec. 2016.

[165] F. Shahzad *et al.*, “Electromagnetic interference shielding with 2D transition metal

carbides (MXenes).," *Science*, vol. 353, no. 6304, pp. 1137–40, Sep. 2016.

[166] Y. Dong, D. Saini, L. A. Echegoyen, and R. Podila, "Passive optical switches based on endohedral fullerenes," 2016.

[167] A. Sarycheva *et al.*, "Two-Dimensional Titanium Carbide (MXene) as Surface-Enhanced Raman Scattering Substrate," *J. Phys. Chem. C*, vol. 121, no. 36, pp. 19983–19988, 2017.

[168] A. D. Dillon *et al.*, "Highly Conductive Optical Quality Solution-Processed Films of 2D Titanium Carbide," *Adv. Funct. Mater.*, vol. 26, no. 23, pp. 4162–4168, Jun. 2016.

[169] V. Mauchamp *et al.*, "Enhanced and tunable surface plasmons in two-dimensional Ti3 C2 stacks: Electronic structure versus boundary effects," *Phys. Rev. B - Condens. Matter Mater. Phys.*, vol. 89, no. 23, 2014.

[170] L. De Boni, E. L. Wood, C. Toro, and F. E. Hernandez, "Optical saturable absorption in gold nanoparticles," *Plasmonics*, vol. 3, no. 4, pp. 171–176, 2008.

[171] A. L. Stepanov, "Nonlinear optical properties of implanted metal nanoparticles in various transparent matrixes: A review," *Reviews on Advanced Materials Science*, vol. 27, no. 2. pp. 115–145, 2011.

[172] N. Del Fatti and F. Vallée, "Ultrafast optical nonlinear properties of metal nanoparticles," *Appl. Phys. B Lasers Opt.*, vol. 73, no. 4, pp. 383–390, 2001.

[173] A. L. Stepanov, "Nonlinear optical properties of implanted metal nanoparticles in various transparent matrixes NONLINEAR OPTICAL PROPERTIES OF IMPLANTED METAL NANOPARTICLES IN VARIOUS TRANSPARENT

MATRIXES: A REVIEW," *Rev. Adv. Mater. Sci*, vol. 27, pp. 115–145, 2011.

[174] S.-J. Ding *et al.*, "Largely Enhanced Saturable Absorption of a Complex of Plasmonic and Molecular-Like Au Nanocrystals," *Sci. Rep.*, vol. 5, no. 1, p. 9735, Sep. 2015.

[175] H. Zhang *et al.*, "Z-scan measurement of the nonlinear refractive index of graphene," *Opt. Lett.*, vol. 37, no. 11, p. 1856, Jun. 2012.

[176] K. Lingam, R. Podila, H. Qian, S. Serkiz, and A. M. Rao, "Evidence for edge-state photoluminescence in graphene quantum dots," *Adv. Funct. Mater.*, vol. 23, no. 40, pp. 5062–5065, 2013.

[177] S. Yuan, R. Roldn, M. I. Katsnelson, and F. Guinea, "Effect of point defects on the optical and transport properties of MoS2 and WS2," *Phys. Rev. B - Condens. Matter Mater. Phys.*, vol. 90, no. 4, 2014.

[178] Y. Dong *et al.*, "Saturable Absorption in 2D Ti_3C_2 MXene Thin Films for Passive Photonic Diodes," *Adv. Mater.*, vol. 1705714, p. 1705714, 2018.

[179] R. R. Nair *et al.*, "Fine Structure Constant Defines Visual Transperency of Graphene," *Science (80-.).*, vol. 320, no. June, p. 2008, 2008.

[180] S. Z. Butler *et al.*, "Progress, challenges, and opportunities in two-dimensional materials beyond graphene," *ACS Nano*, vol. 7, no. 4. pp. 2898–2926, 2013.

[181] B. Xiao, Y. C. Li, X. F. Yu, and J. B. Cheng, "MXenes: Reusable materials for NH3 sensor or capturer by controlling the charge injection," *Sensors Actuators, B Chem.*, vol. 235, pp. 103–109, 2016.

[182] T. L. Tan, H. M. Jin, M. B. Sullivan, B. Anasori, and Y. Gogotsi, "High-

Throughput Survey of Ordering Configurations in MXene Alloys Across Compositions and Temperatures," *ACS Nano*, vol. 11, no. 5, pp. 4407–4418, May 2017.

[183] Y. Dong *et al.*, "Metallic MXenes: A new family of materials for flexible triboelectric nanogenerators," *Nano Energy*, Dec. 2017.

[184] C. Dai *et al.*, "Two-Dimensional Tantalum Carbide (MXenes) Composite Nanosheets for Multiple Imaging-Guided Photothermal Tumor Ablation," *ACS Nano*, vol. 11, no. 12, pp. 12696–12712, Dec. 2017.

[185] W. Feng *et al.*, "Ti $_3$ C $_2$ MXene: a promising microwave absorbing material," *RSC Adv.*, vol. 8, no. 5, pp. 2398–2403, Jan. 2018.

[186] Y. I. Jhon, M. Seo, and Y. M. Jhon, "First-principles study of a MXene terahertz detector," *Nanoscale*, vol. 10, no. 1, pp. 69–75, Dec. 2018.

[187] T. L. Cocker *et al.*, "Terahertz conductivity of the metal-insulator transition in a nanogranular VO2 film," *Appl. Phys. Lett.*, vol. 97, no. 22, p. 221905, Nov. 2010.

[188] J. B. Baxter and C. A. Schmuttenmaer, "Carrier dynamics in bulk ZnO. I. Intrinsic conductivity measured by terahertz time-domain spectroscopy," *Phys. Rev. B*, vol. 80, no. 23, p. 235205, Dec. 2009.

[189] P. U. Jepsen, D. G. Cooke, and M. Koch, "Terahertz spectroscopy and imaging - Modern techniques and applications," *Laser Photon. Rev.*, vol. 5, no. 1, pp. 124–166, Jan. 2011.

[190] R. Ulbricht, E. Hendry, J. Shan, T. F. Heinz, and M. Bonn, "Carrier dynamics in semiconductors studied with time-resolved terahertz spectroscopy," *Rev. Mod.*

Phys., vol. 83, no. 2, pp. 543–586, Jun. 2011.

[191] K. T. Butler, B. J. Dringoli, L. Zhou, P. M. Rao, A. Walsh, and L. V. Titova, "Ultrafast carrier dynamics in $BiVO_4$ thin film photoanode material: interplay between free carriers, trapped carriers and low-frequency lattice vibrations," *J. Mater. Chem. A*, vol. 4, no. 47, pp. 18516–18523, Nov. 2016.

[192] L. V Titova *et al.*, "Ultrafast carrier dynamics and the role of grain boundaries in polycrystalline silicon thin films grown by molecular beam epitaxy," *Semicond. Sci. Technol.*, vol. 31, no. 10, p. 105017, Oct. 2016.

[193] J. Lloyd-Hughes and T.-I. Jeon, "A Review of the Terahertz Conductivity of Bulk and Nano-Materials," *J. Infrared, Millimeter, Terahertz Waves*, vol. 33, no. 9, pp. 871–925, Sep. 2012.

[194] M. Naftaly and R. E. Miles, "Terahertz Time-Domain Spectroscopy for Material Characterization," *Proc. IEEE*, vol. 95, no. 8, pp. 1658–1665, Aug. 2007.

[195] T. L. Cocker *et al.*, "Microscopic origin of the Drude-Smith model," *Phys. Rev. B*, vol. 96, no. 20, p. 205439, Nov. 2017.

[196] S. A. Jensen *et al.*, "Ultrafast Photoconductivity of Graphene Nanoribbons and Carbon Nanotubes," *Nano Lett.*, vol. 13, no. 12, pp. 5925–5930, Dec. 2013.

[197] G. W. Guglietta *et al.*, "Lifetime, Mobility, and Diffusion of Photoexcited Carriers in Ligand-Exchanged Lead Selenide Nanocrystal Films Measured by Time-Resolved Terahertz Spectroscopy," *ACS Nano*, vol. 9, no. 2, pp. 1820–1828, Feb. 2015.

[198] C. Richter and C. A. Schmuttenmaer, "Exciton-like trap states limit electron

mobility in TiO2 nanotubes," *Nat. Nanotechnol.*, vol. 5, no. 11, pp. 769–772, Nov. 2010.

[199] B. G. Alberding *et al.*, "Static and Time-Resolved Terahertz Measurements of Photoconductivity in Solution-Deposited Ruthenium Dioxide Nanofilms.," *J. Phys. Chem. C. Nanomater. Interfaces*, vol. 121, no. 7, pp. 4037–4044, Feb. 2017.

[200] B. G. Alberding, G. P. Kushto, P. A. Lane, and E. J. Heilweil, "Reduced Photoconductivity Observed by Time-Resolved Terahertz Spectroscopy in Metal Nanofilms with and without Adhesion Layers.," *Appl. Phys. Lett.*, vol. 108, no. 22, May 2016.

[201] M. Walther, D. G. Cooke, C. Sherstan, M. Hajar, M. R. Freeman, and F. A. Hegmann, "Terahertz conductivity of thin gold films at the metal-insulator percolation transition," *Phys. Rev. B*, vol. 76, no. 12, p. 125408, Sep. 2007.

[202] T. Hu *et al.*, "Anisotropic electronic conduction in stacked two-dimensional titanium carbide," *Sci. Rep.*, vol. 5, no. 1, p. 16329, Dec. 2015.

[203] A. Miranda, J. Halim, M. W. Barsoum, and A. Lorke, "Electronic properties of freestanding $Ti_3C_2T_x$ MXene monolayers," *Appl. Phys. Lett.*, vol. 108, no. 3, p. 33102, Jan. 2016.

[204] K. J. Tielrooij *et al.*, "Hot-carrier photocurrent effects at graphene–metal interfaces," *J. Phys. Condens. Matter*, vol. 27, no. 16, p. 164207, Apr. 2015.

[205] G. Jnawali, Y. Rao, H. Yan, and T. F. Heinz, "Observation of a Transient Decrease in Terahertz Conductivity of Single-Layer Graphene Induced by Ultrafast Optical Excitation," *Nano Lett.*, vol. 13, no. 2, pp. 524–530, Feb. 2013.

[206] A. J. Frenzel *et al.*, “Observation of suppressed terahertz absorption in photoexcited graphene,” *Appl. Phys. Lett.*, vol. 102, no. 11, p. 113111, Mar. 2013.

[207] C. J. Docherty *et al.*, “Extreme sensitivity of graphene photoconductivity to environmental gases,” *Nat. Commun.*, vol. 3, no. 1, p. 1228, Jan. 2012.

[208] A. Tomadin *et al.*, “The ultrafast dynamics and conductivity of photoexcited graphene at different Fermi energies,” Dec. 2017.